

DISSERTATION

EXCITED ELECTRONIC STATE DECOMPOSITION MECHANISMS AND
DYNAMICS OF NITRAMINE ENERGETIC MATERIALS AND MODEL SYSTEMS

Submitted by

Margo Greenfield

Physics Department

In partial fulfillment of the requirements

For the Degree of Doctor of Philosophy

Colorado State University

Fort Collins, Colorado

Spring 2007

UMI Number: 3266373

INFORMATION TO USERS

The quality of this reproduction is dependent upon the quality of the copy submitted. Broken or indistinct print, colored or poor quality illustrations and photographs, print bleed-through, substandard margins, and improper alignment can adversely affect reproduction.

In the unlikely event that the author did not send a complete manuscript and there are missing pages, these will be noted. Also, if unauthorized copyright material had to be removed, a note will indicate the deletion.

UMI[®]

UMI Microform 3266373

Copyright 2007 by ProQuest Information and Learning Company.

All rights reserved. This microform edition is protected against unauthorized copying under Title 17, United States Code.

ProQuest Information and Learning Company
300 North Zeeb Road
P.O. Box 1346
Ann Arbor, MI 48106-1346

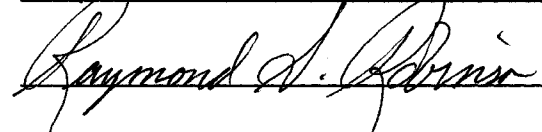
COLORADO STATE UNIVERSITY

January 5, 2007

WE HEREBY RECOMMEND THAT THE DISSERTATION PREPARED
UNDER OUR SUPERVISION BY MARGO GREENFIELD ENTITLED EXCITED
ELECTRONIC STATE DECOMPOSITION MECHANISMS AND DYNAMICS OF
NITRAMINE ENERGETIC MATERIALS AND MODEL SYSTEMS BE ACCEPTED
AS FULFILLING IN PART REQUIREMENTS FOR THE DEGREE OF DOCTOR OF
PHILOSOPHY

Committee on Graduate Work





Chicor-gan Me
Advisor



Co-Adviser

Department Head/Director

ABSTRACT OF DISSERTATION

EXCITED ELECTRONIC STATE DECOMPOSITION MECHANISMS AND DYNAMICS OF NITRAMINE ENERGETIC MATERIALS AND MODEL SYSTEMS

Energetic materials play an important role in aeronautics, the weapon industry, and the propellant industry due to their broad applications as explosives and fuels. RDX (1,3,5-trinitrohexahydro-s-triazine), HMX (octahydro-1,3,5,7-tetranitro-1,3,5,7-tetrazocine), and CL-20 (2,4,6,8,10,12-hexanitro-2,4,6,8,10,12-hexaazaisowurtzitane) are compounds which contain high energy density (J/cm^3) or (J/g). Although RDX and HMX have been studied extensively over the past several decades, a complete understanding of their decomposition mechanisms and dynamics is unknown. This work describes the novel approach taken to assist in the overall understanding of the decomposition of these energetic materials, namely their gas phase single molecule excited state decomposition.

Excited electronic states can be generated by shock and compression and therefore play an important role in the initiation/ decomposition of RDX, HMX, and CL-20. Energy (ns lasers) and time resolved (fs lasers) UV-photodissociation experiments have been performed to elucidate the mechanisms and dynamics of gas phase energetic material decomposition from excited electronic states. Time of flight mass spectroscopy (TOFMS), laser induced fluorescence (LIF), and pump-probe experiments performed on

three energetic materials, as well as five model systems, illustrate the unique behavior of energetic materials.

TOFMS UV photodissociation (ns) experiments of gas phase RDX, HMX, and CL-20 generate the NO molecule as the initial decomposition product. Four different vibronic transitions of the initial decomposition product, the NO molecule, are observed: $A^2\Sigma(v'=0)\leftarrow X^2\Pi(v''=0,1,2,3)$. Simulations of the rovibronic intensities for the $A\leftarrow X$ transitions demonstrate that NO dissociated from RDX, HMX, and CL-20 is rotationally cold (~ 20 K) and vibrationally hot (~ 1800 K). Conversely, experiments on the five model systems (nitromethane, dimethylnitramine, nitropyrrolidine, nitropiperidine and dinitropiperazine) produce rotationally hot and vibrationally cold NO spectra.

LIF experiments are performed to rule out the possible decomposition product OH, generated along with NO, perhaps from the suggested HONO elimination mechanism. The OH radical is not observed in the fluorescence experiments, indicating the HONO decomposition intermediate is not an important pathway for the excited electronic state decomposition of cyclic nitramines.

The NO molecule is also employed to measure the dynamics of the excited state decomposition. A 226 nm, 180 fs light pulse is utilized to photodissociate the gas phase systems. Stable ion states of DMNA and nitropyrrolidine are observed while the energetic materials and remaining model systems present the NO molecule as the only observed product. Pump-probe transients of the resonant $A\leftarrow X$ (0-0) transition of the NO molecule show a constant signal indicating these materials decompose faster than the time duration of the 226 nm laser light. Comparison of NO from the three energetic materials to NO from NO_2 gas generated by a 180 fs light pulse at 226 nm indicates that

NO_2 is not an intermediate product of the excited electronic state photodissociation of RDX, HMX, or CL-20.

Two possible excited state decomposition mechanisms are suggested for the three energetic materials. The first mechanism involves a dissociative excited electronic state in which the nitramine moieties (CNNO_2) in the electronically excited energetic material isomerize (CNONO) and further dissociate. In the second possible decomposition mechanism the electronically excited molecules undergo internal conversion to very highly excited (~ 5 eV of vibrational energy) vibrational states of their ground electronic state. Once in the ground state, isomerization of the nitramine moieties occurs and the material further decomposes. Computational results together with the experimental results indicate the energetic materials decompose according to the second mechanism, relaxation to the ground state, while the model systems follow the excited electronic state decomposition pathway. An additional path in which the $-\text{NO}_2$ moiety loses an O atom, becomes linear with the CN attachment, and then NO is released, is also consistent with experimental observations but is, as yet, not supported by calculations.

The keys to generating better cyclic nitramine energetic materials would then be to enhance the propensity to form $S_1 - S_0$ conical intersections, improve $S_1 - S_0$ Franck-Condon factors for internal conversion near the S_1 zero point level, and to enhance the S_0 density of vibronic states at high S_0 vibrational energy. Additionally, one would like to generate NO with less internal vibrational excitation, so altering the NONO vibrational excitation in the dissociation process could be important. These ideas would suggest that more flexible cyclic nitramines, with increased internal degrees of freedom, might be

useful to explore for new energetic systems. Perhaps larger ring structures along the lines of CL-20 might be useful compounds to explore.

Margo Greenfield
Physics Department
Colorado State University
Fort Collins, CO 80523
Spring 2007

Acknowledgments

There are a number of people whom I must thank for their contributions towards this thesis. Their assistance and guidance made my graduate experience priceless. First and foremost, I would like to thank my advisor Professor Elliot R. Bernstein. His knowledge, insights, patience, understanding and all around support has been invaluable. I especially appreciate the fact that he always made time to listen and help me with all aspects of school.

I must gratefully acknowledge Dr. Yuanqing Guo for all of his excellent help in the lab as well as his very valuable discussions about our experiments. His extreme patience and dedication made these experiments successful. Without his help my graduate experience would not have been nearly as fruitful or enjoyable. I would also like to thank Atanu Bhattacharya. As a new graduate student to our group he has made some helpful calculational contributions.

Dr. Laura Smilowitz and Dr. Bryan Henson have been invaluable collaborators and friends. I would like to thank them for their interesting discussions and helpful insights.

Finally, I would like to thank my parents, Anita and Gary, for their love and support during this long adventure and my sister Katie for being there when I needed someone to listen.

Contents

CHAPTER 1 : INTRODUCTION

Overview.....	1
Introduction.....	2
Background.....	13
Summary.....	21
References.....	25

CHAPTER 2 : DECOMPOSITION OF NITRAMINE ENERGETIC MATERIALS IN EXCITED ELECTRONIC STATES : HMX AND RDX

Introduction.....	27
Experimental procedures	31
Results and discussion.....	33
Conclusions.....	40
References.....	41

CHAPTER 3 : ULTRAFAST PHOTODISSOCIATION DYNAMICS OF HMX AND RDX FROM THE EXCITED ELECTRONIC STATES VIA FEMTOSECOND LASER PUMP-PROBE TECHNIQUES

Introduction.....	44
Experimental procedures.....	46

Calculational procedures.....	48
Results and discussion.....	49
Conclusions.....	54
References.....	55

**CHAPTER 4 : COMPARISON OF ELECTRONICALLY EXCITED
PHOTODISSOCIATION BETWEEN NITRAMINE ENERGETIC MATERIALS
AND MODEL SYSTEMS**

Introduction.....	57
Experimental procedures.....	60
Calculational procedures.....	63
Results.....	64
Discussion.....	72
Conclusions.....	80
References.....	82

CHAPTER 5 : FUTURE WORK..... 84

APPENDIX 1 : EXPERIMENTAL TECHNIQUES

Introduction.....	88
Gas phase molecules.....	88
Supersonic expansion.....	89
Spectroscopy measurements.....	93

Time of flight mass spectroscopy.....	93
REMPI.....	95
LIF.....	97
Time resolved spectroscopy.....	101
References.....	109

APPENDIX 2 : FEMTOSECOND LASER

Overview.....	110
Alignment	
Oscillator.....	122
Stretcher.....	131
Pockels cell.....	136
Amplifier.....	141
Compressor.....	144
TOPAS.....	146
Pictures.....	185
References.....	192

APPENDIX 3 : SAMPLE PREPRATION

Introduction.....	193
Preparation.....	194
References.....	198

APPENDIX 4 : RRKM THEORY	199
References.....	207
APPENDIX 5 : SOURCES OF MATERIAL	208

Chapter 1: Introduction

Overview

This dissertation consists mainly of three publications which have been directly included within this thesis. In efforts to tie this dissertation together an introductory chapter including three main sections (introduction, background, and summary) has been established. The introduction section of the first chapter describes, in detail, the energetic materials and models systems investigated, specifically addressing prior work on their ground state geometries and decomposition mechanisms. The principles behind this study are discussed within the background section. They allow for an overview of the goal of this work and how it has been accomplished. Finally, the summary brings together the three main chapters of this thesis by highlighting their most important results.

The work in this thesis focuses on energy (ns) and time (fs) resolved photodissociation experiments. They are performed to elucidate the mechanisms and dynamics of gas phase energetic material decomposition from excited electronic states. The energetic materials HMX, RDX and CL-20 are placed into the gas phase as intact molecules via laser desorption and supersonic expansion. UV photodissociation ionization time of flight mass spectroscopy (TOFMS) and laser induced fluorescence (LIF) experiments are performed to help determine possible decomposition mechanisms. Femtosecond pump-probe techniques are used to measure the ultrafast photodissociation

dynamics of RDX, HMX, and CL-20 via their initial decomposition product, the NO molecule. Onset of this initial product gives insight into the overall dynamics of these systems. Similar experiments are done on “model systems” in efforts to better understand the mechanistic characteristics of the larger more complicated energetic materials.

Finally, specific information on the experimental techniques, femtosecond laser and sample preparation are recorded in extreme detail within the appendices. This record is meant for future Bernstein group members.

Introduction

Energetic materials are characterized most simply by the magnitude of their adiabatic exotherm and the rate at which it occurs. Understanding their mechanisms and dynamics will allow for better control and improvement of the performance of these materials for combustion and explosion. The energetic materials and model systems studied in this work are based on the nitro group and contain oxidant fuel within their structure. The three specific energetic materials of interest are the cyclic nitramines RDX (1,3,5-trinitrohexahydro-s-triazine), HMX (octahydro-1,3,5,7-tetranitro-1,3,5,7-tetrazocine), and CL-20 (2,4,6,8,10,12-hexanitro-2,4,6,8,10,12-hexaazaisowurtzitane)^{1,2}. RDX was discovered in the 1890's but used as an elixir until its explosive properties were revealed in the 1920's. HMX was produced 10 years later. Dubbed as the “Royal Demolition Explosive” and “Her Majesty's Explosive” these two materials surpassed their predecessor TNT (2,4,6-trinitrotoluene) in both power and material stability. In actuality their acronyms stand for “Research Department composition X” and “High-Molecular-weight rdX”. CL-20 first synthesized around 1987³, is the most recent successor of the well known RDX and HMX. Due to CL-20's cage structure it has a high

density and therefore high energy output. CL-20 is expected to eventually replace RDX and HMX in many applications, but due to its young age not much experimental or theoretical information is known about it⁴. The structures of these energetic materials can be found in Figure 1 below.

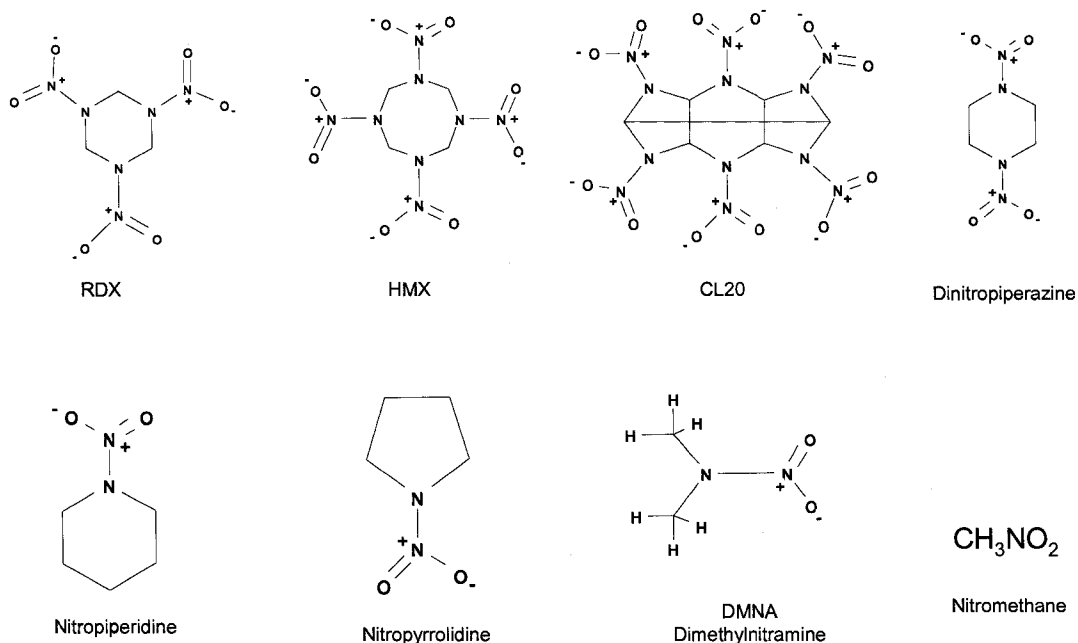


Figure 1. Energetic Materials (RDX, HMX, and CL-20) and the Model Systems (Dinitropiperazine, Nitropiperidine, Nitropyrrolidine, Dimethylnitramine (DMNA) and Nitromethane)

Energetic materials are used as propellants, fuels and in military explosives. RDX and HMX are employed in a number of different types of warfare because they are exceptionally stable at room temperature and their impact sensitivity is quite low. Defining the processes that control the decomposition of these materials will allow for assessing the safety and aging characteristics of existing warfare and propellants. Understanding the shelf life of existing munitions as well as developing new, less sensitive materials will only occur as a more fundamental understanding of the underlying reactions in these materials evolves.

Although HMX and RDX have been in existence for about 100 years, complete understanding of their properties, including their decomposition mechanisms and kinetics, is still unknown. It was not until the 1980's that a general insight among the explosives community evolved. Namely, understanding the detailed decomposition chemistry of these materials was imperative for the design of dependable systems and analyzing structures/materials that have behaved abnormally would be imperative for comprehensive knowledge of the material. As questions were raised about the underlying phenomena behind these materials it became clear that the ignition and combustion of these materials were extremely complicated due to their numerous phases, time dependence, and multiple branching decomposition pathways⁵. A wide variety of theoretical calculations as well as experiments have been performed on HMX and RDX in efforts to elucidate their properties. The underlying, and possibly the most important, question revolving around these materials is the prediction of combustion and detonation properties from the molecular and material properties specific to the energetic material in question. In efforts to understand these properties two categories of experiments have been performed: condensed and gas phase experiments.

In the condensed phase, an enormous effort has gone into understanding slow to fast and low to medium to high thermal decomposition of solid phase energetic materials. Slow cook-off events, heating to relatively low temperatures over long time scales (hours), have shown that numerous products may occur due to the many competing reaction channels^{6,7}. The products can give rise to additional reactions that are not expected to occur from the original material. Heating material for 20-1000 μ s to temperatures around 1000 °C can occur from mechanical impact. The numbers of

reactions accessed during the mechanical impact are still large but may differ from those accesses during a slow cook-off. These differing reactions are accessed due to the opening of higher activation channels^{8,9}. Very fast ($< 1 \mu\text{s}$) times and high temperatures are obtained by use of shock waves. Pressures reached during the shock waves are greater than 100 kbar and because of this it is hard to determine the type of detailed chemistry that could be occurring. Modification of condensed phase chemical kinetics and reaction notions should occur to account for the highly possible electronic excitation and plasma states accessible from shock waves¹⁰.

A number of different gas phase experiments have been performed in efforts to better understand the overall decomposition mechanisms of these energetic materials. The first of these is flame experiments. These experiments probe the combustion products that occur during the burning of RDX and HMX. Gas phase combustion studies revolve around flame structure experiments and are actually an intermediate between condensed phase and gas phase research. Flame investigations offer information on the temperature of the flames, the identity of the species within the flame and their concentrations, as well as species spatial distributions¹¹⁻¹⁹. Inspection of these types of data yield information on the composition of the condensed phase reaction products that are occurring on the burning surface thereby eluding to the reactions and mechanisms occurring in the condensed phase¹⁶. Additionally, depending upon where these measurements are made, with respect to the flame propagation, information about further transformations of products emerging from the surface can be obtained.

Thermal decomposition studies can also probe gas phase decomposition intermediates and products. Richard Behrens has used a quite complicated

thermogravimetric analytic device with a modulated mass spectrometer detection and time of flight velocity analysis to identify molecular species from heated samples of energetic materials and to correlate their production with the weight loss of the sample. From this information an overall scheme of decomposition was determined for RDX. One should note several interesting large intermediates observed in this experiment: NH_2CHO , CH_2NHCHO , oxy-s-triazine (OST) and 1-nitroso-3,5-dinitrohexahydro-5, triazine (ONDTA)²⁰. A possible decomposition mechanism to form the ONTDA from RDX is a loss of an oxygen atom from one of the nitro groups. ONTDA is an important intermediate that could possibly be correlated to the excited state decomposition work discussed in this thesis.

An older yet highly interesting experiment by Lee²¹ and coworkers is a molecular beam experiment on RDX. In this ground state, gas phase experiment, RDX was placed into the vapor phase via thermal excitation, and the gas phase molecules were vibrationally excited under collision free conditions via multiphoton absorption of a CO_2 laser. Fragments were further detected by a mass spectrometer. Two important experimental conclusions and hypothesized decomposition mechanisms were found. First, a majority of the ground state dissociation proceeded by a simultaneous fission to yield 3 CH_2NNO_2 molecules which then further fragmented. Second, the NO_2 product occurred through the secondary dissociation channel via the N-N bond fission. The final highly accepted possible decomposition mechanism is through the precursor HONO. This mechanism involves a transition state where hydrogen bonding forms a five membered ring CNNOH (see figure 2). The modified molecule further decomposes into the possible decomposition precursor HONO^{22} .

One can summarize the aforementioned ground state work to obtain 5 possible decomposition mechanisms. They are represented for RDX in Figure 2 below:

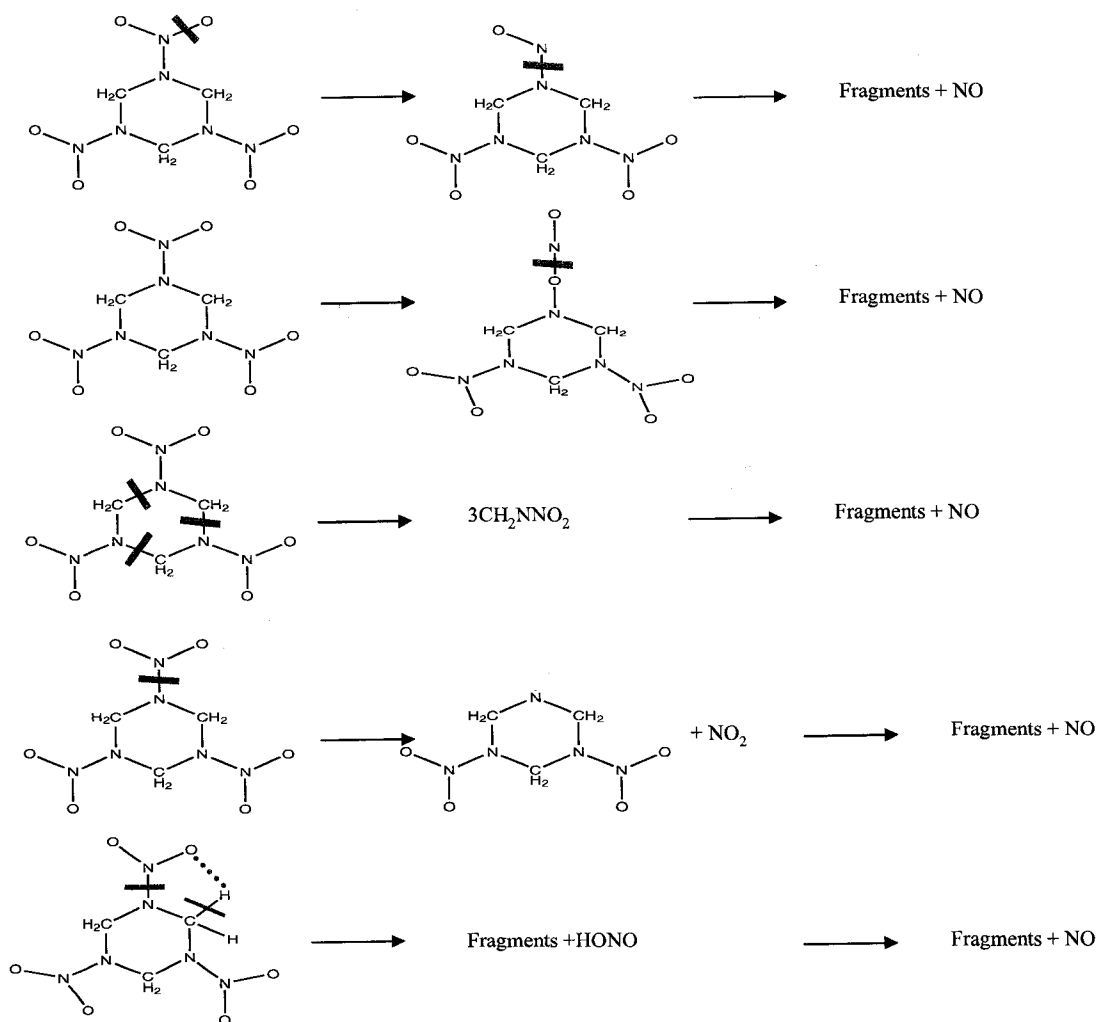


Figure 2. Possible Decomposition Mechanisms for RDX

These mechanisms were used as a starting point for our excited state decomposition work. Confirming the presence of the decomposition precursors would indicate which possible decomposition mechanism could occur.

To this point all of the information shown has been on the ground electronic state surface of energetic materials, but as alluded to briefly it is quite possible that

decomposition of these materials could occur through an excited state process. Compression and shock waves under very short time durations can initiate explosions even detonations. Excited electronic states can be created in molecular crystals. A 10^8 V/cm electric field exists between crystal planes; this is more than enough energy to excite and remove electrons from molecules within the crystals especially at defect and inclusion sites. An example of this comes from placing certain organic molecular crystals into a mortar and grinding them with a pestle. Light is observed due to the possible emission from $O^{\pm,0}$, $N^{\pm,0}$, $N_2^{\pm,0}$, $O_2^{\pm,0}$, C_2 , radicals and even the molecules comprising the crystals^{23,24}. This light is defined as triboluminescence.

Excited electronic states can be generated by shock and compression via excitonic and highest occupied molecular orbital (HOMO)/ lowest unoccupied molecular orbital (LUMO) gap molecular mechanisms. Williams²⁵⁻³¹, Dremin³², and Sharma³³⁻³⁵ have shown the importance of electronic excitation for the initial steps in the condensed phase detonation process. In these studies, shock and impact sensitivity on electronic excitation is compared with the shake-up promotion energy observed for x-ray photoelectron spectra. Core ionization excitations arise for an atom within a solid over the dimensions of a molecule (~ 100 fs). The Coulomb attraction of the ionized core for the valence electrons is on the order of the perturbation caused by high pressure (ca. 1 Mb) or shock. Therefore, a correlation between electronic excitation and shock-induced behavior could be postulated. The suggested mechanism is an electron transfer from the HOMO to the LUMO of an energetic molecule due to reduction of the HOMO/LUMO gap upon shock compression and the materials most likely to detonate are those that experience electronic excitation in response to compression and shock. So studying the decomposition of

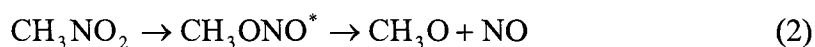
energetic materials from excited electronic states of isolated gas phase molecules is both relevant and important for practical, application, fundamental understanding, long term improvement, evolution and development²³.

As previously mentioned the overall scope of this work is to determine the excited state decomposition of the energetic materials RDX, HMX and the recently synthesized CL-20. As will be described in further detail later in this thesis the NO molecule has been observed as the initial decomposition product for the three of these energetic materials. In efforts to determine the decomposition mechanism for RDX and HMX we started with the five hypothesized mechanisms, suggested for RDX and HMX, and through experiment either ruled out or accepted the possibility of these mechanisms taking place.

To obtain a better understanding of the decomposition of these energetic materials, exploration into a number of 'model' systems has been proposed. Take for example a somewhat simple molecule nitromethane (CH_3NO_2). This molecule correlates well with RDX, HMX, and CL-20 due to its nitro composition. Although nitromethane is much simpler than the energetic materials in question, its decomposition mechanism has been proposed, by Zhang and Bauer³⁶, to have up to 99 different reactions. Needless to say if the decomposition mechanism of a rather simple molecule associates with or represents the more complex energetic nitramines there could be a lot of decomposition pathways involved. In short, these systems are complicated and if we can understand a simpler system that properly represents a larger system this might give insight into how the larger system behaves.

Therefore, the study of the excited state decomposition of the energetic material HMX, RDX, and CL-20 also includes a study on 5 model systems. These systems are nitromethane, dinitromethane, nitropyrrolidine, nitropiperidine, and dinitropiperazine. The structures of these compounds can be found in figure 1 above. On inspection of these “model” systems, one sees that nitropiperidine and dinitropiperazine are quite similar to RDX. While the smaller model systems nitromethane and dinitromethane don’t characterize the energetic materials as well, their simplicity is quite alluring and therefore they have been studied in the gas phase quite extensively. The following couple of paragraphs will present each of these model systems and outline their possible decomposition mechanism. This information will help in the overall understanding of the three energetic materials of interest.

Due to the simplicity of nitromethane (CH_3NO_2) there have been many experimental and theoretical studies performed on it. The infrared multiphoton dissociation (IRMPD) work of Wodtke et al, in Y.T. Lee’s lab, in the mid-80’s suggests two primary decomposition pathways^{37,38}. The first of which was N-N bond fission thereby producing CH_3 and NO_2 and the second involved an excited state isomerization yielding CH_3O and NO ,



The published branching ratio of eq. 2 to eq. 1 is 0.6 ± 0.2 . Theoretical calculations have shown three main decomposition pathways for nitromethane. Using a potential energy surface with a barrier to isomerization at 47.6 kcal/mol Rice and Thompson calculated the following pathways³⁹:



Depending upon the value of the isomerization barrier Rice and Thompson's calculations can be in very good agreement with Wodtke's experiment suggesting eqs. 3-5 represent the decomposition mechanisms of nitromethane.

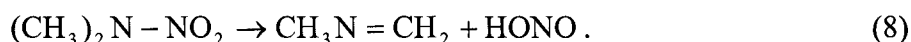
Dimethylnitramine, $(\text{CH}_3)_2\text{N}-\text{NO}_2$, is also often used as a prototype for the larger more important nitramines because it undergoes the same sorts of reactions postulated for RDX, HMX, and quite possibly CL-20. The three most widely accepted decomposition mechanisms of dimethylnitramine (DMNA), listed below, are due to bond fission^{40,41}



nitro-nitrate rearrangement followed by O-N bond fission^{42,43}



and a HONO elimination via a 5-center transition state⁴⁴



These three mechanisms are very similar to the decomposition mechanisms suggested for HMX and RDX.

Finally, we present the decomposition mechanisms for nitropyrrolidine, nitropiperidine, and dinitropiperazine. The complexity of each of these systems is much greater than nitromethane and dimethylnitramine and due to this, less information on their decomposition mechanisms is found. The works of Oxley and Naud have been quite helpful. Oxley suggests that each of these systems decomposes through a

nitrosamine via a loss of oxygen.⁴⁵ Naud on the other hand indicates that nitropiperidine and nitropyrrolidine follow a N-NO₂ bond homolysis pathway while 1,3-dinitropiperazine remains stable.⁴⁶ In both experiments the materials were in solution and the experiments were performed over the temperature range of 150-300 °C. Naud's work investigated these materials under varying pressures as well as temperature. The thermolysis products were analyzed by a gas chromatograph. The species were diluted in solvents to retard intermolecular reactions and stabilize intermediates by quenching highly reactive species allowing for better examination of their decomposition species and rates.

Comparisons of the different decomposition mechanisms for the "model" systems to those of the energetic materials allows one to see that the overall mechanisms have many similarities. Better understanding of the simpler systems will yield insight into the overall understanding of the more complex energetic systems. In general the dissociation process for the RNO₂ molecules (RDX, HMX, CL-20, and model systems) is quite complex and dependent upon competing pathways, activation energies, transition states, and especially dependent upon the electronic state potential energy surface which could include surface crossings upon which the dissociation occurs. To understand completely the condensed phase behavior of energetic materials a study to elucidate the molecular processes that occur as a function of electronic state must be accomplished because, as earlier stated, solid state behavior can generate different electronic states in the initiation process.

Background

The purpose of this background section first is to introduce how the gas phase single molecule experiments were performed (specifically how the highly volatile and unstable species were placed into the vapor phase). The principles behind the study will then be addressed. Specifically, the NO resonant absorption scheme will be discussed and the overall UV absorption spectra of the energetic materials will be presented. Finally, a short introduction into the three different measurement techniques will be provided.

The excited state decomposition studies on RDX, HMX, CL-20, and the five model systems were done in a collision free gas phase environment. The energetic materials are highly reactive and volatile solids which easily decompose upon heating. A number of novel techniques are employed to carry out these experiments. The first technique is generating the gas phase samples. A matrix assisted laser desorption (MALD) method is used to place the energetic materials into the vapor phase. This is an innovative use of a technique well known, in biological and inorganic studies, to place large, fragile, neutral molecules into the gas phase for spectroscopic investigation^{47,48}. The MALD techniques used in these experiments requires a specialized sample drum. The sample drum, an electrochemically coated Al₂O₃ cylindrical drum, is evenly sprayed with a matrix solution. The matrix solution consists of the materials of interest (RDX, HMX, or CL-20), dissolved in acetone, and Rhodamine 590 (R590), a laser dye, dissolved in methanol (10⁻² mol/l). The aerosol solution dries upon contact with the Al₂O₃ drum forming a thin film. This sample drum is further positioned within a laser desorption pulsed nozzle. The pulsed nozzle is timed to intercept the vapor arising from the laser desorbed spot on the drum. A 532 nm laser pulse (2 mJ/pulse) vaporizes the

R590 laser dye in the matrix film but is not absorbed by the energetic material (RDX, HMX, and CL-20 absorb below 250 nm, see Figure 3 for the absorption spectra of RDX and HMX). Consequently, single molecules of the energetic material are placed into the vapor phase without decomposition. The species is then carried from the pulsed nozzle through a supersonic expansion by means of a helium carrier gas (Figure 4). The expansion cools the molecules ($T_{\text{translation}} \sim 1\text{K}$, $T_{\text{rotation}} \sim 20\text{K}$, and $T_{\text{vibration}} \sim 50\text{K}$) and directs them into the spectroscopy region. Three different types of spectroscopy have been employed: time of flight mass spectroscopy (TOFMS), laser induced fluorescence spectroscopy (LIF), and a time resolved pump-probe TOFMS spectroscopy.

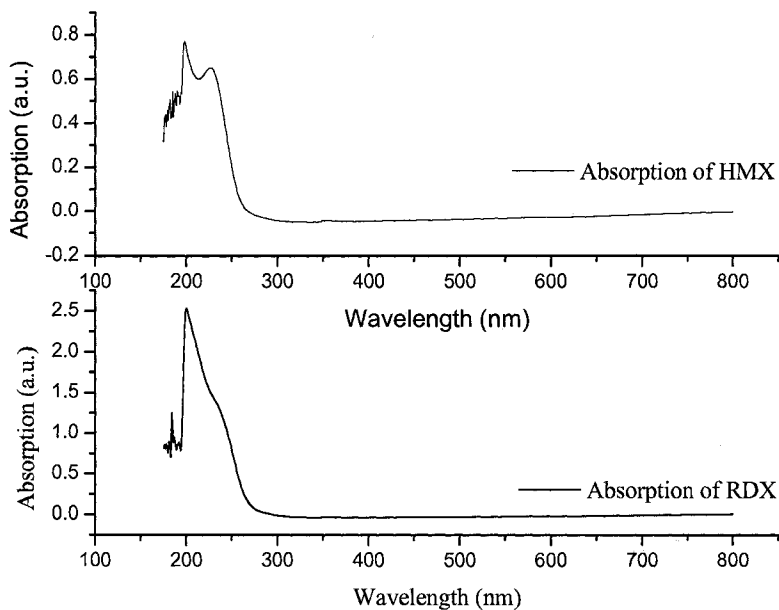


Figure 3. Absorption spectra of HMX and RDX. Note: absorption drops off drastically after ~250nm.

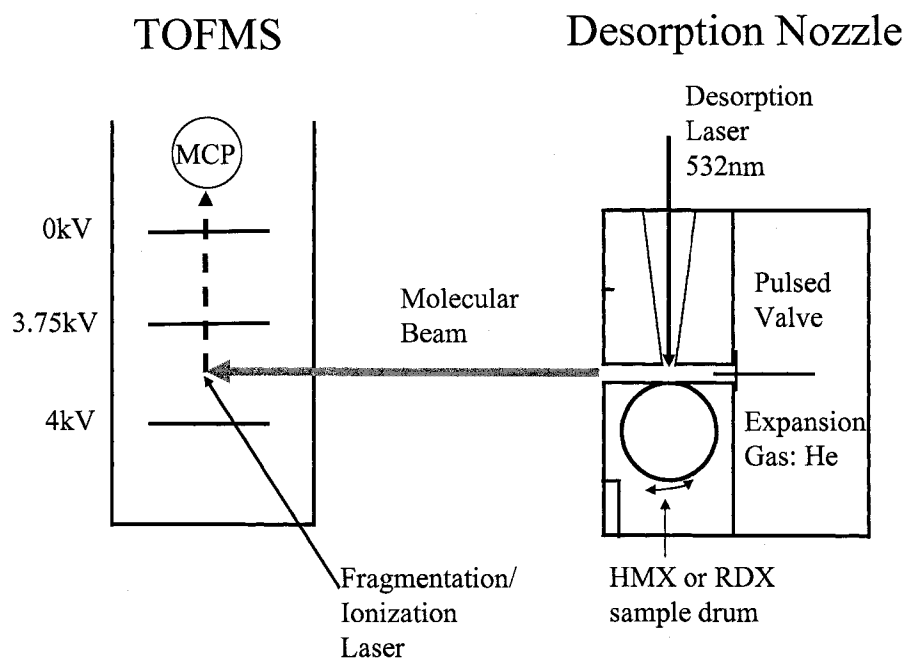


Figure 4. Experimental Setup

The experiments performed are unique given that the initial decomposition product observed, from RDX, HMX, and CL-20 resonantly absorbs in the same region as the energetic materials themselves absorb. Figure 5 shows the different $A^2\Sigma(v'=0) \leftarrow X^2\Pi(v''=0,1,2,3)$ resonant transitions for the NO molecule. The energy transition states were calculated using the following anharmonic oscillator equations:

$$v = T_e + [(G(v') - G(v''))] \quad (9)$$

$$G(v) = \left(v + \frac{1}{2}\right)\omega_e - \left(v + \frac{1}{2}\right)^2\omega_e x_e + \dots \quad (10)$$

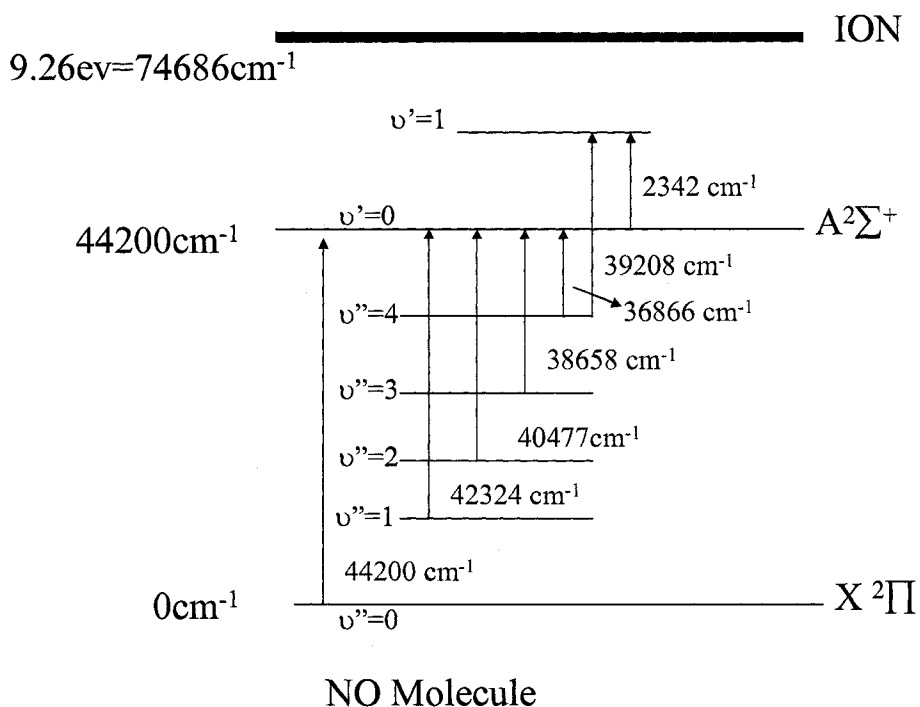


Figure 5. NO molecule vibrational levels for the ground and first excited state

where T_e is the electronic energy of the first excited state, $G(v')$ and $G(v'')$ are the vibrational terms for the ground and excited vibrational states respectively, and v is the vibrational quantum number. The values for the frequencies (ω_e) and anharmonic corrections ($\omega_e x_e$) for each vibrational level were obtained from Hertzburg's book. The supersonically cooled, gas phase molecule of HMX, RDX, or CL-20 absorbs a UV photon (226 nm, 236 nm, or 247 nm), see UV absorption spectra above, electronically exciting it into its excited state. The energetic molecule falls apart into fragments according to its corresponding decomposition mechanisms; the NO molecule is one of the initial decomposition products. Three different spectroscopy techniques have been employed to obtain information about the initial NO product.

Using a wavelength scanning ($\Delta E \sim 0.2 \text{ cm}^{-1}$) ns laser to excite the RDX, HMX, or CL-20 molecules, mass resolved excitation spectra can be obtained with the use of a

TOFMS. For the $A^2\Sigma(v'=0)\leftarrow X^2\Pi(v''=0)$ transition of the NO molecule a 226 nm photon excites the energetic material accessing its excited state. Once in its excited state two possible decomposition mechanisms are suggested: a dissociative excited state yielding decomposition fragments and the NO molecule; or relaxation from the excited state to the ground state followed by dissociation. In both mechanisms the dissociation is believed to occur through isomerization of the nitramine moiety followed by decomposition to the NO molecule. The initial NO product is further excited and ionized through a 1+1 resonant photon absorption. As the wavelength of light is scanned around 226 nm a mass resolved excitation spectra is recorded. The spectrum corresponds to the populated rotational and vibrational levels of the NO molecule. The rovibrational spectra can be obtained for the $A^2\Sigma(v'=0)\leftarrow X^2\Pi(v''=0,1,2,3)$ transition of the NO molecule originating from the three energetic materials. A schematic of this experiment, specifically for HMX, is represented in Figure 6.

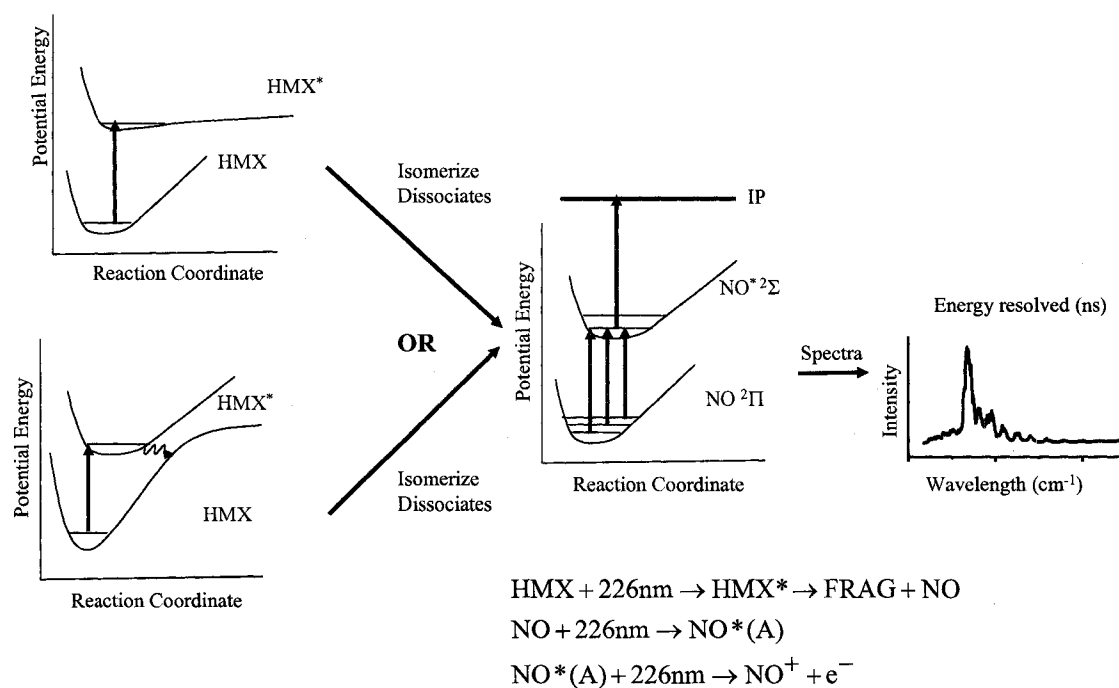


Figure 6. Schematic of excited state decomposition schemes. The figure on the top left represents the possible dissociative excited state decomposition followed by isomerization and dissociation and the lower left figure represents the decomposition mechanism in which the excited state relaxes back to the ground state followed by isomerization and dissociation.

Laser induced fluorescence spectroscopy has also been employed in efforts to better understand the excited state decomposition of HMX and RDX. The general experimental procedure is similar to the TOFMS experiments apart from the fact that laser emission is measured not ionized species. The motivation behind this set of experiments was to exclude the possible decomposition mechanism of a 5-membered ring transition state. This transition state could lead to a possible HONO precursor to the observed NO molecule. Emission from the OH molecule would suggest this is a viable decomposition mechanism. In this two color experiment 226 nm light is used to excite the gas phase energetic material and 308 nm light is used to probe the OH molecule. The energetic material is placed into the vapor phase using the same MALD technique.

Figure 7 contains the experimental schematic for the LIF experiment. OH emission was not observed in this experiment, but the LIF experiment allowed for a second check on the MRES NO spectra obtained via the TOFMS experiment.

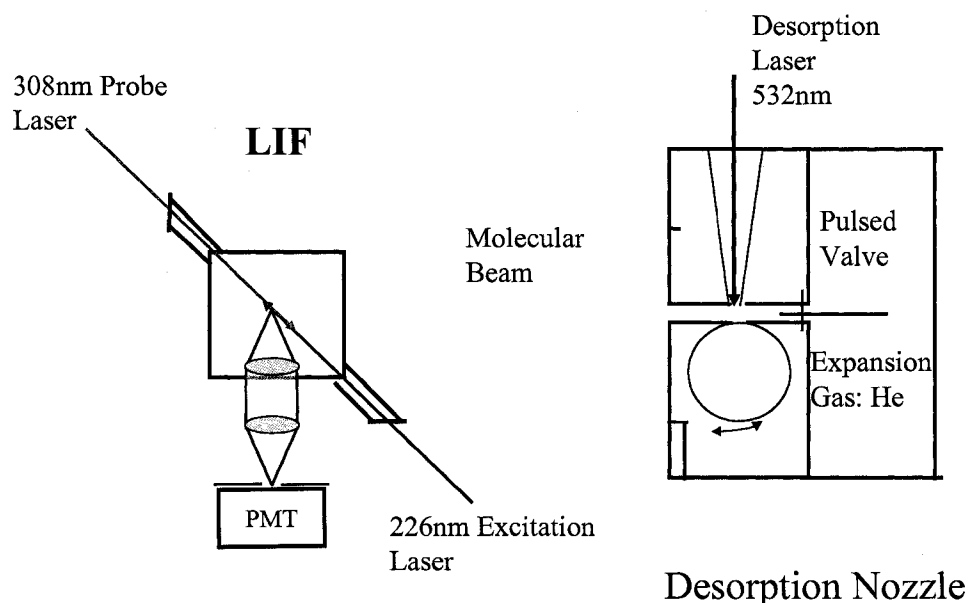


Figure 7. LIF experimental setup

A third and final set of spectroscopy experiments were performed, on the three energetic materials and the model systems, to measure the dynamics of the decomposition from their excited states. Specifically, the onset of the decomposition product NO was measured. This time resolved information yields insight into the decomposition kinetics of the excited electronic state. The pump-probe experiments were done at three different wavelengths 230 nm, 228 nm, and 226 nm, respectively. The energetic materials were placed into the gas phase using the laser desorption technique, they were cooled via the supersonic expansion, and led into the TOFMS region. The experiment consists of an excite (pump) and probe pulse both of the same wavelength.

The pump pulse excites the gas phase sample (HMX, RDX, CL-20, or model system) while the probe pulse scans for the arrival time of the initial product, the NO molecule. The appearance time of the NO molecule was measured and that time represented the decomposition dynamics of the energetic material. Figure 8 and Figure 9 are the schematics corresponding to the experimental setup and detection scheme. Figure 9 represents only one of the proposed decomposition mechanisms, the dissociated excited state decomposition, but in actuality either decomposition mechanism is probable and only one is displayed for simplicity.

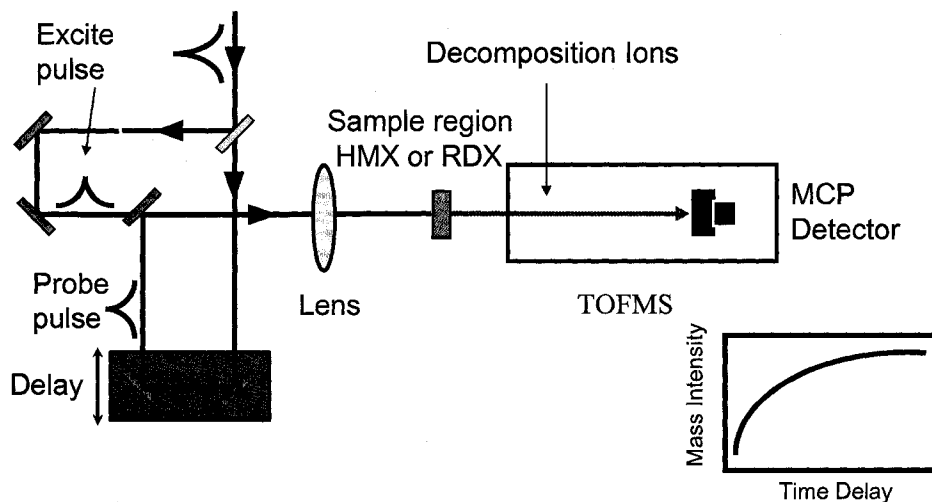


Figure 8. Femtosecond system schematic.

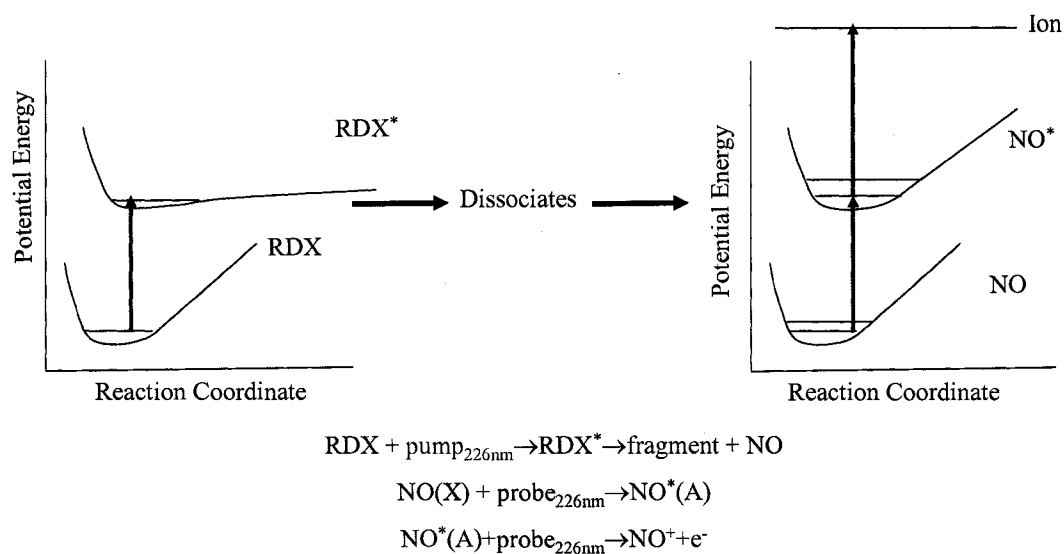


Figure 9. Femtosecond experimental scheme

Three different spectroscopy experiments on the energetic materials as well as the model systems have been completed. These experiments have produced an inclusive story indicating the energetic materials are unique. The comprehensive results of this work will be summarized in the next section. The extensive information on these experiments can be found in the following three chapters.

Summary

Decomposition of Nitramine energetic materials in excited electronic states : RDX and HMX.

Ultraviolet excitation (10 ns duration) is employed to study the decomposition of RDX (1,3,5-trinitro-1,3,5-triazacyclohexane) and HMX (1,3,5,7-tetranitro-1,3,5,7-tetrazacyclooctane) from their first excited electronic states. Isolated RDX and HMX are generated in the gas phase employing a combination of matrix assisted laser desorption and supersonic jet expansion techniques. The NO molecule is observed as one of the initial dissociation products by both time of flight mass spectroscopy and laser induced

fluorescence spectroscopy. Four different vibronic transitions of NO are observed: $A^2\Sigma(v'=0) \leftarrow X^2\Pi(v''=0,1,2,3)$. Simulations of the NO rovibronic intensities for the $A \leftarrow X$ transitions show that dissociated NO from RDX and HMX is rotationally cold (~20 K) and vibrationally hot (~1800 K). Another potential initial product of RDX and HMX excited state dissociation could be OH, generated along with NO, perhaps from an HONO intermediate species. The OH radical is not observed in fluorescence even though its transition intensity is calculated to be twice that found for NO per radical generated. The HONO intermediate is thereby found not to be an important pathway for the excited electronic state decomposition of cyclic nitramines.

Ultrafast photodissociation dynamics of HMX and RDX from their excited electronic states via femtosecond laser pump-probe techniques.

Both single UV femtosecond laser beam detection and UV/UV femtosecond laser pump-probe techniques have been employed to investigate the mechanisms and the dynamics of the photodissociation of energetic materials (HMX or RDX) from their excited electronic states. Gas phase, intact, and isolated HMX and RDX molecules are produced through the combination of two techniques: matrix assisted laser desorption and supersonic molecular beam expansion. Ion signals are detected by a time of flight mass spectrometer. Three different wavelengths (230 nm, 228 nm, and 226 nm) with pulse durations of 180 fs are used to photodissociate the HMX or RDX molecules. The only observed product is the NO molecule. The NO $A^2\Sigma \leftarrow X^2\Pi(0,0)$ transition has a resonant single photon absorption at 226 nm and non-resonance two photon absorptions occur at 228 nm and 230 nm. In the femtosecond temporal regime NO_2 gas experiments show a competition between the NO_2 ionization and NO_2 photodissociation to the NO molecule;

thus we conclude that NO₂ is not an intermediate product of the excited electronic state photodissociation of HMX or RDX. Parent HMX and RDX ions are not observed. This suggests these energetic materials do not have stable ion states, which is in good agreement with our X-ray laser single photon ionization and theoretical calculational results. Pump-probe transients of the HMX and RDX NO product at off-resonance absorption wavelengths (228 nm and 230 nm) show similar temporal widths to the cross correlation spectra taken of the laser pulse via both self-diffraction autocorrelation and non-resonance two photon absorption of furan. This indicates that the decomposition dynamics of HMX and RDX falls into the time scale of our UV femtosecond laser pulse duration (180 fs). Due to the long lifetime of the first excited electronic state of the NO molecule, the pump-probe transient of the NO product at resonance absorption wavelength is a constant, this also illustrates that HMX and RDX decompose faster than our laser pulse duration.

Comparison of Electronically Excited Photodissociation between Nitramine Energetic Materials and Model Systems

In order to elucidate the difference between the nitramine energetic materials, RDX (1,3,5-trinitro-1,3,5-triazacyclohexane), HMX (1,3,5,7-tetranitro-1,3,5,7-tetraazacyclooctane), and CL20 (2,4,6,8,10,12-hexanitro-2,4,6,8,10,12-hexaazaisowurtzitane), and the model systems, 1,4-dinitropiperazine, nitropiperidine, nitropyrrolidine and dimethylnitramine, both nanosecond mass resolved excitation spectroscopy (MRES) and femtosecond pump-probe spectroscopy have been employed. Investigation of the UV electronically excited photodissociation of these materials has presented insight into their mechanisms and dynamics. The NO molecule is a dominant decomposition product. The NO molecule from the decomposition of energetic materials

displays cold rotational and hot vibrational spectral structures. Conversely, the NO molecule from the decomposition of model systems shows relatively hot rotational and cold vibrational spectra. In addition, the intensity of the NO ion signal from energetic materials is proportional to the number of nitramine functional groups. Based upon the experimental observations and the theoretical calculations of the potential energy surfaces for these systems, we suggest that energetic materials dissociate from ground electronic states after an internal conversion from their first excited states and the model systems dissociate from their excited state. In both cases a nitro-nitrite isomerization is part of the decomposition mechanism. Parent ions of dimethylnitramine and nitropyrrolidine are observed in femtosecond experiments. All of the other molecules generate NO as a decomposition product even in femtosecond time regime. The dynamics of the decomposition is faster than 180 fs, which is equivalent to the time duration of our laser pulse.

References

- (1) Bottaro, J. In *Overviews of recent research on energetic materials*; Shaw, R. W., Brill, T. B., Thompson, D. L., Eds.; World Scientific Publishing Co.: Singapore, 2005; Vol. 16.
- (2) *Chemistry of energetic materials*; Olah; Squire, Eds.; Academic Press: New York City, 1991.
- (3) Nielsen, A. T.; Chafin, A. P.; Christian, S. L.; Moore, D. W.; Nadler, M. P.; Nissan, R. A.; Vanderah, D. J.; Gilardi, R. D.; George, C. F.; Flippen-Anderson, J. L. *Tetrahedron* **1998**, *54*, 11793.
- (4) Okovytyy, S.; Kholod, Y.; Qasim, M.; Fredrickson, H.; Leszczynski, J. *Journal of Physical Chemistry A* **2005**, *109*, 2964-2970.
- (5) Shaw, R. W. In *Overviews of recent research on energetic materials*; Shaw, R. W., Brill, T. B., Thompson, D. L., Eds.; World Scientific Publishing Co.: Singapore, 2005; Vol. 16.
- (6) Henson, B. F.; Smilowitz, L. B.; Asay, B. W.; Dickson, P. M. AIP, 2002; p 1069-10072.
- (7) Henson, B. F.; Smilowitz, L. B.; Asay, B. W.; Dickson, P. M. In *Jannaf propulsion systems hazards subcommittee meeting*; CPIA publication, 2002.
- (8) Kamlet, M. J.; Adolph, H. G. *Prop. Explos.* **1979**, *4*, 30.
- (9) Wenograd, J. *Trans. Farad. Soc* **1961**, *57*, 1612.
- (10) Kanel, G. I. *Fiz. Goreniya Vzryza* **1978**, *14*, 113.
- (11) Fristrom, R. M. *Flame Structure and Processes*; Oxford University Press: New York, 1995.
- (12) Korobeinichev, O. P. *Combustion Explosives Shock Waves* **1988**, *23*, 565.
- (13) Korobeinichev, O. P. *Pure Applied Chemistry* **1993**, *65*, 269.
- (14) Korobeinichev, O. P. *Combustion Science Technology* **1996**, *113-114*, 557.
- (15) Korobeinichev, O. P. In *Progress in Astronautics and Aeronautics*; Yang, V., Brill, T. B., Ren, W. Z., Eds.; AIAA: Reston, VA, 2000; Vol. 185.
- (16) Korobeinichev, O. P. In *Overviews of Recent Research on Energetic Materials*; Shaw, R. W., Brill, T. B., Thompson, D. L., Eds.; World Scientific Publishing Co. Pte. Ltd: Singapore, 2005; Vol. 16.
- (17) Litzinger, T. A.; Lee, Y. J.; Tang, C. J. Proceeding Workshop on the Application of Free-Jet, Molecular Beam, Mass Spectrometric Sampling, Springfield VA, 1994; p 128.
- (18) Litzinger, T. A.; Lee, Y. J.; Tang, X. J. In *Progress in Astronautics and Aeronautics*; Yang, V., Brill, T. B., Ren, W. Z., Eds.; AIAA: Reston, VA, 2000; Vol. 185.
- (19) Parr, T. P.; Hanson-Parr, D. M. In *Non-Intrusive Combustion Diagnostics*; Kuo, K. K., Parr, T. P., Eds.; Begell House Publishing Inc: New York, 1994.
- (20) Behrens, R. *Journal of Physical Chemistry* **1992**, *96*, 8877.
- (21) Zhao, X. S.; Hints, E. J.; Lee, Y. T. *Journal of Chemical Physics* **1988**, *88*, 801-810.
- (22) Maharrey, S.; Behrens, R. *Journal of Physical Chemistry A* **2005**, *109*, 11236-11249.

- (23) Bernstein, E. R. In *Overviews of Recent Research on Energetic Materials*; Shaw, R. W., Brill, T. B., Thompson, D. L., Eds.; World Scientific Publishing Co. Pte. Ltd: Singapore, 2005; Vol. 16.
- (24) Tsuoboi, Y.; Seto, T.; Kitamura, N. *Journal of Physical Chemistry* **2003**, *B107*, 7547.
- (25) Windawi, H. M.; Varma, S. P.; Cooper, C. B.; Williams, F. *Journal of Applied Physics* **1976**, *47*, 3418.
- (26) Schanda, J.; Baron, B.; Williams, F. *Acta Technica Academiae Scientiarum Hungaricae* **1975**, *80*, 185.
- (27) Schanda, J.; Baron, B.; Williams, F. *Journal of Luminescence* **1974**, *9*, 338.
- (28) Varma, S. P.; Williams, F.; Moeller, K. D. *Journal of Chemical Physics* **1974**, *60*, 4950.
- (29) Varma, S. P.; Williams, F. *Journal of Chemical Physics* **1973**, *59*, 912.
- (30) Hall, R. B.; Williams, F. *Journal of Chemical Physics* **1973**, *58*, 1036.
- (31) Williams, F. *Advanced Chemical Physics* **1971**, *21*, 289.
- (32) Dremin, A. N.; Klimenko, V. Y.; Davidoua, O. N.; Zolodeva, T. A. Proc. 9th Symp. On Detonation, Portland OR, 1989; p 319.
- (33) Sharma, J.; Beard, B. C.; Chaykovsky, M. *Journal of Physical Chemistry* **1991**, *95*, 1209.
- (34) Sharma, J.; Forbes, J. W.; Coffey, C. S.; Liddiard, T. P. *Journal of Physical Chemistry* **1987**, *91*, 5139.
- (35) Sharma, J. APS Topical Meeting on Shocks in Energetic Materials, Williamsburg VA, 1991.
- (36) Zhang, Y. X.; Bauer, S. H. *Journal of Physical Chemistry* **1997**, *B101*, 8717.
- (37) Wodtke, A. M.; Hintsä, E. J.; Lee, Y. T. *Journal of Chemical Physics* **1986**, *84*, 1044.
- (38) Wodtke, A. M.; Hintsä, E. J.; Lee, Y. T. *Journal of Physical Chemistry* **1986**, *90*.
- (39) Rice, B. M.; Thompson, D. L. *Journal of Chemical Physics* **1990**, *93*, 7986.
- (40) Loyd, S. A.; Umstead, M. E.; Lin, M. C. *Journal of Energetic Materials* **1985**, *3*, 187.
- (41) Lazarou, Y. G.; Papagiannakopoulos, P. *Journal of Physical Chemistry* **1990**, *94*, 7114.
- (42) Stewart, P. H.; Jeffries, J. B.; Zellweger, J.-M.; McMillen, D. F.; Golden, D. F. *Journal of Physical Chemistry* **1989**, *93*, 3557.
- (43) Nigenda, S. E.; McMillen, D. F.; Golden, D. F. *Journal of Physical Chemistry* **1993**, *81*, 2572.
- (44) Thompson, D. L. In *Overviews of Recent Research on Energetic Materials*; Shaw, R. W., Brill, T. B., Thompson, D. L., Eds.; World Scientific Publishing Co. Pte. Ltd.: Singapore, 2005; Vol. 16.
- (45) Oxley, J. C.; Kooh, A. B.; Szekeres, R.; Zheng, W. *Journal of Physical Chemistry* **1994**, *98*, 7004-7008.
- (46) Naud, D. L.; Brower, K. R. *Journal of Organic Chemistry* **1992**, *57*, 3303-3308.
- (47) Garland, N. L.; Ladouceur, D. H.; Nelson, H. H. *Journal of Physical Chemistry* **1997**, *A101*, 8508.
- (48) Hankin, S. M. *Rapid Communications of Mass Spectrometry* **2002**, *16*, 111.

Chapter 2: Decomposition of Nitramine energetic materials in excited electronic states: HMX and RDX

Introduction

Energetic materials such as RDX (1,3,5-trinitro-1,3,5-triazaclohexane), HMX (1,3,5,7-tetranitro-1,3,5,7-tetraazacyclooctane), and other nitramines have been intensively investigated both theoretically¹⁻⁴ and experimentally⁵⁻⁸ over the past several decades. In order to understand how shock waves and impact can initiate the rapid exothermic chemical reactions that lead to detonation in explosive solids, most of the previous studies have focused mainly on the ground electronic state in the condensed phase.⁹⁻¹⁴ Study of these materials in the condensed phase however, does not expose the difference between intra-molecular and inter-molecular behavior and the fundamental properties of these molecules. To understand the properties and reactions of energetic materials at a fundamental level, an elucidation of their molecular behavior is essential. Gas phase studies of these energetic materials can reveal the behavior of such molecular species.¹⁵ Decomposition of RDX and HMX as isolated molecules in the gas phase can be determined as a function of electronic and vibrational state excitation. A reaction mechanism can be proposed and tested for the energetic molecules of interest by further disclosing which bonds rupture first and on what time scales.

Decomposition of energetic materials from the excited state plays a very important role in the overall decomposition mechanisms and kinetics.^{5,16-19} One suggested

mechanism of detonation initiation in the condensed phase is that of “hot spot” generation.²⁰ A hot spot is presumed to be a small region in a crystal that localizes the energy of an impact/shock wave and triggers the chemical reaction. Formation of “hot spots” is thought to involve electronic excitation; several proposed mechanisms for hot spot initiation are related to excited electronic states of energetic materials.²¹⁻²² Additionally, ignition processes, such as sparks, shocks, slow/rapid heating, lasers and arcs can all initiate the decomposition reaction of energetic materials by generating excited electronic states via excitonic and HOMO/LUMO gap molecular mechanisms.²³ These dissociative and reactive excited electronic states will then generate small radicals and atoms that initiate and propagate a series of ultrafast reactions and enhance the energy release process. Generation of gas phase species is possible in all the above initiation processes. As crystal planes shear, large electric fields propagate through the crystal and excite molecules. Only a few excited state molecules are needed to generate radicals and ions to begin the rapid decomposition process for the entire sample. Thus, the decomposition of solid energetic materials should involve both ground and excited electronic states, as well as both gas and condensed phase species.²⁴⁻²⁶ An elucidation of the behavior of energetic nitramines for various applications should consider all of these circumstances and initial conditions. Therefore, isolated gas phase molecular investigations into the excited electronic states of HMX and RDX will yield an improved understanding of their molecular and condensed phase behavior at a fundamental level.

To date, theoretical investigations of unimolecular HMX in the ground electronic state show decomposition mainly through two channels: N-N bond rupture to generate NO₂; and HONO formation from a five membered ring elimination reaction.²⁷⁻³¹ For

unimolecular RDX, theoretical calculations suggest multiple decomposition pathways.³²⁻
³⁴ A few experimental gas phase, ground³⁵⁻³⁷ and excited electronic state³⁸⁻⁴¹ studies are reported. These experimental studies suggest different mechanisms depending on the electronic state of RDX: N-N bond scission to generate NO₂⁴⁰, ground electronic state concerted ring fission to generate three CH₂NNO₂³⁵ radicals, and loss of OH via a five membered ring intermediate.^{36,39} We have found that gas phase, isolated excited electronic state RDX generates NO as an initial product (~ 8 ns). NO₂ was eliminated as a possible reaction intermediate for this decomposition pathway through NO₂ decomposition studies.^{38,42} RDX and HMX can generate NO through two reaction channels: loss of O and then N-N bond scission of the unstable nitrosamine intermediate [(CH₂NNO₂)₂CH₂NNO]; and HONO loss and then fragmentation of this species to yield both OH and NO in equal amounts. This latter channel would involve the formation of the intermediate RDX and HMX five membered ring transition states [...NN(O)O...HCH...], as indicated in Figure 1, Figure 2, and Figure 3.

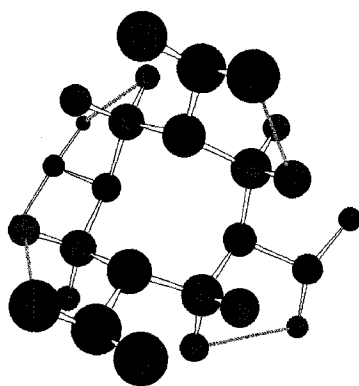


Figure 1. Delta-HMX with possible H-O bonds to form five membered ring. Oxygen (red), Nitrogen (blue), Carbon (grey), Hydrogen (aqua), possible Hydrogen-Oxygen bonds are two color (red and aqua).

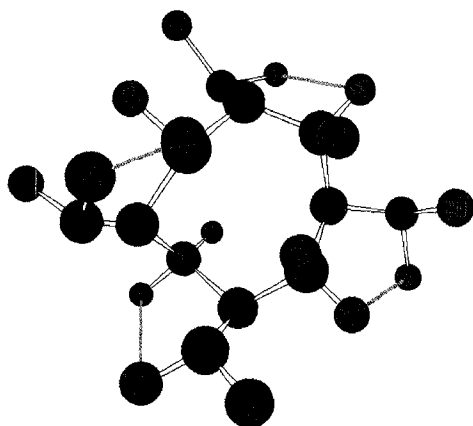


Figure 2. Beta-HMX with possible H-O bonds to form five membered ring.

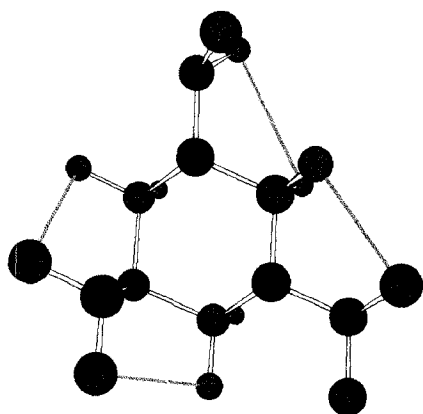


Figure 3. RDX with possible H-O bonds to form five membered rings.

In this report, we continue to pursue the isolated molecule, excited electronic state decomposition pathways for RDX and HMX on an 8 ns time scale. RDX and HMX are excited to their first excited electronic states and NO is observed by laser induced fluorescence (LIF) spectroscopy and time of flight mass spectroscopy (TOFMS). For both RDX and HMX NO is found to be rotationally cold (~ 20 K) and vibrationally hot (~ 1800 K). OH is not observed by LIF spectroscopy in the same experiments in which NO is observed. If HONO is the OH and NO precursor, the OH LIF signal should be 1.5 times as intense as the NO LIF signal. Thus we conclude that the five membered ring

elimination is not an important pathway for the decomposition of these energetic nitramines from the excited electronic state. In brief, the decomposition mechanism of RDX and HMX from their excited electronic states is apparently different than that from ground electronic states in either gas or condensed phase.

Experimental procedures

The combination of matrix assisted laser desorption and supersonic jet expansion is employed to obtain a molecular beam of a non volatile, thermally unstable sample, such as an energetic nitramine, in a vacuum chamber. The experimental set up has been described in detail in our previous publication on TOFMS of RDX and NO.³⁸ In this section we will review, briefly, the main components of this apparatus and discuss the LIF addition to the detection procedure for OH and NO. The nozzle employed for the sample beam generation is constructed from a Jordan Co. pulsed valve and a laser ablation attachment: the system is modeled after a design by Smalley and co-workers⁴³ and is discussed in references.^{44,45} The laser desorption head is attached to the front of the pulsed valve and consists of a 2 mm x 60 mm channel for the expansion gas from the nozzle, a conical channel (3 mm at the outside and 1 mm at the intersection with the expansion gas channel) for the ablation laser beam perpendicular to the expansion gas channel, and a ca. 40 mm diameter hole for the sample drum. The sample drum tangentially intersects the expansion gas channel near the middle of the laser desorption head, at the intersection of the ablation laser conical channel and the expansion gas channel. The sample drum fits into the 40 mm hole and is simultaneously rotated and translated, by a motor and gear system operating in vacuum, to present a fresh sample region to the ablation laser for each few pulses. The sample drum is electrolytically⁴⁶⁻⁴⁹

coated with a microscopically rough, porous surface of Al_2O_3 prior to sample deposition on the drum. A solution of equimolar amounts of sample (RDX or HMX) and matrix (R6G) in acetone is uniformly sprayed on the drum surface while it is rotating under a heat lamp in a fume hood. The dried drum is then placed in the laser ablation head/nozzle assembly and put into a vacuum chamber for LIF or TOFMS detection of RDX or HMX decomposition products. Under microscopic examination, the deposited sample is non crystalline, uniformly red, and completely covers the microscopically rough Al_2O_3 surface. The nitramine molecules are desorbed from the drum by laser ablation at 532 nm, entrained in the flow of He carrier gas through the 2 mm x 60 mm channel in the ablation head, and expanded into the vacuum chamber. Two chambers are used: a TOFMS and an LIF chamber, both of which has been previously described.^{38, 50-52} This procedure has been employed to detect NO for both RDX and HMX by LIF or TOFMS.

The Al_2O_3 matrix generates a very strong OH signal in LIF spectroscopy and so the matrix preparation procedure must be modified to detect OH from the energetic nitramine alone. In this instance we find that a piece of porous filter paper attached to an Al metal-surface drum gives no OH signal but that, due to the reduced roughness (surface area) of the paper with respect to the Al_2O_3 coating, the sample/matrix ratios must be changed from 1:1 to 2:1.

In addition to the 532 nm ablation laser, one or two additional lasers are required to photo excite the nitramine energetic material in the beam and then detect the fragmented small species (either NO or OH in this case). For NO detection, a single pump/probe laser is needed at 226-258 nm to both initiate dissociation of RDX and HMX

and detect NO through LIF or TOFMS ($A(v'=0) \leftarrow x(v''=0-3)$ and $I \leftarrow A$). For LIF detection of OH, two lasers are required: one at 226 nm to fragment RDX or HMX; and one at 308 nm to detect OH by LIF.

The three laser beams enter the LIF chamber by three different windows. The 226 nm photoexcitation pump laser and the 308 nm detection/probe laser for OH counter propagate and intersect the molecular beam perpendicularly at ca. 2 cm from the face of the ablation head/nozzle structure. These lasers are focused by 2 m and 1.5 m lenses, respectively, at the beam intersect position. The UV energy ranges from 0.2 to 0.6 mJ/pulse and, at the 0.5 mm focal point, the intensity of the laser beams is in the range ~ 3 to $\sim 8 \times 10^6$ W/cm² for an 8 ns pulse duration.

In both the LIF and TOFMS experiments the timing sequence for the pulsed nozzle and lasers is controlled by time delay generators (SRS DG535). The experiment is conducted at a repetition rate of 10 Hz. Ion signals, in the TOFMS, are detected by a microchannel plate (MCP) detector and fluorescence signals are detected by an RCA C31034 photomultiplier tube. Signals are recorded and processed on a PC using an ADC card (Analog Devices RTI-800) and a boxcar averager (SRS SR 250). In all experiments the chamber pressure and pulsed valve timing remain constant. For the ion velocity slip measurements, the fragment/ionization laser timing is swept.

Results and discussion

Figure 4 shows the spectra of four different $A(v'=0) \leftarrow X(v''=0,1,2,3)$ rovibronic transitions of the NO molecule generated from laser desorbed HMX excited to its first excited electronic state. All spectra show nearly the same rotational pattern but have a different vibronic intensity for each band. The intense feature in each spectrum is

assigned as the ($Q_{11}+P_{21}$) band and the lower intensity features for each vibronic transition are other rotational transitions.^{53, 54}

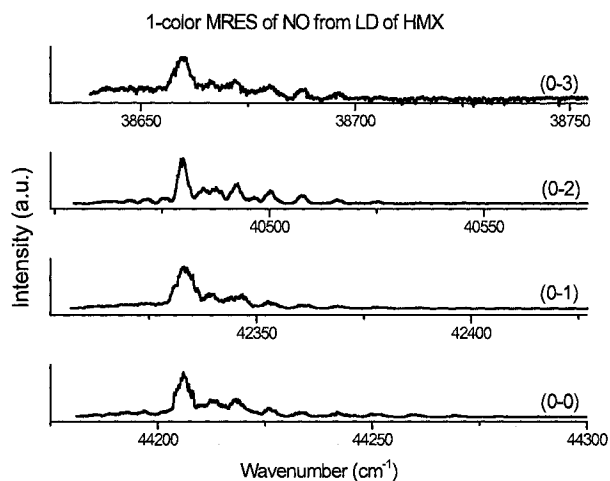


Figure 4. NO spectra A ($v' = 0$) \leftarrow X ($v'' = 0,1,2,3$), NO is generated from the photodissociation of HMX. The intensity is in arbitrary units.

The top spectrum in Figure 5 is the (0-1) transition for NO derived from laser desorbed RDX photodissociation, and the bottom spectrum of Figure 5 is for NO derived from laser desorbed and photodissociated HMX. Careful comparison between the two spectra shows that they are equivalent; this suggests that the decomposition pathway to the NO product is the same for both excited RDX and HMX.

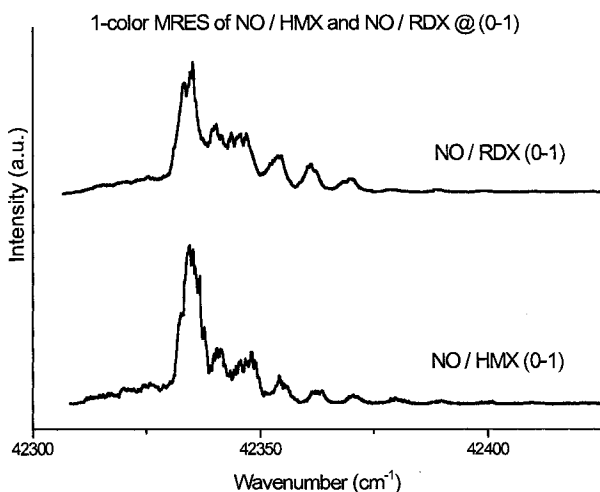


Figure 5. Comparison of NO spectra [A ($\nu' = 0$) \leftarrow X ($\nu'' = 1$)] between NO/HMX (Bottom) and NO/RDX (Top). Intensity is in arbitrary units.

Even though the matrix assisted laser desorption technique is known to place easily fragmented, fragile molecules in the gas phase without fragmentation^{55,56}, one must still ensure that RDX and HMX are not fragmented in the ablation process. That is, we must try to demonstrate that laser ablation at 532 nm (RDX and HMX do not absorb at this wavelength, while the R6G matrix does) does not generate NO in the nozzle that is then cooled in the expansion process. We must distinguish between NO generated in the nozzle by the ablation laser and NO generated at the decomposition/ionization/LIF region by the pump/probe lasers. This distinction was made for RDX at great length in our previous study, in which we also demonstrated that NO₂ was not a precursor for NO.^{38, 42} Here we briefly present three methods for making this determination: comparison of NO velocity distributions from the nozzle; determination of arrival time for the NO signal intensity as a function of nozzle/pump laser timing (velocity slip measurement); and NO rotational and vibrational temperature determinations as a function of source of NO.

Figure 6 shows that the gas phase NO signal (1% NO/99% He) from the nozzle has a much different distribution than the HMX/NO signal. Therefore, the NO signal attributed to HMX is not background NO from the nozzle expansion gas. This figure also demonstrates that the NO does not diffuse into the expansion gas after ablation, as could be anticipated for a light molecule. Thus, this result suggests that HMX is not photodissociated in the ablation process.

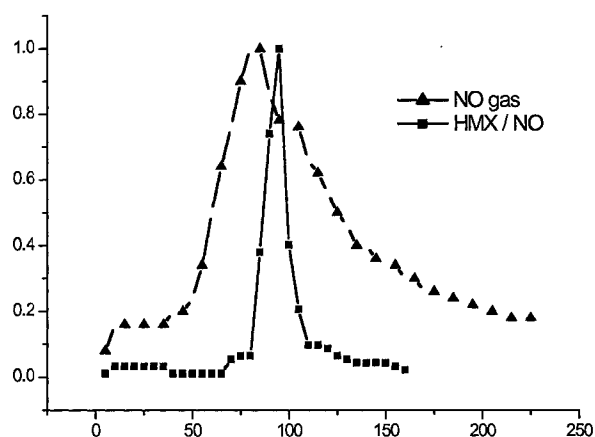


Figure 6. A comparison between the detected distributions of NO TOFMS intensity from two different sources: (1) Gas phase NO expanded through a supersonic nozzle (triangles); and (2) gas phase NO derived from MALD generated HMX fragmented at the TOFMS ion source region (squares).

Figure 7 presents data on the arrival times for NO signals derived from RDX and HMX at the ionization region of the TOFMS relative to the heavy molecule HMT (hexamethylene tetramine – $(\text{CH}_2)_6\text{N}_4 = \text{C}_6\text{H}_{12}\text{N}_4$). Both sources for the NO^+ signal have an arrival time of a heavy molecule compared to NO. A slower speed for heavy molecules in the expansion (velocity slip) is related to the molecules' mass and collision cross section,^{44, 45, 58} therefore HMT, RDX, and HMX arrive at the ionization region from the nozzle much later than a light molecule such as NO does.³⁸

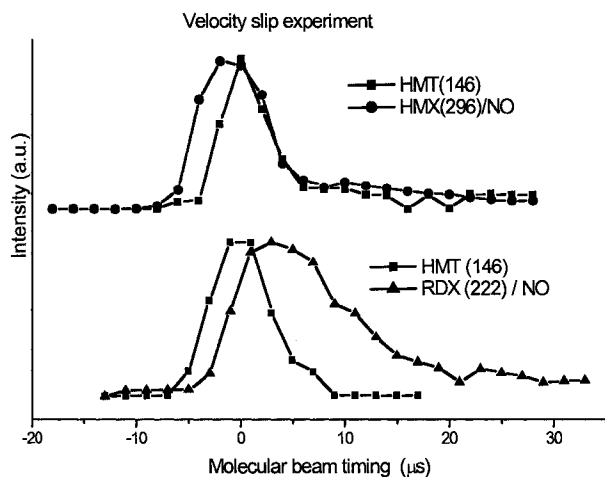


Figure 7. Velocity distribution differences between laser desorbed HMT and RDX (Bottom) or HMX (Top). Equimolar quantities of HMT and RDX/HMX samples are coated together with the matrix molecule R6G. Signals from the parent molecule for HMT, NO for RDX/HMX have been used to determine the velocity distribution data. The precise relative arrival time for HMT and RDX/HMX is determined by molecular mass and collision cross section. See text for more discussion.

Finally, one can characterize the rotational and vibrational temperatures (T_{rot} and T_{vib} , respectively) for NO under different sample and generation conditions: 1. NO mixed with the backing gas at ca. 1% in He; and 2. NO derived from laser ablated RDX or HMX fragmented at the ionization region of the TOFMS or the LIF point in the low density molecular beam. At the NO (0-0), $T_{\text{rot}} \sim 11$ K for 100 psig expansion and $\sim 1\%$ NO/99% He. This is rotationally colder than (0-0) NO from RDX or HMX for which $T_{\text{rot}} \sim 20$ K. On the other hand, T_{rot} for NO (0-1) mixed into the backing gas under these conditions is ca. 100 K, while NO from RDX and HMX remains ca. 20 K. See Figure 8. No NO (0-2,3) transitions are observed for NO mixed into the backing gas, while RDX and HMX produce (0-0), (0-1), (0-2), and (0-3) vibronic transitions with a $T_{\text{vib}} \sim 1800$ K and $T_{\text{rot}} \sim 20$ K.

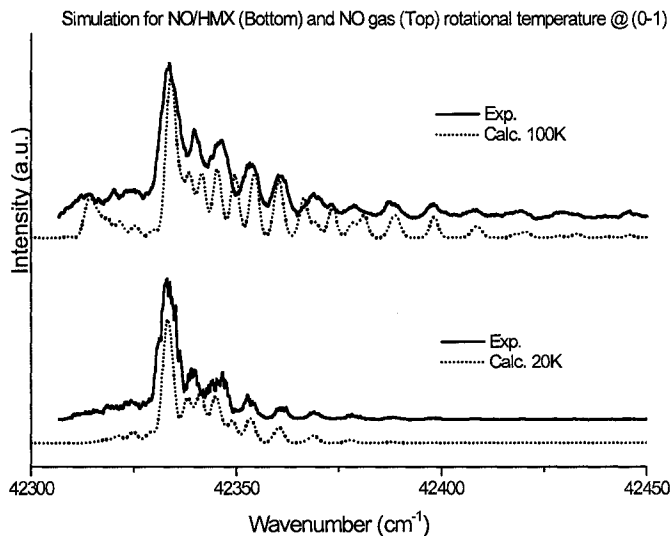


Figure 8. Simulations of the NO rotational spectra at the (0-1) transition obtained from photodissociation of HMX (Bottom) and NO gas (top). The dotted lines are the simulated spectra fit to the experimental spectra (solid line). The rotational temperatures for NO/HMX and NO gas are determined to be 20K and 100K, respectively.

These three observations, taken together, prove that NO is a primary decomposition product of RDX and HMX at the pump/probe laser access point in the ionization region of the TOFMS. The above observations are completely consistent with the LIF results. On the contrary, if the NO were generated in the nozzle by laser ablation it would have to be generated with a very cold rotational temperature and a very hot vibrational temperature that were not changed in the supersonic expansion. We consider this highly unlikely, but still indicative of the decomposition of RDX and HMX from their excited electronic states. According to the above analysis, the NO molecule is demonstrated to be an initial product of the decomposition of RDX and HMX from an isolated, excited electronic state molecule. As pointed out in the Introduction, NO has been shown not to derive from the N-N bond scission product NO_2 .^{38, 42} Another possible precursor of NO would be HONO derived from a five membered ring formation with N-N-O...H-C connectivity in the intact nitramine or from concerted ring fission to form

CH_2NNO_2 and again five membered ring connectivity. Assuming that HONO is the intermediate in the formation of NO from RDX or HMX, one should observe OH at a comparable intensity to NO. Without such a pairing of OH and NO signals, the NO must arise from loss of O and formation of an unstable nitrosamine [... $\text{H}_2\text{CN}(\text{NO})$...], which subsequently undergoes N-N bond scission to yield NO and $(\text{CH}_2\text{N}_2\text{O}_2)_2\text{CH}_2\text{N}$...

The OH radical can not be detected by TOFMS through multiphoton, stepwise absorption because the yield of OH^+ is quite small and the ionization energy for OH is 13.2 eV. LIF of OH is, however, well known and quite intense. Thus we can detect both NO and OH by LIF, to identify and observe OH and to confirm the TOFMS results for NO. The NO signal also serves as a standard signal by which one can calibrate the apparatus and the OH signal. Figure 9 illustrates the RDX NO TOFMS and LIF spectra and compares them for the (0-1) $\text{A} \leftarrow \text{X}$ transition. Although the LIF spectrum exhibits a narrower linewidth ($\sim 2 \text{ cm}^{-1}$) compared to the TOFMS linewidth ($\sim 5 \text{ cm}^{-1}$), both spectra are consistent with regard to T_{rot} and T_{vib} , based on spectral simulations. The slightly broader TOFMS linewidth than the LIF linewidth is probably due to power broadening of the TOFMS spectrum as three photons are required to generate this spectrum, and thus the focus is tighter and the intensity of the laser electric field is higher for the TOFMS detected spectrum. If HONO is the intermediate precursor to both OH and NO from these excited electronic state cyclic nitramines, the NO:OH emission ratio should be roughly 1:1.5 based on Franck-Condon factors and oscillator strengths for the respective $\text{A} \leftarrow \text{X}$ vibronic transitions. An average transition intensity for NO $\text{A} \leftarrow \text{X}$ (0-0) is ca. 200 mV on an oscilloscope. One should expect therefore to find a 300 mV OH detected

signal. No such signal is observed for OH at maximum gain on the phototube. This result is in agreement with that of ref. 36.

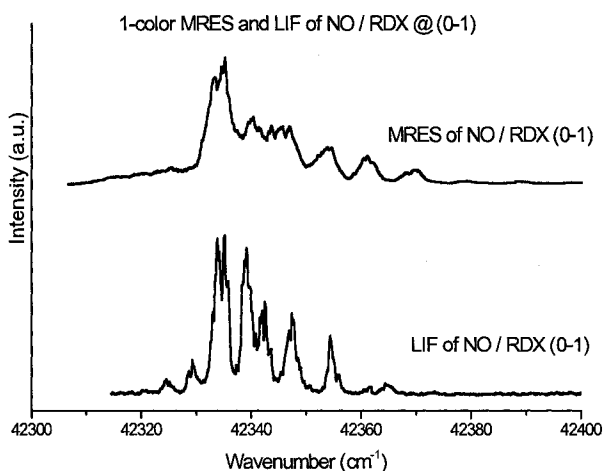


Figure 9. MRES (Top) and LIF spectrum (Bottom) of NO (0-1) transition from NO fragmented from RDX photolysis.

Conclusions

NO is observed as an initial product of 8 ns UV single photon photodissociation of HMX and RDX. NO from this process is vibrationally hot and rotationally cold. OH is not observed by LIF detection and this eliminates HONO as an intermediate precursor for NO generation. The decomposition mechanism of RDX and HMX from their excited electronic states is apparently different than that from ground electronic states in either gas or condensed phase. Further investigations are presently underway to study the NO generation from RDX and HMX with 50 fs time resolution.

References

- (1) W. Fickett, and W. C. Davis, *Detonation*, University of California Press: Los Angeles, (1979).
- (2) F. H. Ree, *J. Chem. Phys.* **81**, 1251 (1984).
- (3) Y. Kohno, K. Ueda, and A. Imamura, *J. Phys. Chem.* **100**, 4701 (1996).
- (4) D. C. Sorescu, B. M. Rice, and D. L. Thompson, *J. Phys. Chem. B* **102**, 6692 (1998).
- (5) F. J. Owens, and J. Sharma, *J. Appl. Phys.* **51**, 1494 (1979).
- (6) S. Bulusu, D. I. Weinstein, J. R. Autera, and R. W. Velicky, *J. Phys. Chem.* **90**, 4121 (1986).
- (7) J. J. Dick, R. N. Mulford, W. J. Spencer, D. R. Pettit, E. Garcia, and D. C. Shaw, *J. Appl. Phys.* **70**, 3572 (1991).
- (8) J. C. Oxley, A. B. Kooh, R. Szekers, and W. Zhang, *J. Phys. Chem.* **98**, 7004 (1994).
- (9) T. B. Brill and P. J. Brush, *Philosophical Transactions of the Royal Society of London, Series A: Mathematical, Physical and Engineering Sciences* **339**, 377 (1992).
- (10) R. Behrens, *Int. J. Chem. Kinetics* **22**, 135 (1990).
- (11) R. Behrens, S. Mack, and J. Wood, *JANNF 17th Propulsion Systems Hazards Subcommittee* **1**, 21 (1998).
- (12) R. Behrens and S. Bulusu, *Materials Research Society Symposium Proceedings* **418**, 119 (1996).
- (13) M. R. Manaa, L. E. Fried, C. F. Melius, M. Elstner, and Th. Frauenheim, *J. Phys. Chem.* **106**, 9024 (2002).
- (14) E. F. C. Byrd, G. E. Scuseria, and C. F. Chabalowski, *J. Phys. Chem.* **108**, 13100 (2003).
- (15) A. N. Ali, S. F. Son, B. W. Asay, and R. K. Sander, *J. Appl. Phys.* **97**, 1 (2005).
- (16) J. Sharma, and B. C. Beard, in *Structures and properties of Energetic Materials MRS Symposium Proceedings*, edited by D. H. Liedenber, R. W. Armstrong, and J. J. Gilman (MRS Pittsburgh, Pennsylvania, 1993).
- (17) J. J. Gilman, *Chem. Propulsion Inf. Agency* **589**, 379 (1992).
- (18) B. P. Aduiev, E. D. Aluker, G. M. Belokurov, and A. G. Krechetov, *Chem. Phys. Rep.* **16**, 1479 (1997).
- (19) A. B. Kunz, M. M. Kuklja, T. R. Botcher, and T. P. Russell, *Thermochimica Acta* **384**, 279 (2002).
- (20) F. P. Bowden, and Y. D. Yoffe, in *Initiation and Growth of Explosion in Liquids and Solids* (Cambridge University Press, London, 1952), pp. 64-65.
- (21) A. N. Dremin, *Chem. Phys. Rep.* **14**, 1851 (1995).
- (22) J. J. Gilman, *Philos. Magazine B* **79**, 643 (1999).
- (23) E. R. Bernstein, in *Overviews of Recent Research on Energetic Materials*, D. Thompson, T. Brill, and R. Shaw, Eds (World Scientific, New Jersey, 2004).
- (24) J. Sharma, and B. C. Beard, *Mater. Res. Soc. Symp. Proc.* **296**, 189 (1993).
- (25) T. R. Botcher, H. D. Landouceur, and T. R. Dussel, In *Shock Compression of*

- Condensed Matter-1997, Proceedings of the Conference of the APS Topical Group 429*, edited by S. C. Schimdt, D. P. Dankebar, and J. W. Forbes (1998), pp. 989.
- (26) B. P. Aduiev, E. D. Aluker, and A. G. Krechetov, *Chem. Phys. Rep.* **17**, 469 (1998).
 - (27) Y. Oyumi and T. B. Brill, *Combustion and Flame* **62**, 213 (1985).
 - (28) J. P. Lewis, *Chem. Phys. Lett.* **371**, 588 (2003).
 - (29) S. Zhang and T. N. Truong, *J. Phys. Chem. A* **105**, 2427 (2001).
 - (30) D. Chakraborty, R.P. Muller, S. Dasgupta, and W. A. Goddard, *J. Phys. Chem. A* **105**, 1302 (2001).
 - (31) J. P. Lewis, K. R. Glaesemann, K. VanOpdorp, and G. A. Voth, *J. Phys. Chem. A* **104**, 11384 (2000).
 - (32) D. Chakraborty, R. P. Muller, S. Dasgupta, and W. A. Goddard, *J. Phys. Chem. A* **104**, 2261 (2000).
 - (33) C. J. Wu and L. E. Fried, *J. Phys. Chem. A* **101**, 8675 (1997).
 - (34) T. D. Sewell and D. L. Thompson, *J. Phys. Chem.* **95**, 6228 (1991).
 - (35) X. Zhao, E. J. Hints, and Y. T. Lee, *J. Chem. Phys.* **88**, 801 (1988).
 - (36) H. Zuckermann, G. D. Greenblatt, and Y. Hass, *J. Phys. Chem.* **91**, 5159 (1987).
 - (37) T. A. Litzinger, B. L. Fetherolf, and Y.-J. Lee, and C. -J. Tang, *J. of Propulsion and Power* **11**, 698 (1995).
 - (38) H. -S. Im and E. R. Bernstein, *J. Chem. Phys.* **113**, 7911 (2000).
 - (39) C. Capellos, P. Papagiannakopoulos, and Y. -L. Liang, *Chem. Phys. Lett.* **164**, 533 (1989).
 - (40) C. Capellos, S. Lee, S. Bulusu, and L. Gams, *Advances in Chemical Reaction Dynamics* (Reidel, Dordrecht, 1986), pp. 398-404.
 - (41) C. Capellos, *12th International Detonation Symposium*, J.M. Short and J.L. Maienschein (Eds) (OCNR, Arlington, CA, 2003) p. 813
 - (42) H.-S. Im and E. R. Bernstein, *J. Phys. Chem. A*, **106**, 7565 (2002).
 - (43) R.E. Smalley, *Laser Chem.* **2**, 167 (1983).
 - (44) M. Foltin, G. J. Stueber, and E. R. Bernstein, *J. Chem. Phys.* **114**, 8971 (2001).
 - (45) M. Foltin, G. Stueber, and E. R. Bernstein, *J. Chem. Phys.* **111**, 9577 (1999).
 - (46) G. P. Wirtz, S. D. Brown, and W. M. Kriven, *Mater. Manuf. Processes* **6**, 87 (1991).
 - (47) P. Kurze, W. Krysmann, J. Schreckenbach, Th. Schwarz, and K. Rabending, *Cryst. Res. Technol.* **22**, 53 (1987).
 - (48) W. Krysmann, R. Kurze, K. -H. Dittrich, and H. G. Schneider, *Cryst. Res. Technol.* **19**, 973 (1984).
 - (49) K. -H. Dittrich, W. Krysmann, P. Kurze, and H. G. Schneider, *Cryst. Res. Technol.* **19**, 93 (1984).
 - (50) Q. Y. Shang and E. R. Bernstein, *Chem. Rev.* **94**, 2015-2025 (1994).
 - (51) E. R. Bernstein, *Ann. Rev. Phys. Chem.* **46**, 197 (1995).
 - (52) E. R. Bernstein, *Atomic and Molecular Clusters*, E. R. Bernstein (Ed.) (Elsevier, New York, 1990), p. 551.
 - (53) M. Hippler and J. Pfab, *Chem. Phys. Lett.* **243**, 500 (1995).
 - (54) G. Herzberg, *Spectra of Diatomic Molecules* (Van Nostrand, New York, 1950), p. 257.

- (55) P. Carcabal, R. T. Kroemer, L. C. Snoek, J. P. Simons, J. M. Bakker, I. Compagnon, G. Meijer, and G. von Helden, *Phys. Chem. Chem. Phys.* **6**, 4546 (2004).
- (56) L. C. Snoek, T. Van Mourik, and J. P. Simons, *Molec. Phys.* **101**, 1239 (2003).
- (57) Q. Y. Shang, P. O. Moreno, S. Li, and E. R. Bernstein, *J. Chem. Phys.* **98**, 1876 (1993).
- (58) a. Y. Matsuda, D. N. Shin, and E. R. Bernstein, *J. Chem. Phys.* **120**, 4142 (2004).
b. Y. Matsuda and E. R. Bernstein, *J. Phys. Chem. A*, **109**, 314 (2005).

Chapter 3: Ultrafast photodissociation dynamics of HMX and RDX from the excited electronic states via femtosecond laser pump-probe techniques.

Introduction

Energetic materials such as HMX (1,3,5,7-tetranitro-1,3,5,7-tetrazacyclooctane) and RDX (1,3,5-trinitro-1,3,5-triazacyclohexane) have broad applications as explosives and fuels. In order to understand how the chemical energy in these materials converts into mechanical energy and improve the efficiency of using them in explosion and combustion applications, much effort has been expended on the elucidation of the decomposition mechanisms and dynamics of HMX and RDX both experimentally and theoretically in the past decades.¹⁻⁸ The following initial steps in the decomposition mechanism for the ground electronic states have been proposed: N-N bond fission to generate the NO₂ molecule;⁹ formation of a five-membered ring to generate an HONO intermediate which then decomposes to NO and OH;^{10,11} and concerted symmetric ring fission to form three CH₂NNO₂.¹² Although the decomposition of energetic materials from their excited electronic states plays a very important role in the detonation of these materials,¹³⁻¹⁶ only a few studies of these excited state processes have been pursued. We have done several useful and informative experiments to investigate the initial steps in the photodissociation of both HMX and RDX from their first excited electronic states using ns laser pulses.^{17,18} Results, for both energetic materials, show that the NO molecule is one of the initial decomposition products, while NO₂ and HONO have been

ruled out as potential intermediates of the initial NO product. Two possible mechanisms for the NO product are N-N bond fission of the unstable nitrosamine intermediate $[(\text{CH}_2\text{NNO}_2)_3\text{CH}_2\text{NNO}]$ which occurs after an O atom loss from the HMX or RDX molecule, and isomerization of the RNNO_2 intermediate to RNONO with subsequent NO release.

Detonation of energetic materials is an ultrafast process, therefore, not only the mechanisms, but also the dynamics of the decomposition of these materials are important. As mentioned above, mechanistic studies have been widely performed, but currently the dynamics of the decomposition of both HMX and RDX have not been directly measured due, in part, to the limitation of the time resolution of the experimental techniques. A few hundred femtoseconds is a proposed time regime for the initial decomposition step of these energetic materials.¹⁹ With the rapid development of femtosecond laser technology, one can measure the ultrafast dynamics of interesting systems using pump-probe techniques.²⁰ In this work, femtosecond pump-probe techniques are employed to investigate the decomposition dynamics of HMX and RDX. Single UV femtosecond laser beam detection shows the NO molecule is the only observed product from the excited electronic state decomposition of either HMX or RDX. Parent ions are not observed. Femtosecond laser pump-probe experiments at three wavelengths (226 nm, 228 nm, 230 nm) are carried out to monitor the time evolution of the NO product appearance in an effort to determine the dynamics of the decomposition of both HMX and RDX. The NO molecule has a resonant $\text{A}^2\Sigma \leftarrow \text{X}^2\Pi$ (0, 0) transition at 226 nm and off-resonance two-photon absorption at 228 nm and 230 nm. The pump-probe transients for the NO product at both resonance and off-resonance absorption wavelengths show that the dynamics of

the decomposition of HMX and RDX falls into the time scale of our laser pulse duration (180 fs).

Experimental procedures

The experimental set-up consists of a femtosecond laser pump-probe system, a laser desorption supersonic jet expansion nozzle, and a time of flight mass spectrometer (TOFMS). The intact, gas phase, and isolated HMX or RDX molecules are produced through the combination of matrix assisted laser desorption (MALD) and supersonic jet expansion. The MALD method has been proven to be a good technique for placing non-volatile, thermally unstable samples into the gas phase in a vacuum chamber.^{21, 22} The laser desorption supersonic jet expansion nozzle and the TOFMS have been described in detail in our previous publications.^{17,18} The femtosecond laser system consists of a self mode-locked Ti:Sapphire oscillator (KM Labs) that is pumped by a 4.75 W diode laser (Coherent, Verdi) at 532 nm and generates femtosecond laser pulses with center wavelength of 810 nm, output power of 430 mW and repetition rate of 91 MHz. A home-made ring cavity Ti:Sapphire amplifier, which is pumped by the second harmonic of a 10 Hz Nd:YAG laser (Quanta Ray GCR), is employed for pulse amplification. The amplified pulse has an energy of 1.5 mJ with a 10 Hz repetition rate and a temporal width of <30 fs. A commercial traveling optical parametric amplifier of super fluorescence (TOPAS, Light Conversion) system is used for wavelength extension. The three wavelengths (226 nm, 228 nm and 230 nm) used in this work are deep UV outputs from the TOPAS and are used as the fragmentation/ionization source for the time resolved TOFMS experiments. To avoid absorption saturation, the power density is maintained at $1.3 \times 10^{13} \text{ Wcm}^{-2}$.

The pulse duration of the UV laser pulses has been measured to be ~ 180 fs using a self-diffraction (SD) autocorrelator²³ and the off-resonance two-photon absorption of the furan molecule. The two methods use the same pump-probe optical system as the femtosecond laser pump-probe experiments in which both pump and probe beams have the same wavelength. The autocorrelation trace is obtained by recording the signal intensity versus the delay time between the two beams. A self diffraction signal appears when two beams are overlapped both spatially and temporally on a thin quartz diffraction medium. The maximum signal position is determined to be the zero delay time for the pump-probe system. Figure 1 (a) is a typical SD autocorrelation trace (circles) with a Gaussian shape fitting (solid line) that shows a width (FWHM) of 254 fs, which yields a laser pulse duration of 180 fs. The off-resonance two-photon absorption of the furan molecule shows an absorption signal enhancement when the two beams are overlapped in the ionization region of the TOFMS. The enhanced absorption signal (Figure 1 (b)) displays similar laser pulse duration to that measured by SD autocorrelation. In the femtosecond UV/UV pump-probe experiments on HMX and RDX, the sample molecules are excited by the pump beam, and fall apart according to their photodissociation dynamics. Photodissociation products are further photoionized by the delayed probe beam and detected via the TOFMS. By delaying the probe beam with respect to the pump beam, product appearance time can be determined.

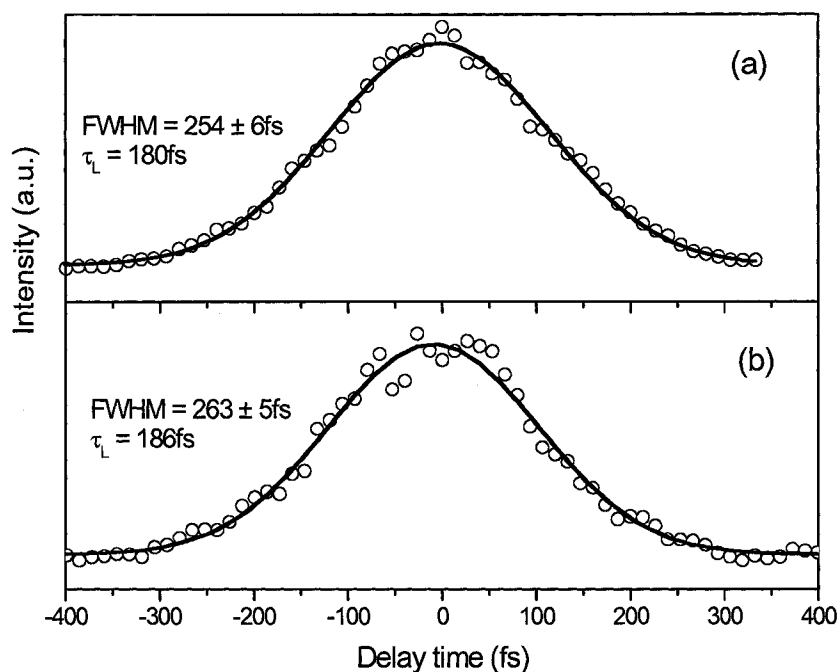


Figure 1. Measurements of the femtosecond laser pulse duration at 226 nm using a self diffraction autocorrelator (a) and off-resonance two photon absorption of the furan molecule (b).

The experiment is run at a repetition rate of 10 Hz. The 10 Hz trigger source derives from the 91 MHz pulse train. The timing sequence for the pulsed nozzle and the ablation laser is controlled by a time delay generator (SRS DG535). Ion signals are detected by a microchannel plate detector (MCP). Signals are recorded and processed on a PC using an ADC card (Analog Devices RTI-800) and a box car averager (SRS SR 250). The delay time between the pump and probe beam is controlled by a micro translation stage (Thorlabs: LNR50SEK1) and a step size of 13 femtoseconds is used. Each point on the pump-probe transient corresponds to an average intensity resulting from 100 laser shots.

Computational procedures

The theoretical ion state calculation of RDX molecule is based on the optimized ground state geometry of its AAA conformer, which is suggested as a possible structure

for RDX in the vapor phase and has been calculated by B. M. Rice and C. F. Chabalowski²⁴. Single point energy calculations and ion state geometry optimizations are performed via the Gaussian 98 program²⁵ at the B3LYP density functional level^{26,27} with a 6-31G* basis set.²⁸⁻³⁰

Results and discussion

Figure 2 shows mass spectra obtained from the photodissociation of HMX and NO₂ gas. Spectra were taken using a single femtosecond laser beam at 226 nm. The NO molecule is the only observed product from the UV photodissociation of not only the HMX molecule but also the RDX molecule. Although the MALD technique is a good method to place easily fragmented, fragile molecules in the gas phase without fragmentation, great efforts are taken in our previous work to ensure that HMX or RDX are not fragmented in the ablation process.^{17,18} Three different methods have been employed to explore this issue: comparison of NO velocity distributions from the nozzle; determination of arrival time for the NO signal intensity as a function of nozzle/pump laser timing; and NO rotational and vibrational temperature determinations as a function of source of NO. These methods demonstrate that NO from HMX and RDX is generated at the decomposition/ionization region rather than in the ablation nozzle.

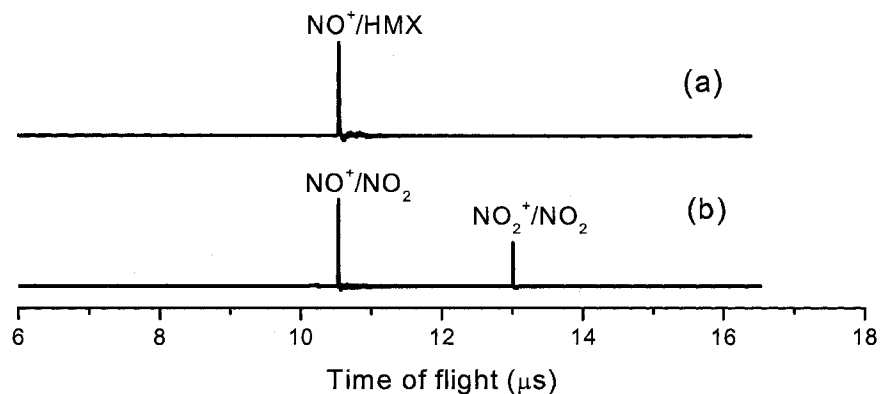


Figure 2. Mass spectra of NO from the photodissociation of HMX (a) and NO₂ gas (b) using femtosecond laser pulses at 226 nm.

Neither the HMX nor the RDX parent ion is observed even though femtosecond laser pulses are employed for ionization. This suggests that HMX and RDX do not have a stable ion state when excited by UV light. X-ray laser (25.6 eV) single photon ionization experiments have proven to be an excellent method to prevent fragmentation due to multi-photon absorption even for weakly bound van der Waals clusters,³¹ and therefore this X-ray laser is also employed to photoionize HMX and RDX molecules. The parent ions of these molecules are not observed by either fs or X-ray laser ionization.

In order to further confirm our unstable ion state observation, non-local density functional calculations have been performed using a B3LYP method and the 6-31G* basis set. Single point energy calculation and geometry optimization of RDX ion state give vertical and adiabatic ionization energies of 10.28 and 9.89 eV, respectively; however, the optimized geometry of the RDX ion state shows that two NO₂ (i.e., NO + O) fragments are separated from the parent, illustrating that the RDX ion state is not stable at this level of theory. Therefore our experimental observation is in good agreement with the calculational result.

For NO₂ gas fs ionization TOFM spectrum, both NO and NO₂ ions are observed indicating that two different processes occur simultaneously at the femtosecond time scale: one is NO₂ photodissociation into NO and O, and the other is direct NO₂ ionization. This is different from energy resolved (nanosecond) laser experiments, for which only the NO ion signal is observed.¹⁷ Ledingham and co-workers have done a comparison of femto-, pico- and nano-second multiphoton ionization and dissociation of NO₂ at 248 and 496 nm.³² At 248 nm, they observed the NO₂/NO ion ratio varied from 1% using nanosecond laser pulses to about 60% for 300 fs laser pulses. Both ours and Ledingham's observations for NO₂ gas show a strong competition between NO₂ ionization and NO₂ photodissociation into the NO molecule if femtosecond laser pulses are used. Since the NO₂ ion has not been observed from the photodissociation of HMX or RDX, we conclude that the NO₂ molecule is not the intermediate for the initial decomposition product, the NO molecule, of either HMX or RDX even in femtosecond temporal regime.

Femtosecond pump-probe experiments on the decomposition of HMX and RDX are carried out at three different wavelengths (230 nm, 228 nm and 226 nm). For each wavelength, the laser beam is split into pump and probe beams. The gas phase HMX or RDX molecule is pumped to its first excited electronic state by the pump beam, it then dissociates into products according to corresponding mechanisms and dynamics. The probe beam is used to excite and ionize the initial products so that the dissociation dynamics can be monitored. Assuming the decomposition of HMX and RDX takes a much longer time than the laser pulse duration, we should be able to observe the buildup of the product signal as the delay time between the pump and probe beams is varied. The

NO product is selected to monitor the dynamics of the decomposition process. The pump-probe transients for both molecules are obtained by recording the NO ion signal versus the delay time between the pump and probe beams and have been found to be equivalent. Figure 3 (a) and (b) show the pump-probe transients for the NO product of HMX at 228 nm and 230 nm, respectively. Circles correspond to experimental measurements, and the solid lines are the Gaussian-fitted results. Instead of a buildup of NO signal, an enhancement of signal intensity is observed around zero delay time. The transients display a symmetric Gaussian shape because both pump and probe beams are identical in these experiments. These two wavelengths (228 nm and 230 nm) are off-resonance for the NO molecular transition and ionization of the NO molecule requires two photons; therefore, off-resonance two-photon absorption enhancement occurs when the pump and probe beams are overlapped both temporally and spatially. The Gaussian full widths at half maximum for the transients at 228 nm and 230 nm are 240 fs and 250 fs, respectively. Both results are consistent, within experimental uncertainty, with the autocorrelation and cross correlation measurements recorded for the time duration of the UV femtosecond laser pulses. Thus we conclude that the dynamics of the decomposition of HMX as well as RDX fall into the time scale of the present pulse duration of our UV femtosecond laser, and the off-resonant two-photon absorption of the NO product becomes equivalent to the measurement of the time duration of the laser pulses.

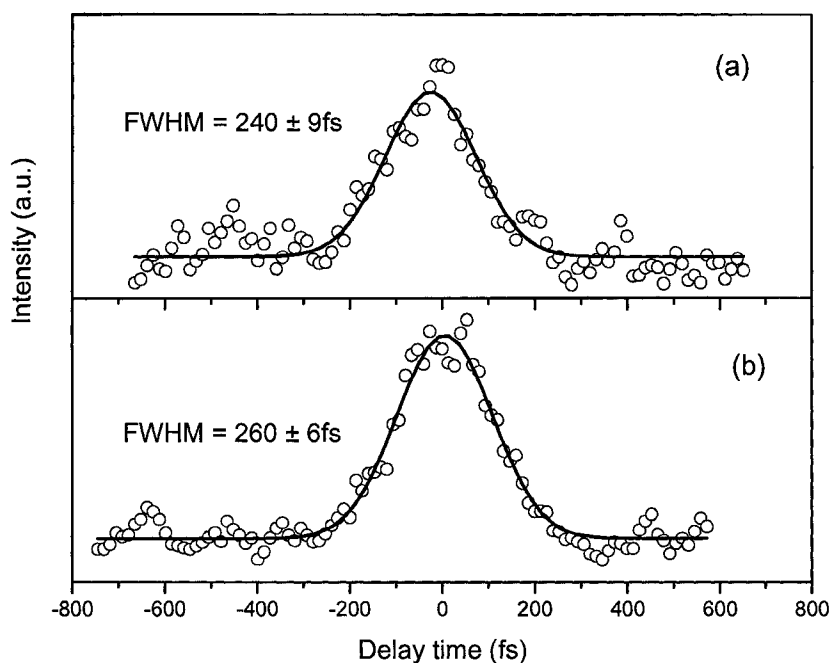


Figure 3. Femtosecond pump-probe transients for the NO molecule from the photodissociation of HMX at 228 nm (a) and 230 nm (b). At both wavelengths, off-resonance two-photon absorption occurs. Similar results have been observed for RDX.

The pump-probe transients for NO gas (a) and the NO product of RDX (b) at 226 nm are shown in Figure 4 and are illustrated as a fluctuating flat line. The NO $A^2\Sigma \leftarrow X^2\Pi$ (0, 0) transition has a resonance single-photon absorption occurring at 226 nm; therefore, if the decomposition of either HMX or RDX occurs much faster than the laser pulse duration, measurements will show the lifetime of the first excited state of the NO molecule rather than the onset dynamics of the decomposition process. From the fluorescence lifetime measurement of the first excited state of the NO molecule, we know the lifetime of this state is in the hundreds of ns range, so the NO ion signal should remain almost constant within the scanned delay time range (± 1 ps). This is consistent with our observation, which indicates the dynamics of the decomposition of both HMX and RDX is faster than our laser pulse. In brief summary, both on-resonance and off-resonance wavelengths measurements illustrate that the decomposition of HMX and

RDX falls within the time scale of our femtosecond laser pulse duration (180 fs). Note that shorter fs laser pulses may not resolve this time scale because of uncertainty principle constraints and coherence/wavepacket dynamics for dissociative states.

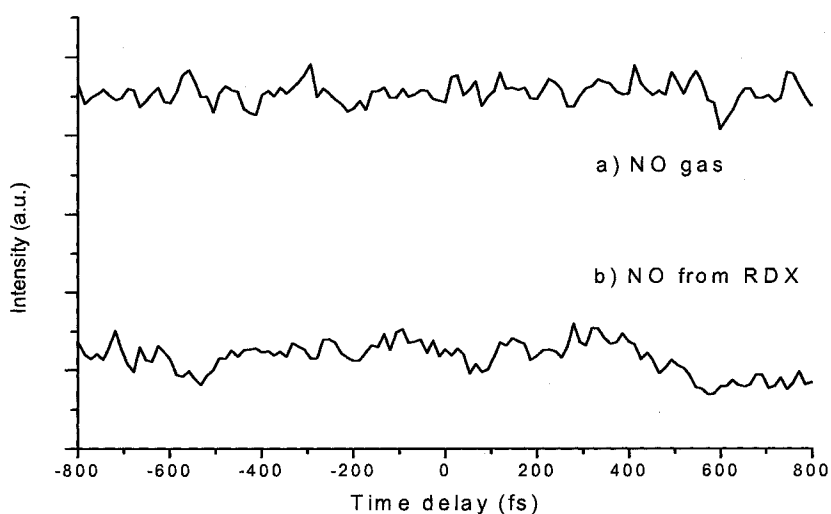


Figure 4. 226 nm fs pump-probe transients for NO gas (a) and the NO product of RDX (b).

Conclusions

The NO molecule is the only observed product from the UV femtosecond laser photodissociation of HMX and RDX using both off-resonant and resonant absorption wavelengths for the NO transition. NO₂ is ruled out as the intermediate for the NO product even in the femtosecond temporal regime. HMX and RDX parent ions are not observed. This suggests these molecules do not have stable ion states when excited by UV light. The pump-probe transients for the NO product at both off-resonant and resonant wavelengths indicate that the decomposition dynamics of either HMX or RDX falls within the time scale of our femtosecond laser pulse duration (180 fs).

References

- (1) F. J. Owens, and J. Sharma, *J. Appl. Phys.* 51 (1979) 1494.
- (2) S. Bulusu, D. I. Weinstein, J. R. Autera, and R. W. Velicky, *J. Phys. Chem.* 90 (1986) 4121.
- (3) J. J. Dick, R. N. Mulford, W. J. Spencer, D. R. Pettit, E. Garcia, and D. C. Shaw, *J. Appl. Phys.* 70 (1991) 3572.
- (4) J. C. Oxley, A. B. Kooh, R. Szekers, and W. Zhang, *J. Phys. Chem.* 98 (1994) 7004.
- (5) W. Fickett, and W. C. Davis, *Detonation*, University of California Press, Los Angeles, 1979.
- (6) F. H. Ree, *J. Chem. Phys.* 81 (1984) 1251.
- (7) Y. Kohno, K. Ueda, and A. Imamura, *J. Phys. Chem.* 100 (1996) 4701.
- (8) D. C. Sorescu, B. M. Rice, and D. L. Thompson, *J. Phys. Chem. B* 102 (1998) 6692.
- (9) C. Capellos, S. Lee, S. Bulusu, and L. Gams, *Advances in Chemical Reaction Dynamics*, Reidel, Dordrecht, 1986, p. 398.
- (10) H. Zuckermann, G. D. Greenblatt, and Y. Haas, *J. Phys. Chem.* 91 (1987) 5159.
- (11) C. Capellos, P. Papagiannakopoulos, and Y. -L. Liang, *Chem. Phys. Lett.* 164 (1989) 533.
- (12) X. Zhao, E. J. Hints, and Y. T. Lee, *J. Chem. Phys.* 88 (1988) 801.
- (13) J. Sharma, and B. C. Beard, in *Structures and properties of Energetic Materials MRS Symposium Proceedings*, edited by D. H. Liedenberg, R. W. Armstrong, and J. J. Gilman, MRS Pittsburgh, Pennsylvania, 1993.
- (14) J. J. Gilman, *Chem. Propulsion Inf. Agency* 589 (1992) 379.
- (15) B. P. Aduiev, E. D. Aluker, G. M. Belokurov, and A. G. Krechetov, *Chem. Phys. Rep.* 16 (1997) 1479.
- (16) A. B. Kunz, M. M. Kuklja, T. R. Botcher, and T. P. Russell, *Thermochimica Acta* 384 (2002) 279.
- (17) H.-S. Im and E. R. Bernstein, *J. Chem. Phys.* 113 (2000) 7911.
- (18) Y. Q. Guo, M. Greenfield, and E. R. Bernstein, *J. Chem. Phys.* 122 (2005) 244310.
- (19) G. P. Wakeham, D. D. Chung, and K. A. Nelson, *Thermochimica Acta* 384 (2002) 7.
- (20) A. H. Zewail, *J. Phys. Chem. A* 104 (2000) 5660.
- (21) P. Carcabal, R. T. Kroemer, L. C. Snoek, J. P. Simons, J. M. Bakker, I. Compagnon, G. Meijer, and G. von Helden, *Phys. Chem. Chem. Phys.* 6 (2004) 4546.
- (22) L. C. Snoek, T. Van Mourik, and J. P. Simons, *Molec. Phys.* 101 (2003) 1239.
- (23) R. Trebino, *Frequency-Resolved Optical Gating: The measurement of ultrafast laser pulses*, Kluwer Academic Publisher, Boston, 2000.
- (24) B. M. Rice, and C. F. Chabalowski, *J. Phys. Chem. A* 101 (1997) 8720.
- (25) Gaussian 98, M. J. Frisch, G. W. Trucks, H. B. Schlegel, G. E. Scuseria, M. A. Robb, J. R. Cheeseman, V. G. Zakrzewski, J. A. Montgomery, R. E. Stratmann, J. C. Burant, S. Dapprich, J. M. Millam, A. D. Daniels, K. N. Kudin, M. C. Strain, O. Farkas, J. Tomasi, V. Barone, M. Cossi, R. Cammi, B. Mennucci, C. Pomelli,

- C. Adamo, S. Clifford, J. Ochterski, G. A. Petersson, P. Y. Ayala, Q. Cui, K. Morokuma, D. K. Malick, A. D. Rabuck, K. Raghavachari, J. B. Foresman, J. Cioslowski, J. V. Ortiz, B. B. Stefanov, G. Liu, A. Liashenko, P. Piskorz, I. Komaromi, R. Gomperts, R. L. Martin, D. J. Fox, T. Keith, M. A. Al-Laham, C. Y. Peng, A. Nanayakkara, C. Gonzalez, M. Challacombe, P. M. W. Gill, B. G. Johnson, W. Chen, M. W. Wong, J. L. Andres, M. Head-Gordon, E. S. Replogle and J. A. Pople, Gaussian, Inc., Pittsburgh PA, 1998.
- (26) A. D. McLean, and G. S. Chandler, *J. Chem. Phys.* 72 (1980) 5639.
- (27) R. Krishnan, J. S. Binkley, R. Seeger, and J. A. Pople, *J. Chem. Phys.* 72 (1980) 650.
- (28) W. J. Hehre, R. Ditchfield, and J. A. Pople, *J. Chem. Phys.* 56 (1972) 2257.
- (29) P. C. Hariharan, and J. A. Pople, *Theor. Chem. Acta* 28 (1973) 213.
- (30) M. S. Gordon, *Chem. Phys. Lett.* 76 (1980) 163.
- (31) F. Dong, S. Heinbuch, J. J. Rocca, and E. R. Bernstein, *J. Chem. Phys.* 124 (2006).
- (32) K. W. D. Ledingham, C. Kosmidis, S. Georgiou, S. Couris, R. P. Singhal, *Chem. Phys. Lett.* 247 (1995) 555.

Chapter 4: Comparison of Electronically Excited Photodissociation between Nitramine Energetic Materials and Model Systems

Introduction

Nitramine energetic materials, such as RDX (1,3,5-trinitro-1,3,5-triazacyclohexane), HMX (1,3,5,7-tetranitro-1,3,5,7-tetraazacyclooctane), and CL-20 (2,4,6,8,10,12-hexanitro-2,4,6,8,10,12-hexaazaisowurtzitane), have broad applications as explosives and fuels due to their high density and high energy. Except for the number of nitramine functional groups, these materials have similar structures which are shown in Figure 1. As older and simpler nitramine energetic materials, RDX and HMX have been intensively investigated both theoretically and experimentally over the past decades¹⁻⁸. These studies involve the decomposition of RDX and HMX from both ground and excited electronic states, either in the condensed phase or in the gas phase. Studies in the condensed phase help in understanding how shock waves and impact can initiate the rapid exothermic chemical reactions that lead to detonation in explosive solids. On the other hand, studies in the gas phase reveal the properties and reactions of the energetic materials at a molecular level, and determine the decomposition mechanism and dynamics as a function of electronic and vibrational state excitations.

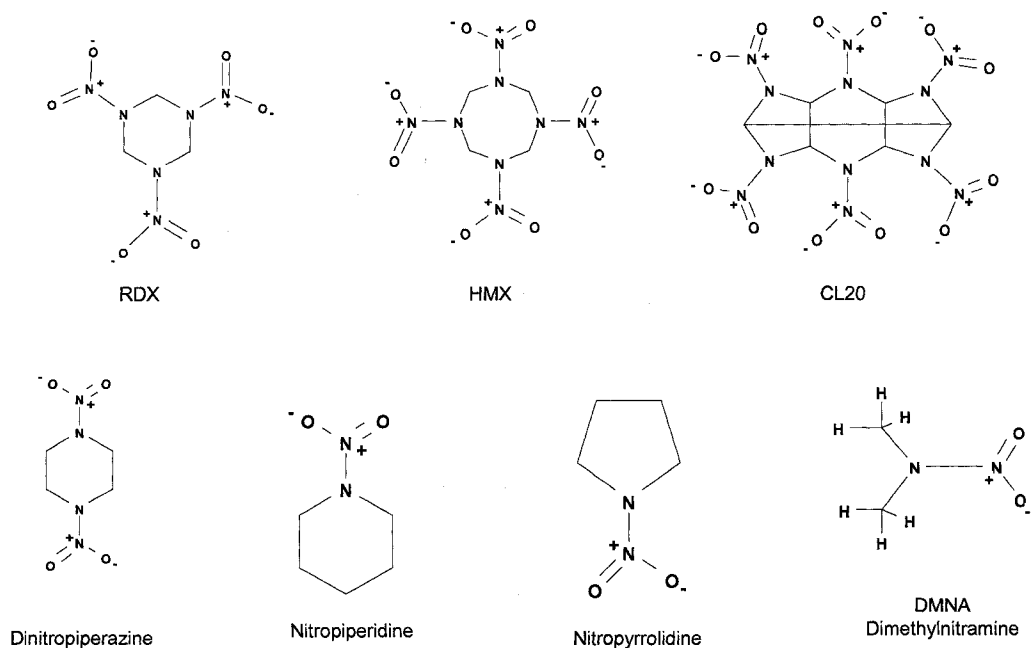


Figure 1. Chemical Structures of Energetic Materials (RDX, HMX, and CL-20) and the Model Systems (Dinitropiperazine, Nitropiperidine, Nitropyrrolidine, and Dimethylnitramine (DMNA))

Although there have been many experimental and theoretical advances in understanding the initiation chemistry within energetic materials, the mechanisms of the decomposition of these nitramines still remains uncertain. The following three initial steps in the decomposition of RDX and HMX from their ground electronic states have been proposed: (1) N-N bond fission to generate the NO_2 molecule⁹; (2) formation of a five-membered ring to generate the HONO intermediate which then decomposes to NO and OH^{10,11}; and (3) concerted symmetric ring fission to form three CH_2NNO_2 ¹². Electronic excitation has been experimentally proven to play an important role in the initiation process of the detonation of energetic materials¹³⁻²². In order to understand the decomposition of gas phase energetic materials from their excited states, we have done several useful and informative experiments to reveal the initial steps in the photodissociation of RDX and HMX from their first excited electronic states²³⁻²⁵. Results

show that the NO molecule is one of the initial decomposition products, while NO₂ and HONO have been ruled out as potential intermediates of the initial NO product. Two possible mechanisms for the NO product are N-N bond fission of the unstable nitrosamine intermediate [(CH₂NNO₂)₂CH₂NNO or (CH₂NNO₂)₃CH₂NNO] which occurs after an O atom loss from the RDX or HMX molecule, and nitro-nitrite isomerization of the RDX or HMX molecule with subsequent release of NO.

As a new and polycyclic energetic nitramine, CL-20 is expected to replace RDX and HMX in many applications due to its superior explosive performance. Although some theoretical studies^{26,27} of CL-20 have been pursued since it was first synthesized in 1987²⁸, only a few experimental studies have been done on the decomposition of this energetic material²⁹. Theoretical investigation shows CL-20 has ground electronic state decomposition mechanisms similar to RDX and HMX³⁰.

Model systems, including 1,4-dinitropiperazine, nitropiperidine, nitropyrrolidine and dimethylnitramine, have similar molecular structure to the above energetic materials (shown in figure 1), however they are unable to be used as fuels and explosives. In order to elucidate the difference between the energetic materials and model systems, we have experimentally and theoretically investigated the decomposition mechanisms and dynamics of both the energetic materials and the model systems from their excited electronic states. Presently, both nanosecond mass resolved excitation spectroscopy (MRES) and femtosecond pump-probe spectroscopy in the UV spectral region have been employed to investigate the mechanisms and dynamics of the electronically excited photodissociation of CL-20 and the model systems. The only difference between CL-20 and RDX and HMX is its more intense experimental NO⁺ ion signal, thus the

decomposition behavior of CL-20 from its excited electronic state is the same as RDX and HMX^{24,25}. In the ns MRES experiments, the dominant decomposition product for both the energetic materials and model systems is the NO molecule. However the NO molecule from the decomposition of the energetic materials displays contrary rotational and vibrational spectral properties to that of the model systems. Potential energy surface calculations on RDX and various model systems using density functional theory propose the nitramine energetic materials might dissociate from their ground electronic state with highly excited vibrational levels after an internal conversion from their first excited electronic state, while model systems dissociate from their excited electronic states. In both cases, a nitro-nitrite isomerization is part of the decomposition mechanism. Parent ions of dimethylnitramine and nitropyrrolidine are observed in femtosecond experiments. All of the other molecules generate NO as a decomposition product even in the femtosecond time regime. The dynamics of the production of the NO molecule is faster than 180 fs, which is equivalent to the time duration of our laser pulse.

Experimental Procedures

Detailed procedures for both the ns MRES and femtosecond pump-probe spectroscopy experiments have been described in our previous publications²³⁻²⁵. Only the main components of the apparatus and some changes that have been made in this experiment will be briefly reviewed in this section. The experimental set-up consists of laser systems with both ns and fs time duration, a laser desorption supersonic jet expansion nozzle, and a time of flight mass spectrometer. The intact, gas phase, isolated, and neutral nitramine energetic material molecules are produced through the combination of matrix assisted laser desorption (MALD) and supersonic jet expansion. Due to the low

vapor pressure of 1,4-dinitropiperazine it has also been placed into gas phase using the MALD technique. The nozzle employed for the sample beam generation is constructed from a Jordan CO. pulsed valve and a laser desorption attachment^{31,32}. The laser desorption head is attached to the front of the pulsed valve and consists of a 2 mm x 60 mm channel for the expansion gas from the nozzle, a conical channel (3 mm at the outside and 1 mm at the intersection with the expansion gas channel) for the desorption laser beam perpendicular to the expansion gas channel, and a ca. 40 mm diameter hole for the sample drum. The sample drum tangentially intersects the expansion gas channel near the middle of the laser desorption head, at the intersection of the desorption laser conical channel and the expansion gas channel. The sample drum fits into the 40 mm hole and is simultaneously rotated and translated, by a motor and gear system operating in vacuum, to present a fresh sample region to the desorption laser for each few pulses. In our previous experiments, a solution of equimolar amounts of sample and matrix (R6G) in acetone is uniformly sprayed on an Al₂O₃ coated drum³³⁻³⁶. In this experiment, we prepare all the sample drums by wrapping a piece of porous filter paper around a clean aluminum drum. The filter paper is preferred over the Al₂O₃ coated drum for two reasons: (1) the procedure for preparing Al₂O₃ coated drum is time consuming and it is difficult to clean the residual solution from the electrolytic coating process, which produces interference ion signals; and (2) we find that a piece of porous filter paper produces gas phase molecules in amounts similar to the coated drum. The dried drum is then placed in the laser ablation head/nozzle assembly and put into a vacuum chamber. The TOFMS experiment on the nitramine molecule decomposition products can then be performed. The nitramine molecules are desorbed from the drum by laser desorption at

532 nm, entrained in the flow of a helium carrier gas through the 2 mm x 60 mm channel in the ablation head, and expanded into the vacuum chamber^{37,38}. The other model systems are heated to about 350 K in a glass vial outside the nozzle and brought into the molecular beam by a helium carrier gas with varying pressures according to the vapor pressure of samples.

In addition to the 532 nm desorption laser, one or two other lasers are required to photoexcite the energetic materials and model systems within the beam and then detect the fragmented pieces (NO in this case). For the ns MRES experiments, a single pump-probe laser is needed from 226-258 nm to both initiate the dissociation of the nitramine molecules and to detect the NO⁺ ions through TOFMS [$A(v'=0) \leftarrow X(v''=0-3)$ and $I \leftarrow A$ transitions]. The proper UV laser wavelengths for this process are generated by a dye laser, pumped by the second harmonic (532 nm) of a Nd:YAG laser's fundamental output (1064 nm), in conjunction with a wavelength extension system. For the fs pump-probe experiments, a single laser beam at 226 nm is equally split into pump and probe beams. The sample molecules are excited by the pump beam and fall apart according to their photodissociation dynamics. Photodissociation products are further ionized by the delayed probe beam and detected via the TOFMS. By delaying the probe beam with respect to the pump beam, product appearance time can be determined. The fs laser light is generated by a femtosecond laser system consisting of a self-mode-locked Ti:Sapphire oscillator (KM Labs), a home-made ring cavity Ti:Sapphire amplifier, and a commercial traveling optical parametric amplifier of super fluorescence (TOPAS, Light Conversion) system. The pulse duration of the UV laser light has been measured to be 180 fs using a

self-diffraction (SD) autocorrelator and the off-resonance two-photon absorption of the furan molecule³⁹.

The experiment is run at a repetition rate of 10 Hz. The timing sequence for the pulsed nozzle and the ablation laser is controlled by a time delay generator (SRS DG535). Ion signals are detected by a microchannel plate detector (MCP). Signals are recorded and processed on a PC using an ADC card (Analog Devices RTI-800) and a box car averager (SRS SR 250). For the fs pump-probe experiments, the delay time between the pump and probe beam is controlled by a micro translation stage (Thorlabs: LNR50SEK1) where a step size of 13 femtoseconds has been used. Each point on the pump-probe transient intensity curve corresponds to an average intensity resulting from 100 laser shots.

Calculation Procedures

Potential energy surface calculations have been performed for RDX, nitropiperidine, nitropyrrolidine and dimethylnitramine using the chemistry computational software package Gaussian 98⁴⁰. The optimization of ground state geometries, as well as ground (S_0) transition state structures have been performed at a MP2/6-31G* level of theory (RHF/6-31G* is used to calculate the unstable normal mode of vibration for RDX). Optimizations of the geometries, energies, and transition state structures for the excited state (S_1), have been computed at a RCIS/6-31+G level of theory. Additionally, a CASSCF (10,6)/STO-3G calculation is employed on DMNA in efforts to determine a conical intersection between the first and second excited state.

Results

Analysis of the four rovibronic transitions, $A^2\Sigma(v'=0)\leftarrow X^2\Pi(v''=0,1,2,3)$, of the NO molecule observed from ns photodissociation of CL-20 excited to its first excited electronic state, by 226-250 nm UV laser light, shows similar results to the NO molecule observed from RDX and HMX (Figure 2). The four spectra in fig. 2 have similar rotational structure but have varying vibrational intensity for each vibronic band. As was shown for HMX and RDX^{23,24} the most intense feature in each spectrum of NO from CL-20 corresponds to the ($Q_{11} + P_{21}$) band while the less intense features within each spectrum correspond to the rotational transitions^{41,42}.

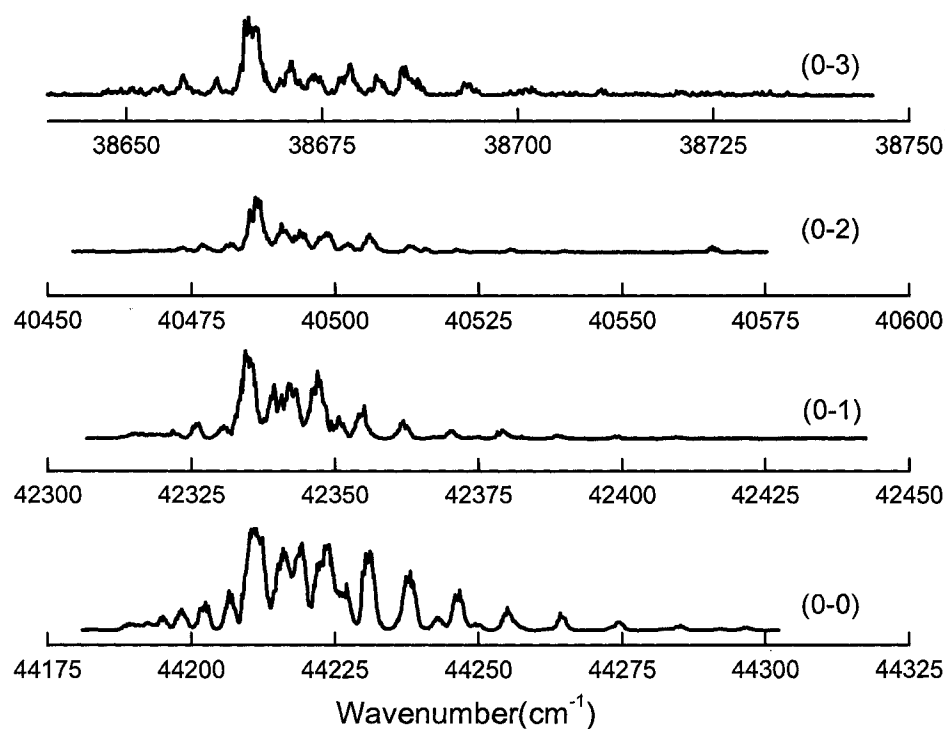


Figure 2. Absorption 1-color MRES of the $A^2\Sigma(v'=0)\leftarrow X^2\Pi(v''=0,1,2,3)$ transitions of NO from CL-20

Although the MALD technique is a good method to place easily fragmented, fragile molecules in the gas phase without fragmentation, great efforts are taken in our previous and present work to ensure that HMX, RDX, or CL-20 are not fragmented in the desorption process²³⁻²⁵. Three different methods have been employed to explore this issue: comparison of NO velocity distributions from the nozzle; determination of arrival time for the NO signal intensity as a function of nozzle/pump laser timing; and NO rotational and vibrational temperature determinations as a function of source of NO. These methods demonstrate that NO from HMX, RDX, and CL-20 is generated at the decomposition/ionization region rather than in the desorption nozzle.

Figure 3 illustrates the $A \leftarrow X$ (0-1) transition spectra with simulations of the initial decomposition product, the NO molecule, of RDX, HMX, and CL-20. Comparisons of the three spectra confirm that the NO molecule from the decomposition of CL-20, HMX, and RDX has very similar rotational temperature (20 K) for the (0-1) vibronic transition. In addition, the observation of similar transition bands demonstrates the NO molecule from the decomposition of CL-20 has about the same vibrational temperature (~ 1800 K) as that for RDX and HMX. Thus we conclude: the NO molecule is an initial product of the electronically excited decomposition of the three energetic materials (RDX, HMX, and CL-20); the NO product is rotationally cold (20 K) and vibrationally hot (~1800 K); and the UV photodecomposition of CL-20 experiences the same decomposition mechanism as that of RDX and HMX.

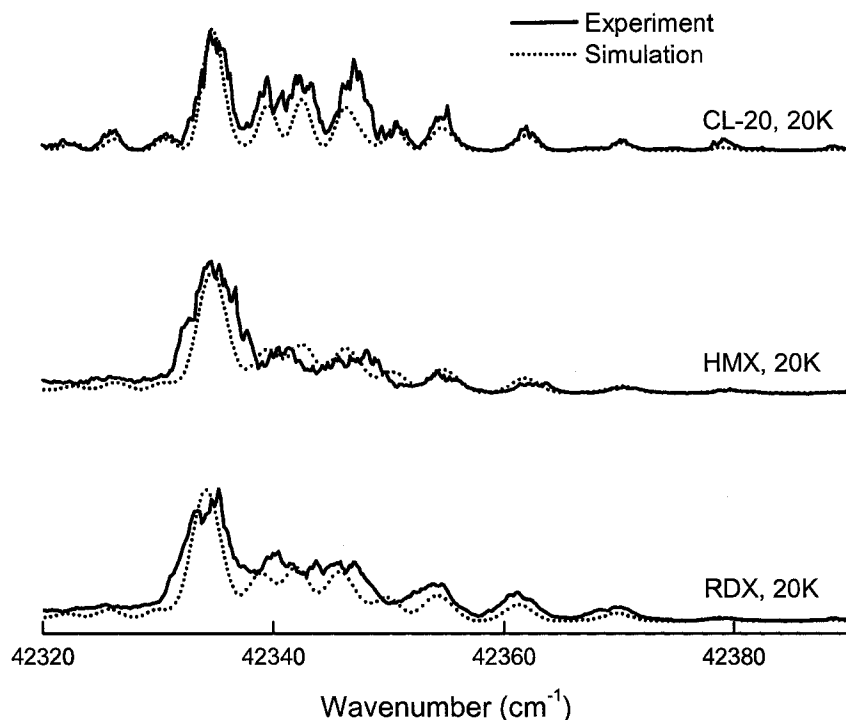


Figure 3. Comparison of the 1-color MRES of the $A^2\Sigma(v'=0)\leftarrow X^2\Pi(v''=1)$ transition of NO from CL-20, HMX, and RDX.

In efforts to better understand the excited state decomposition mechanisms of HMX, RDX, and CL-20 a number of model systems are explored. Although the NO molecule is still the only observed product of the ns UV photodecomposition of all the model systems from their excited electronic states, the rotational and vibrational spectral distributions of the NO molecule are not only different from the energetic materials but also from each other. Figure 4 presents the MRES spectra with simulations of the $A\leftarrow X$ (0-0) transition of the NO decomposition product for these model systems. The rotational temperatures of the NO product from 1,4-dinitropiperazine, nitropiperidine, dimethylnitramine, and nitropyrrolidine are 20 K, 20 K, 120 K, and 50 K, respectively. NO from dimethylnitramine and nitropyrrolidine is rotationally hotter than NO from nitropiperidine and 1,4,-dinitropiperazine suggesting the model systems which are more

similar in structure to RDX, nitropiperidine and dinitropiperazine, could possibly follow similar decomposition routes to those of the energetic materials. Yet the comparisons shown in Figure 5 suggest the model systems behave differently. The A←X (0-1) transitions of the model systems yield much hotter rotational temperatures than those of the energetic materials. Computational results in the following discussion will shed insight into these seemingly inconsistent results. Table 1 gives the rotational temperatures for each of the populated vibrational levels of the NO product from both the energetic materials and model systems. NO from the energetic materials (RDX, HMX, and CL-20) has its first four vibrational levels populated [$X^2\Pi(v''=0,1,2,3)$], whilst NO from the model systems have fewer vibrational states populated indicating a cooler vibrational temperature. NO from dinitropiperazine, nitropiperidine, and nitropyrrolidine have measured vibrational signals for $X^2\Pi(v''=0,1)$, but NO from dimethylnitramine is only observed from its ground vibrational level [$X^2\Pi(v''=0)$]. In brief summary, the overall vibrational temperature of the NO molecule from the model systems is much less than that of the NO molecule from energetic materials.

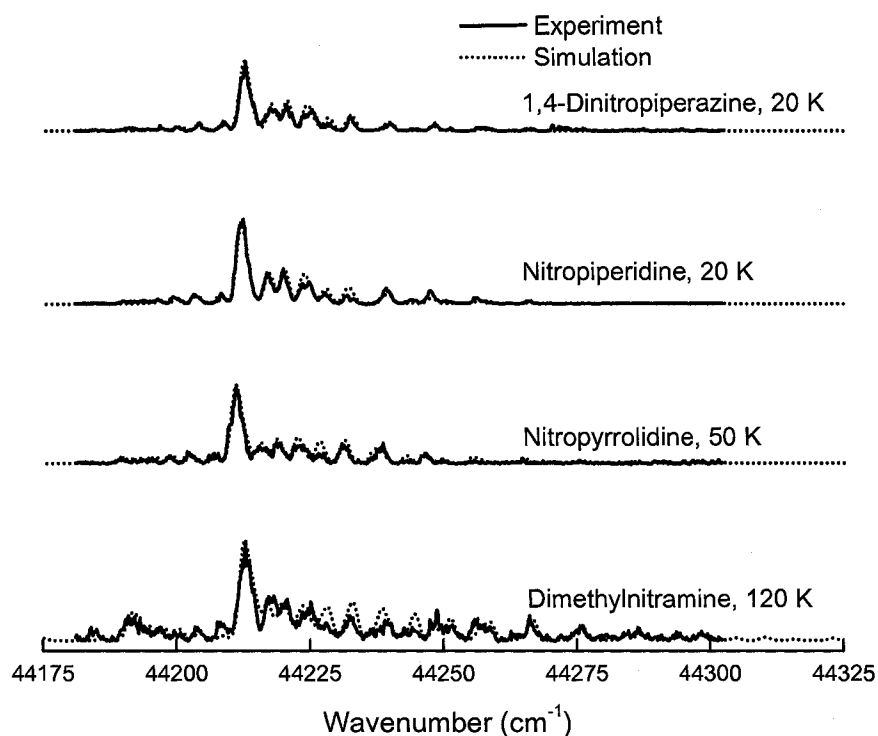


Figure 4. 1-color MRES of the $A^2\Sigma(v'=0) \leftarrow X^2\Pi(v''=0)$ transition of NO from the nitramine model systems.

System	Rotational Temp. ns $A \leftarrow X (0-0)$	Rotational Temp. ns $A \leftarrow X (0-1)$	Rotational Temp. ns $A \leftarrow X (0-2)$	Rotational Temp. ns $A \leftarrow X (0-3)$
CL-20	20 K	20 K	20 K	20 K
HMX	20 K	20 K	20 K	20 K
RDX	20 K	20 K	20 K	20 K
Dinitropiperazine	20 K	75 K	-----	-----
Nitropiperidine	20 K	700 K	-----	-----
Nitropyrrolidine	50 K	100 K	-----	-----
Dimethylnitramine	120 K	-----	-----	-----

Table 1. Rotational temperatures for the $A^2\Sigma(v'=0) \leftarrow X^2\Pi(v''=0,1,2,3)$ transitions of the NO product from ns UV decomposition of Energetic materials and model systems

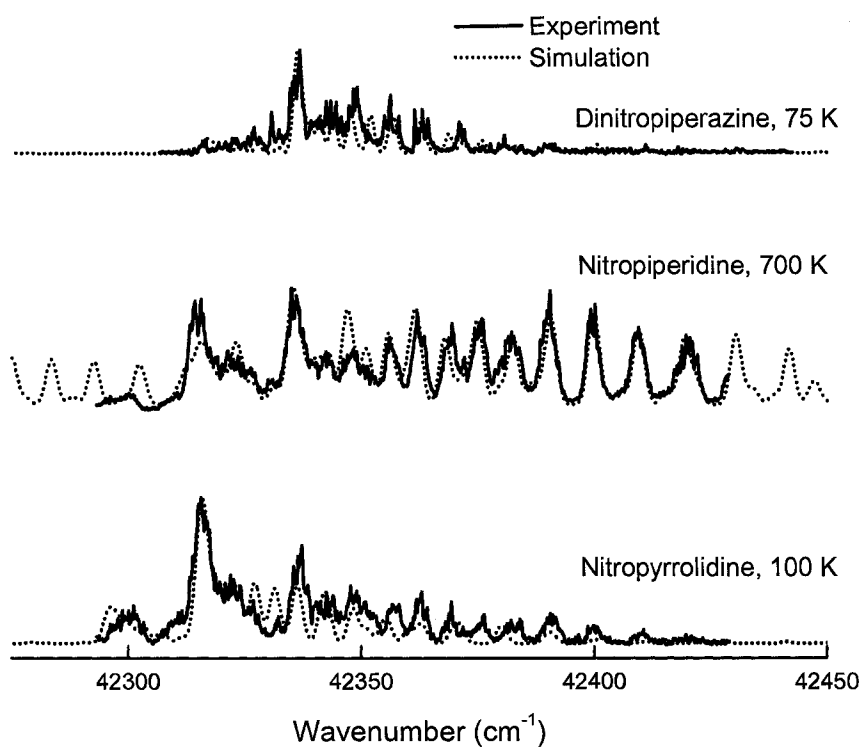


Figure 5. 1-color MRES of the $A^2\Sigma(v'=0) \leftarrow X^2\Pi(v''=1)$ transition of the NO molecule from the Nitramine model systems.

System	(0-1) NO intensity (ns)	fs result
CL-20	3.7 V	NO product decomposes < 180 fs
HMX	2.0 V	NO product decomposes < 180 fs
RDX	1.5 V	NO product decomposes < 180 fs
Dinitropiperazine	300 mV	NO product decomposes < 180 fs
Nitropiperidine	255 mV	NO product decomposes < 180 fs
Nitropyrrolidine	160 mV	Stable ion
Dimethylnitramine	150 mV	Stable ion

Table 2. The fs photodissociation products and ns NO signal intensities for the energetic materials and model systems.

The NO signal intensity for the ns UV decomposition of the energetic materials and model systems, as well as the results for the fs UV decomposition of these materials is listed in Table 2 above. The relative concentration of RDX, HMX, and CL-20 is assumed to be the same in the ionization region due to the fact that equal molar amounts of each material are placed on the sample drum. Comparing the signal intensity of the NO molecule for each energetic material yields an approximate ratio of 3:4:6 for RDX : HMX : CL-20 corresponding to the number of nitramine moieties within each material. This signal intensity, suggests that the energetic materials decompose via the same mechanism in which each nitramine group yields an NO molecule. On the fs time scale, parent ions of DMNA and nitropyrrolidine are observed when 226 nm fs light pulses are employed to photodissociate these nitrate systems (Figure 6). Table 2 illustrates that all of the other systems explored in the fs time regime yield the NO product.

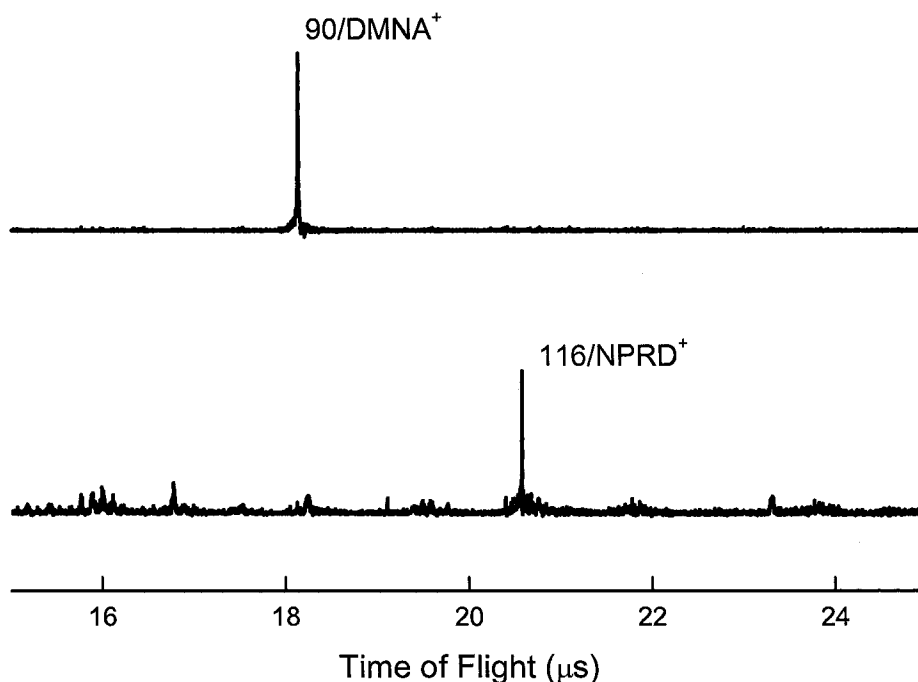


Figure 6. Mass spectra of dimethylnitramine (upper) and nitropyrrolidine (lower) using 226 nm fs excitation.

Figure 7 displays the fs pump-probe transients of the NO product from RDX (b), and CL-20 (c) at 226 nm. The NO molecule has a resonant single photon absorption for the $A^2\Sigma(v'=0) \leftarrow X^2\Pi(v''=0)$ transition at 226 nm. Both pump and probe beams have the same wavelength. As described in our previous paper²⁵ the gas phase energetic material is pumped into its first excited electronic state by the pump beam, it dissociates into products according to its corresponding mechanisms and dynamics, and its initial products are probed. The dynamics of the decomposition are measured via the NO molecule appearance. If the decomposition of the energetic materials is slower than the time duration of the pump and probe beams (180 fs) an (exponential) onset of the NO ion signal will be observed as the relative delay time between the pump and probe is scanned. If the decomposition of the energetic materials is much faster than the pulse duration, the NO product will be excited by the pump beam rather than by the probe beam and the lifetime of the NO excited state, which is several hundreds of ns, will be detected by the probe beam. The transients in fig. 7 show a roughly steady NO ion signal from both RDX and CL-20, which is the same as NO gas, indicating the dynamics of these three systems occur faster than the time duration of our laser pulse. Similar results were found for nitropiperidine and dinitropiperazine suggesting that these larger more representative model systems also have fast dissociation dynamics.

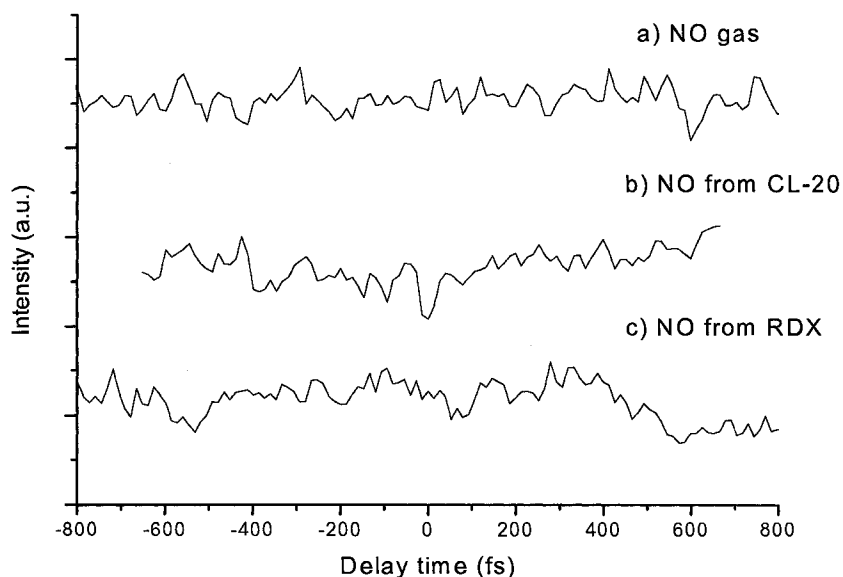


Figure 7. fs pump-probe transients for the NO molecule from NO gas (a), and the photodissociation of RDX (b) and CL-20 (c) at 226 nm. The NO₂ $A^2\Sigma(v'=0) \leftarrow X^2\Pi(v''=0)$ transition has a single-photon resonant absorption at 226 nm. Intensity is in arbitrary units

Discussion

In the results section, we conclude that the NO molecule is an initial ns UV decomposition product for both the energetic materials and model systems of interest in this work. However, there is a difference between the systems, the energetic materials present a rotationally cold and vibrationally hot NO molecule while the model systems give a rotationally hot yet vibrationally cold NO molecule. In order to understand better the experimental data, calculations of geometries, energies, and transition state structures for both the ground (S_0) and excited (S_1) states have been performed on the energetic materials and model systems. Two possible decomposition mechanisms are computationally explored in efforts to yield insight into the experimental finding. The first mechanism includes a dissociative excited state which follows a decomposition channel through an isomerization of the nitramine moieties. The second mechanism involves an internal conversion of the excited state into the ground state in which the decomposition

also follows a path through the isomerization of the nitramine moiety. Since the calculations on the large RDX molecule require a lot of memory, a low level of theory (RHF/ 6-31G*) has been used to optimize the ground state structures of RDX as well as find its transition state geometry. Recent access to a TeraGrid supercomputing facility should allow us to use a higher level of theory (MP2/6-31G*, CIS/6-31+G) for structure and transition state optimization of the RDX molecule in the future. Although the calculations are still in progress, their initial results, shown below, taken with the experimental data, shed some light onto the possible decomposition mechanisms.

Calculations on RDX and the model systems nitropiperidine and nitropyrrolidine indicate that the most probable decomposition mechanism for the energetic materials is internal conversion of the excited molecules to highly excited vibrational states of their ground electronic states, which is followed by isomerization and dissociation. RDX, nitropiperidine, and nitropyrrolidine have calculated first excited electronic state energies of 5.59 eV, 5.62 eV, and 5.85 eV, respectively. Each system is excited to its first excited electronic state by absorbing a single 226 nm (~ 5.5 eV) photon. NO from RDX, HMX, and CL-20 is vibrationally hot yet rotationally cold. Calculations suggest that there is not enough extra energy within the electronically excited energetic materials to produce a highly vibrationally excited NO decomposition molecule. Therefore, the energetic materials must undergo an internal conversion to their ground electronic state. This conversion would give extra energy (5.5 eV) to the molecule allowing for the high vibrationally energy. The low rotational temperatures associated with the different populated vibrational levels of the NO decomposition product indicate that the parent molecule (RDX, HMX, and CL-20) must isomerize and the resulting NO-NO moiety

must become linear. Nitropiperidine and nitropyrrolidine, on the other hand, yield a vibrationally cool but rotationally hot NO molecule. The low vibrational temperature of the NO molecule indicates the parent molecules should decompose from their first excited state. It is possible that there is a small amount of extra energy, above the excited state TS geometry, to excite the low frequency bending modes of the parent molecule (nitropiperidine and nitropyrrolidine). These low frequency modes will result in a NO molecule with populated $\nu''=0$ and $\nu''=1$ states with high rotational energy. The suggested decomposition mechanisms for the energetic materials are therefore different from those of the model systems. Further analysis of the ground and excited state calculations performed on these systems will be presented below.

The ground state (S_0) nitro-nitrite isomerization TS geometries of RDX, nitropiperidine, and nitropyrrolidine are illustrated in Figure 8, Figure 9, and Figure 10, respectively. Each system has an isomerization TS_1 with similar S_0 geometry at an energy of ~ 1 eV. RDX has three additional unique concerted nitro-nitrite isomerization states; one TS at an energy of ~ 1 eV (S_0 - TS_2) and two states (S_0 - TS_3 , S_0 - TS_4) at an energy 1.4 eV above the single nitro-nitrite isomerization state (S_0 - TS_1). The \angle NON TS bond angle, of RDX, nitropiperidine, and nitropyrrolidine, is around 105 - 110° and the negative frequency or unstable normal mode of vibration is characterized by the out-of-plane bending of the ONCC moiety. This motion corresponds to a true nitro-nitrite isomerization. Due to the similar TS structures and the unstable normal modes of vibration a decomposition mechanism through the ground TS of RDX, nitropiperidine, and nitropyrrolidine should yield similar NO molecule rotational and vibrational

temperatures. This is not found to be true experimentally suggesting, again, that the energetic materials decompose through a different path than the model systems.

From the excited state calculations of nitropiperidine and nitropyrrolidine it appears as though the $\nu''=0$ and $\nu''=1$, of the NO decomposition product, are populated from different vibronic states of the transition state, while the rotations are populated from the low frequency bending modes of the excited transition state. An example of this is illustrated below by assuming that the vibrationless ($\nu''=0$) ground state of the NO molecule is populated solely from the $\nu'=0$ state of the transition state (TS) of the parent molecule (nitropiperidine, or nitropyrrolidine) for a particular electronic surface (S_0 , S_1 , $S_2\dots$), while other vibrational levels ($\nu''=1,2,3\dots$) of the NO molecule are being populated from the vibrational excitations of the TS.

Further analysis of the excited state calculation on nitropiperidine suggests the S_1 (TS) negative frequency or unstable normal mode of vibration of nitropiperidine corresponds to a rotation of the terminal NO around the elongated ON bond of the molecule. This unstable mode of vibration of the nitropiperidine molecule, could result in a NO molecule with high rotational population of the $\nu''=1$ state which corresponds with the probed $A\leftarrow X$ (0-1) rotationally hot (700 K) transition of the NO molecule. The S_1 TS geometry corresponds to the NO $\nu''=0$ population. The probed (0-0) rotational temperature of NO from nitropiperidine (20 K) is the same as NO from RDX ($T_{\text{rot}}=20$ K) but the probed NO (0-1) rotational temperatures are very different, suggesting, from the analysis of the S_1 TS unstable normal mode of vibration, nitropiperidine decomposes through the isomerization transition state of its first excited state.

RDX

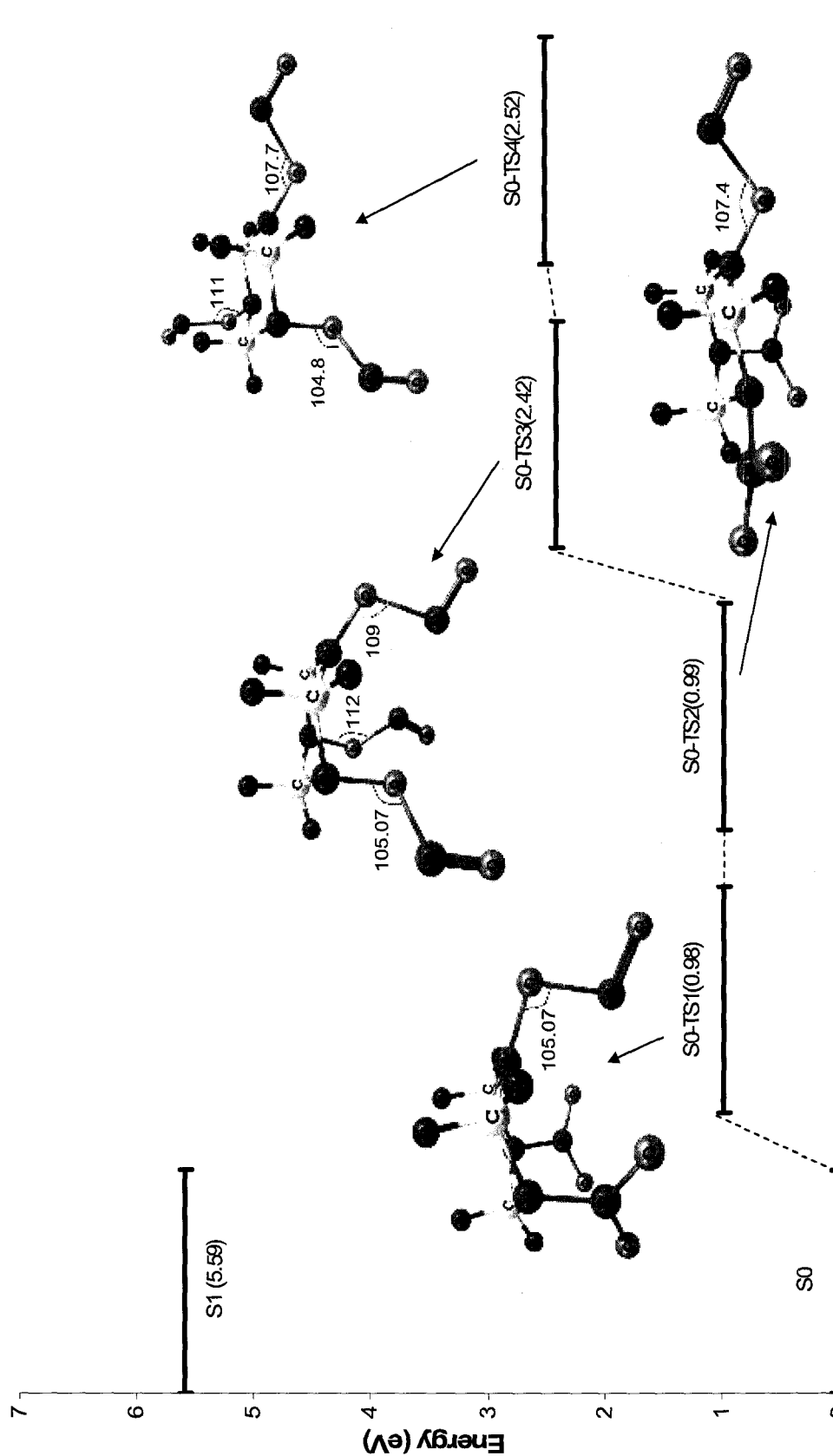


Figure 8. Potential energies and structures of the transition states of RDX in its ground electronic state. Energies are in eV.

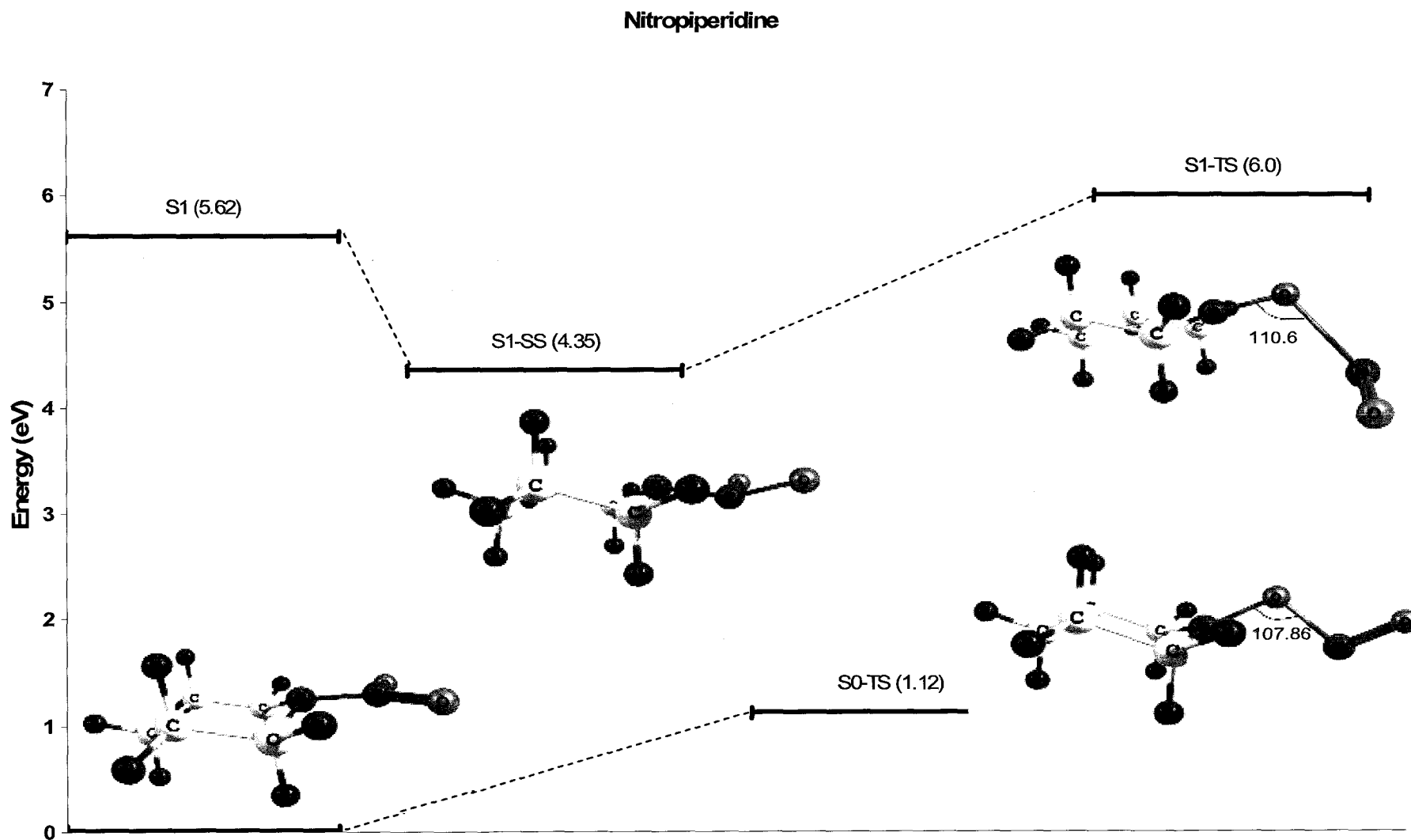


Figure 9. Potential energies and structures of the transition states of Nitropiperidine in its ground and first excited states.

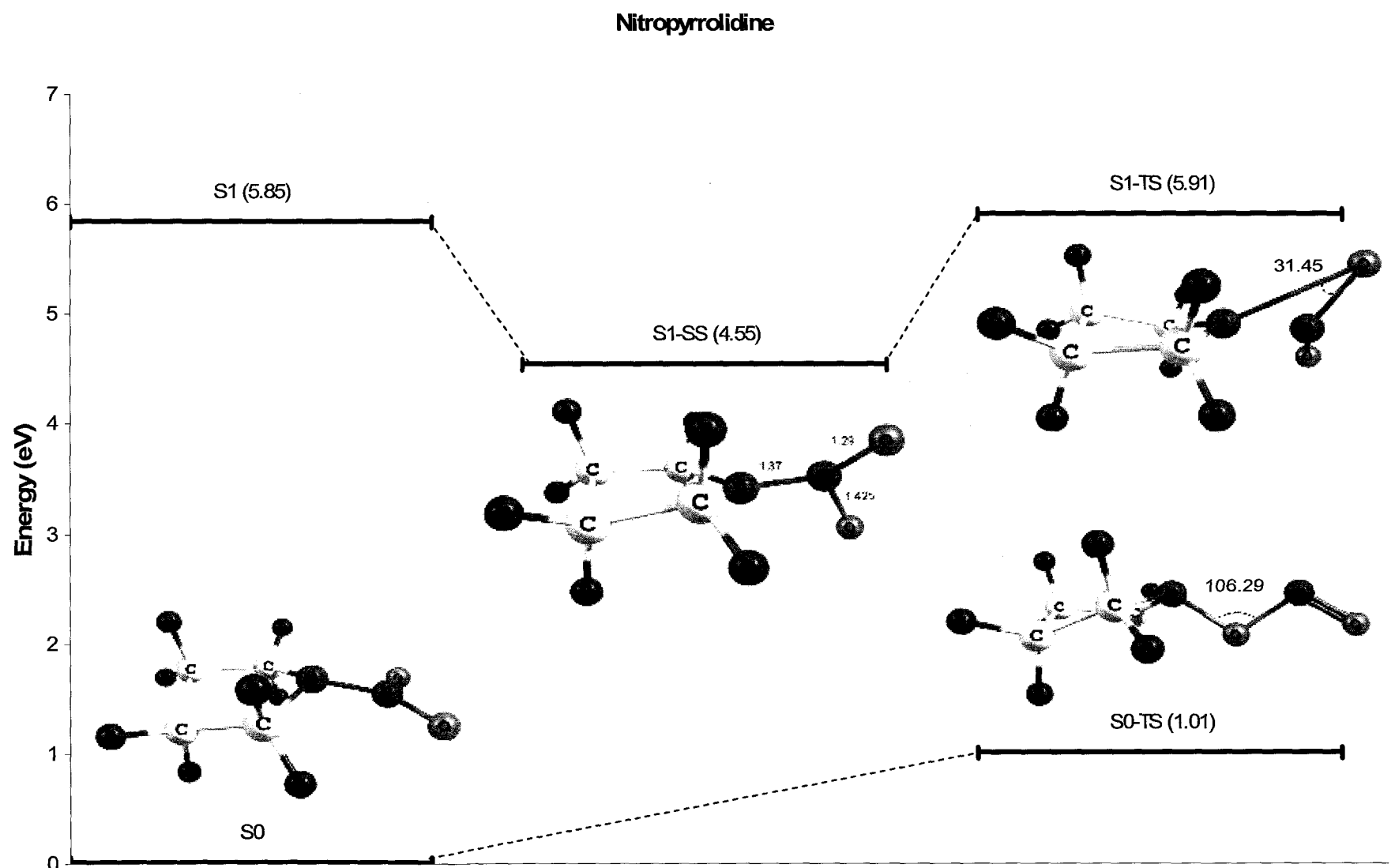


Figure 10. Potential energies and structures of the transition states of Nitropyrrolidine in its ground electronic and first excited states.

The rotational energy of the initial NO decomposition product is associated with the \angle NON bond angle in the nitro-nitrite isomerization TS. A smaller \angle NON bond angle will result in more NO $v''=0$ rotational population. Nitropyrrolidine has a much tighter S_1 , TS \angle NON bond angle than nitropiperidine, see fig 10. Therefore, the bond angle, \angle NON = 32° , for nitropyrrolidine results in a higher NO $v''=0$ rotational population. The probed NO (0-0) rotational temperature is 50 K. The unstable normal mode of vibration associated with the S_1 -TS relates to an asymmetric stretch of the ONO moiety. NO from Nitropyrrolidine has a probed (0-1) rotational temperature of 100 K which reflects this. The unstable normal mode associated with nitropiperidine corresponds directly with the rotation of the NO moiety hence the (0-1) rotational temperature of NO from nitropiperidine (700 K) should be greater than NO from nitropyrrolidine (100 K). The S_1 transition state geometries and frequencies of nitropyrrolidine and nitropiperidine suggest these two molecules decompose through a nitro-nitrite isomerization process occurring in their first excited state (S_1).

The low rotational temperatures and high vibrational temperature of NO from RDX suggests that there is an internal conversion, of the (S_1) excited RDX molecule, to very highly excited (~ 5 eV vibrational energy) vibrational states of the ground electronic state followed by concerted nitro-nitrite isomerization and decomposition. This is favorable from energy considerations and consistent with the experimental results that the NO^+ ion signal intensity is proportional to the number of nitramine functional groups. This mechanism is only suggested and requires true frequency values of the ground TS as

well as a better understanding of the excited state (S_1) namely the TS geometry and stable minima.

The model system DMNA has very different calculational results compared to RDX, nitropiperidine, and nitropyrrolidine. Current CASSCF (10,6) active space calculations predict a NO_2 elimination followed by a direct dissociation decomposition mechanism rather than the isomerization process suggested for the other systems. A 226 nm light pulse excites DMNA to its second excited state S_2 . The CASSCF calculations show an optimized conical intersection between the excited states S_2 and S_1 . A 266 nm light pulse will excite DMNA to its first excited state. Mialocq and Stephenson^{43,44} have shown the NO_2 elimination decomposition pathway from DMNA at a 5 ps time scale using a 266 nm pump and 532 nm probe experiment. NO from DMNA at 226 nm is vibrationally cold, only the (0-0) transition is observed, and rotationally hot (120 K). This compares well to NO from NO_2 gas passed through the supersonic expansion⁴⁵. NO from NO_2 is also rotationally hot for the (0-0) transition. Therefore, it is suggested that DMNA decomposes through its first excited state (S_1) via the NO_2 precursor.

Parent ions of DMNA and nitropyrrolidine are observed from the fs UV decomposition of these two species. All other systems generate NO as a decomposition product and the dynamics of the decomposition of these systems are faster than 180 fs. So far we do not have theoretical calculations to further explain the experimental results in the fs time regime.

Conclusions:

Electronically excited photodissociation of the nitramine energetic materials (RDX, HMX, and CL-20) and models systems (1,4-dinitropiperazine, nitropiperidine,

nitropyrrolidine and dimethylnitramine) has been investigated via both nanosecond MRES and femtosecond pump-probe techniques. The NO molecule is a dominant product of both the energetic materials and model systems. However, the NO molecule from energetic materials displays cold rotational and hot vibrational spectral structures. In contrast, the NO molecule from the model systems shows relatively hot rotational and cold vibrational states. Parent ions of dimethylnitramine and nitropyrrolidine are observed in femtosecond experiments. All of the other systems generate the NO molecule as a product even in the femtosecond temporal regime, and the dynamics of the decomposition falls into 180 fs scale, which is equivalent to the time duration of our laser pulse. Finally, calculations suggest the energetic materials decompose via an isomerization of the nitramine moieties that occur after an internal conversion to very highly excited (~ 5 eV of vibrational energy) vibrational states of the ground electronic state. The model systems nitropiperidine and nitropyrrolidine most likely decompose via an isomerization route of the dissociative S_1 excited state, while DMNA decomposes through an excited electronic state geometry with the NO_2 precursor for the observed NO molecule.

References

- (1) Owens, F. J.; Sharma, J. *J. Appl. Phys.* **1980**, *51*, 1494.
- (2) Bulusu, S.; Weinstein, D. I.; Autera, J. R.; Velicky, R. W. *J. Phys. Chem.* **1986**, *90*, 4121.
- (3) Dick, J. J.; Mulford, R. N.; Spencer, W. J.; Pettit, D. R.; Garcia, E.; Shaw, D. C. *J. Appl. Phys.* **1991**, *70*, 3572.
- (4) Oxley, J. C.; Kooh, A. B.; Szekeres, R.; Zheng, W. *Journal of Physical Chemistry* **1994**, *98*, 7004-7008.
- (5) Fickett, W.; Davis, W. C. *Detonation*; University of California Press: Berkeley, 1979.
- (6) Ree, F. H. *J. Chem. Phys.* **1984**, *81*, 1251.
- (7) Kohno, Y.; Ueda, K.; Imamura, A. *J. Phys. Chem.* **1996**, *100*, 4701.
- (8) Sorescu, D. C.; Rice, B. M.; Thompson, D. L. *J. Phys. Chem. B* **1998**, *102*, 6692.
- (9) Capellos, C.; Lee, S.; Bulusu, S.; Gams, L. *Advances in Chemical Reaction Dynamics*; Reidel: Dordrecht, 1986.
- (10) Zuckermann, H.; Greenblatt, G. D.; Hass, Y. *J. Phys. Chem.* **1987**, *91*, 5159.
- (11) Capellos, C.; Papagiannakopoulos, P.; Liang, Y.-L. *Chemical Physics Letters* **1989**, *164*, 533.
- (12) Zhao, X. S.; Hints, E. J.; Lee, Y. T. *Journal of Chemical Physics* **1988**, *88*, 801-810.
- (13) Windawi, H. M.; Varma, S. P.; Cooper, C. B.; Williams, F. *Journal of Applied Physics* **1976**, *47*, 3418.
- (14) Schanda, J.; Baron, B.; Williams, F. *Acta Technica Academiae Scientiarum Hungaricae* **1975**, *80*, 185.
- (15) Schanda, J.; Baron, B.; Williams, F. *Journal of Luminescence* **1974**, *9*, 338.
- (16) Varma, S. P.; Williams, F. *Journal of Chemical Physics* **1973**, *59*, 912.
- (17) Hall, R. B.; Williams, F. *Journal of Chemical Physics* **1973**, *58*, 1036.
- (18) Williams, F. *Advanced Chemical Physics* **1971**, *21*, 289.
- (19) Dremin, A. N.; Klimenko, V. Y.; Davidou, O. N.; Zolodeva, T. A. Proc. 9th Symp. on Detonation, Portland OR, 1989; p 319.
- (20) Sharma, J.; Beard, B. C.; Chaykovsky, M. *Journal of Physical Chemistry* **1991**, *95*, 1209.
- (21) Sharma, J.; Forbes, J. W.; Coffey, C. S.; Liddiard, T. P. *Journal of Physical Chemistry* **1987**, *91*, 5139.
- (22) Sharma, J. APS Topical Meeting on Shocks in Energetic Materials, Williamsburg VA, 1991.
- (23) Im, H. S.; Bernstein, E. R. *Journal of Chemical Physics* **2000**, *113*, 7911-7918.
- (24) Guo, Y. Q.; Greenfield, M.; Bernstein, E. R. *Journal of Chemical Physics* **2005**, *122*, 6.
- (25) Greenfield, M.; Guo, Y. Q.; Bernstein, E. R. *Chemical Physics Letters* **2006**, *430*.
- (26) Rice, B. M.; Hare, J. *J. Thermochim. Acta* **2002**, *384*, 377.
- (27) Zhou, G.; Wang, J.; He, W.-D.; Wong, N.-B.; Tian, A.; Li, W.-K. *J. Mol. Struct. (Theochem)* **2002**, *273*, 589-590.

- (28) Nielsen, A. T.; Chafin, A. P.; Christian, S. L.; Moore, D. W.; Nadler, M. P.; Nissan, R. A.; Vanderah, D. J.; Gilardi, R. D.; George, C. F.; Flippen-Anderson, J. L. *Tetrahedron* **1998**, *54*, 11793.
- (29) Cabalo, J.; Sausa, R. *Applied Optics* **2005**, *44*, 1084.
- (30) Okovytyy, S.; Kholod, Y.; Qasim, M.; Fredrickson, H.; Leszczynski, J. *Journal of Physical Chemistry A* **2005**, *109*, 2964-2970.
- (31) Foltin, M.; Stueber, G. J.; Bernstein, E. R. *J. Chem. Phys* **1999**, *111*, 9577.
- (32) Foltin, M.; Stueber, G. J.; Bernstein, E. R. *J. Chem. Phys* **2001**, *114*, 8971.
- (33) Wirtz, G. P.; Brown, S.; Kriven, W. M. *Mater. Manuf. Processes* **1991**, *6*, 87.
- (34) Kurze, P.; Krysmann, W.; Schreckenbach, J.; Schwarz, T.; Rabending, K. *Cryst. Res. Technol.* **1987**, *22*, 53.
- (35) Krysmann, W.; Kurze, P.; Dittrich, K.-H.; Schneider, H. G. *Cryst. Res. Technol.* **1984**, *19*, 973.
- (36) Dittrich, K.-H.; Krysmann, W.; Kurze, P.; Schneider, H. G. *Cryst. Res. Technol.* **1984**, *19*, 93.
- (37) Carcabal, P.; Kroemer, R. T.; Snoek, L. C.; Simons, J. P.; Bakker, J. M.; Compagnon, I.; Meijer, G.; Helden, G. v. *Phys. Chem. Chem. Phys.* **2004**, *6*, 4546.
- (38) Snoek, L. C.; Mourik, T. V.; Simons, J. P. *Mol. Phys.* **2003**, *101*, 1239.
- (39) Trebino, R. *Frequency-Resolved Optical Gating: The Measurement of Ultrafast Laser Pulses*; Kluwer Academic Publisher: Boston, 2000.
- (40) Frisch, M. J.; Trucks, G. W.; Schlegel, H. B.; Scuseria, G. E.; Robb, M. A.; Cheeseman, J. R.; Zakrzewski, V. G.; Montgomery, J., J. A.; Stratmann, R. E.; Burant, J. C.; Dapprich, S.; Millam, J. M.; Daniels, A. D.; Kudin, K. N.; Strain, M. C.; Farkas, O.; Tomasi, J.; Barone, V.; Cossi, M.; Cammi, R.; Mennucci, B.; Pomelli, C.; Adamo, C.; Clifford, S.; Ochterski, J. W.; Petersson, G. A.; Ayala, P. Y.; Cui, Q.; Morokuma, K.; Salvador, P.; Dannenberg, J. J.; Malick, D. K.; Rabuck, A. D.; Raghavachari, K.; Foresman, J. B.; Cioslowski, J.; Ortiz, J. V.; Baboul, A. G.; Stefanov, B. B.; Liu, G.; Liashenko, A.; Piskorz, P.; Komaromi, I.; Gomperts, R.; Martin, R. L.; Fox, D. J.; Keith, T.; Al-Laham, M. A.; Peng, C. Y.; Nanayakkara, A.; Challacombe, M.; Gill, P. M. W.; Johnson, B.; Chen, W.; Wong, M. W.; Andres, J.; Gonzalez, C.; Head-Gordon, M.; Replogle, E. S.; Pople, J. A.; Gaussian, Inc.: Pittsburgh PA, 2001.
- (41) Hippler, M.; Pfab, J. *Chemical Physics Letters* **1995**, *243*, 500.
- (42) Herzberg, G. *Spectra of Diatomic Molecules*; Van Nostrand: New York, 1950.
- (43) Mialocq, J. C.; Stephenson, J. C. *Chemical Physics Letters* **1986**, *123*, 390-393.
- (44) Mialocq, J. C.; Stephenson, J. C. *Chem. Phys.* **1986**, *106*, 281-291.
- (45) Im, H. S.; Bernstein, E. R. *Journal of Physical Chemistry A* **2002**, *106*, 7565-7572.

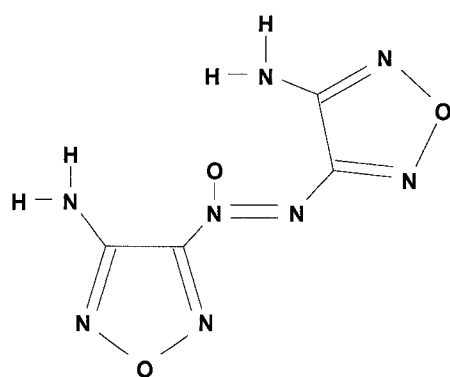
Chapter 5 : Future Direction

Current UV photodissociation experiments on the energetic materials RDX, HMX, and CL-20 suggest the most probable excited electronic state decomposition mechanism is due to an internal conversion of the excited molecules to very highly excited vibrational states of their ground electronic state. If this is indeed true, production of better cyclic nitramine materials would require a S_1 - S_0 conical intersection, an improved S_1 - S_0 Franck-Condon overlap for internal conversion near the S_1 zero point level and an enhanced S_0 density of vibronic states at high S_0 vibrational energy. Compounds that are more likely to have these characteristics are flexible cyclic nitramines with increased internal degrees of freedom.

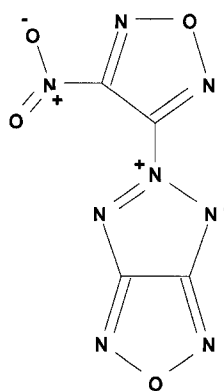
CL-20 is thought of as a bridging system to more compact and crowded multi-ring systems and as an entrée into the high nitrogen content species shown in Figure 1 and Figure 2. Studies presented in this thesis show that electronically excited gas phase CL-20 behaves similarly to electronically excited gas phase RDX and HMX. The suggested decomposition mechanism of CL-20 is internal conversion to very highly excited vibrational states of its electronic ground state. Due to its caged structure CL-20 is probably not as flexible as the longer chained high nitrogen containing species BTATZ or NOTO. If internal conversion plays an important role in the behavior of an energetic material and it is dependent upon the flexibility of the structure, BTATZ and NOTO should give products with high vibrational temperatures. Studying the UV excited state decomposition of these energetic materials by utilizing ns spectroscopy to determine their

decomposition products (NH_2 , NH , NO , CH , N_2O) and the rotational and vibrational temperatures associated with them will give information as to how they decompose as a function of vibrational and electronic state. Time resolved fs spectroscopy experiments on BTATZ or NOTO might determine the mechanism and dynamics for the initial stages of their decomposition as a function of their electronic and vibrational states.

Furazan Based Energetic Materials

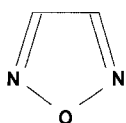


DAAF, diaminoazofurazan

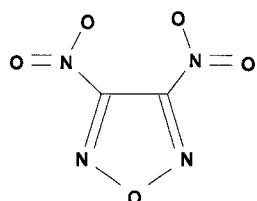


NOTO, 5-[4-nitro-(1,2,5)oxadiazolyl]-5H-[1,2,3]triazolo[4,5-c][1,2,5]oxadiazole

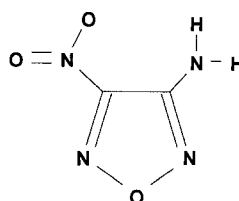
Model systems of Furazan Based Energetic Materials



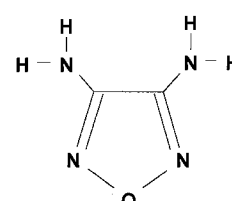
Furazan



3,4-dinitrofurazan



3-amino-4-nitrofurazan



3,4-diaminofurazan

Figure 1. Furazan based energetic materials and model systems.

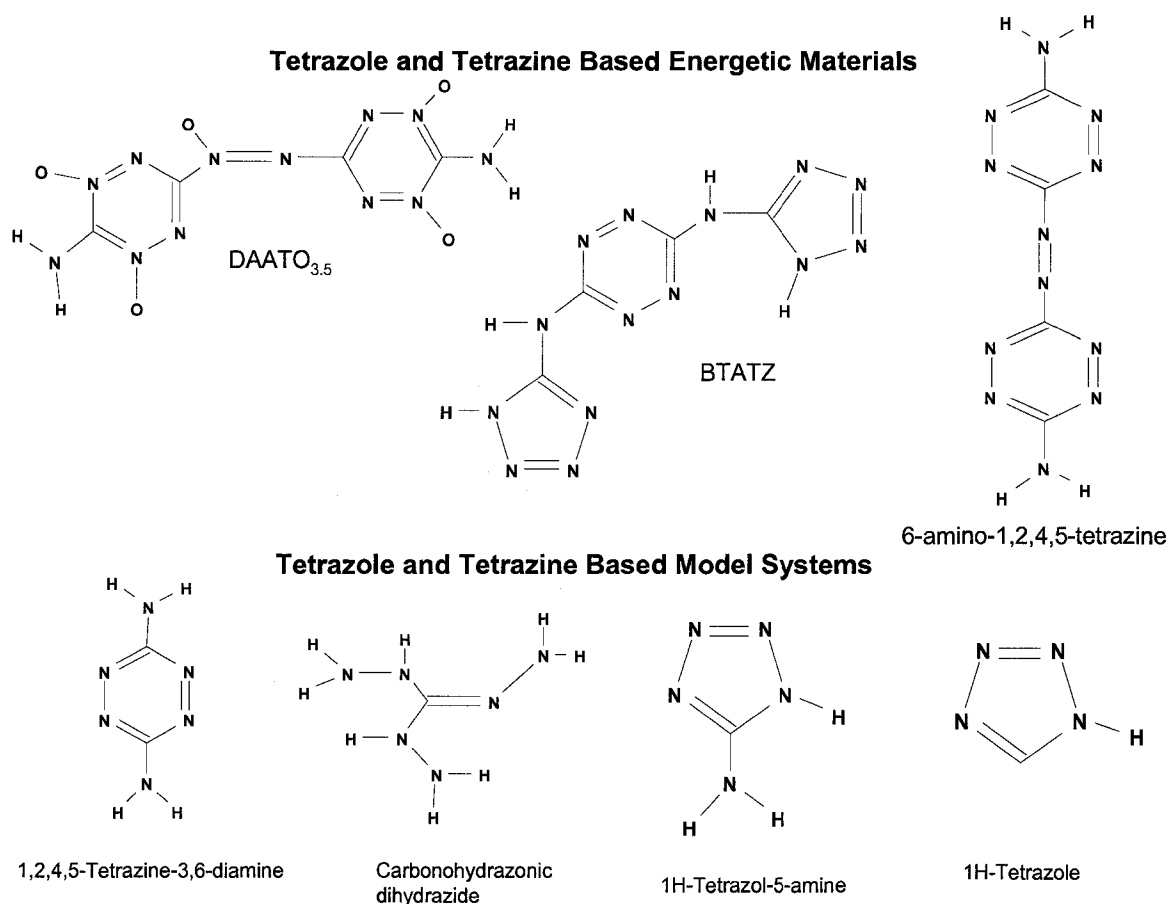


Figure 2. Tetrazole and tetrazine based energetic materials and model systems.

Initial UV excited state decomposition studies on the furazan based high nitrogen energetic material DAAF show the initial decomposition product, the NO molecule, is not as vibrationally hot as NO from RDX and HMX. This suggests that, although DAAF is larger in structure than HMX and RDX and would seemingly give decomposition products with an enhanced S_0 density of vibronic states at high S_0 vibrational energy, the rigidity of the N=N double bond between the furazan like moieties possibly reduced its flexibility and internal degrees of freedom thereby decreasing the internal conversion of the excited state molecules to the highly excited vibrational states of the ground electronic state. Further investigations into the importance of structural make-up

(material, orientation, bonding type, flexibility, etc) of the energetic materials will allow for better understanding of its efficiency and will help in exploring possibilities for new energetic materials.

There are many non-energetic furazan, tetrazole and tetrazine based systems that can be investigated as model systems. The model systems are appealing on many levels. First, the systems are smaller so analyzing the experimental results might be easier. Second, elucidating the true nature as to why some compounds are “energetic” while similar ones are not must arise through a comparison of the decomposition mechanisms and dynamics of the model systems to the energetic materials.

Finally, including calculational and experimental efforts for these new systems will allow for better understanding of the excited state decomposition mechanisms. Calculations will suggest new species and pathways to explore for the experiments while the experiments will provide direction for the calculations, so that a complete picture of the decomposition mechanism will be established.

Appendix 1: Experimental techniques

Introduction

The purpose of this section is to illustrate and discuss in detail the experimental techniques used in the exploration of the excited state decomposition of the nitramine energetic materials and their model systems. A short section on the preparation of these gas phase molecules will be followed by a more in depth discussion on the supersonic expansion used to cool the gas phase molecules translationally, rotationally, and vibrationally. The cooled molecules allow for proper completion of the spectroscopy experiments. The final sections of this appendix will delve into the three spectroscopy experiments performed; namely the TOFMS, LIF, and fs pump-probe experiments. A general overview of the experiments, including an experimental schematic, will be provided. This appendix is intended to document, in detail, how the experiments were performed and to give a basic background/ overview to a new student working on this or a similar project.

Gas Phase Molecules

The excited electronic state decomposition experiments require intact neutral gas phase sample molecules. The energetic materials HMX and RDX are large, fragile and extremely reactive species. Placing these species into the gas phase as intact molecules involves a variant to the well know matrix assisted laser desorption ionization (MALDI) technique which generates ions that are further detected by a mass spectrometer

(Figure 1). The MALD (matrix assisted laser desorption) technique, developed in the Bernstein laboratory, places large, fragile, intact neutral molecules (peptides, dyes, energetic materials, etc) into the gas phase for spectroscopic investigation¹. This process places the species of interest into the vapor phase without decomposition or ionization.

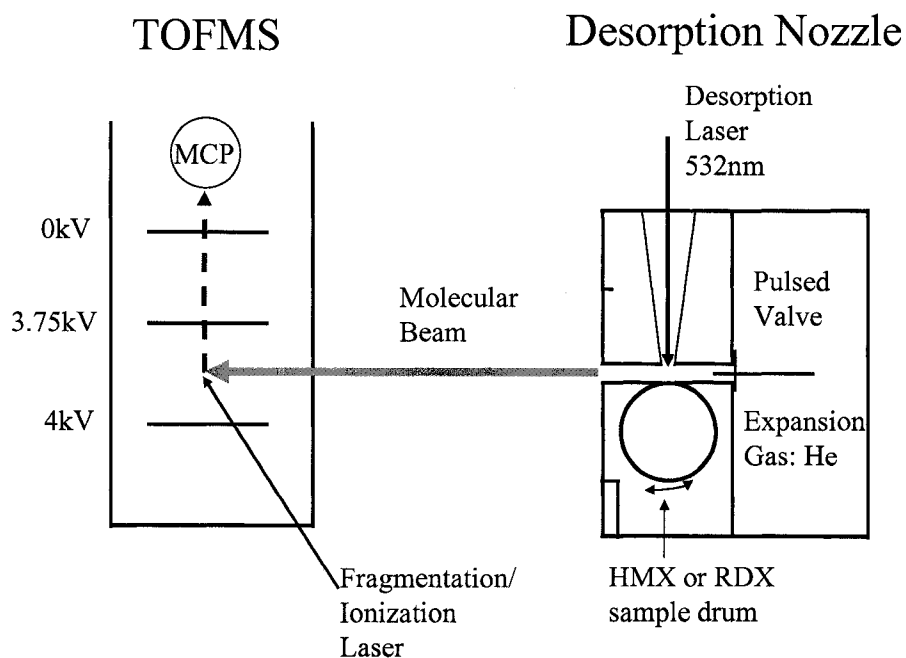


Figure 1. Experimental Setup

A complete discussion on this technique can be found in the appendix 3 of this thesis, sample preparation.

Supersonic expansion

Once the species of significance are in the gas phase a carrier gas, helium or argon, from the pulsed desorption nozzle encompasses them and leads them through a supersonic expansion. The main purpose of the supersonic expansion is to cool the molecules translationally, rotationally, and vibrationally². A molecular gas at room

temperature or higher can contain many populated rotational and vibrational levels, thereby leading to transitions out of many different energy levels. For low spectral resolution, a broadening of bands will occur due to unresolved rotational and possibly unresolved vibrational congestion. Conversely, for high spectral resolution the excessive number of transitions can give a high density of individual rovibronic lines within the spectrum making assignment difficult. Therefore, it is desirable to cool the molecules so that a simpler spectrum can be obtained whereby spectral assignments will be possible.

Supersonic jet expansion dramatically cools the internal degrees of freedom of the molecules without excessive condensation of the gas. A supersonic expansion can be understood by considering the scenario of a gas reservoir (desorption nozzle) located inside a vacuum chamber. In general the gas reservoir has a small hole of diameter D which connects it to the vacuum chamber (Figure 2). If the reservoir is filled with an inert gas (He/Ar) and the vacuum chamber is evacuated via a high speed pump, capable of maintaining a low pressure regardless of the amount of gas escaping into the chamber, a supersonic jet will be formed.

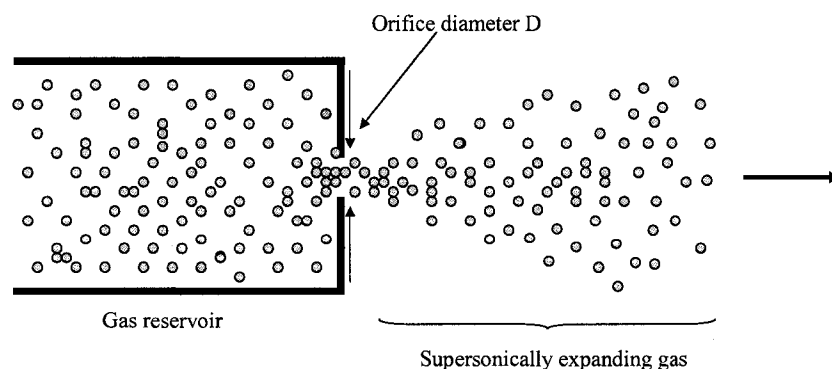


Figure 2. Generic representation of a supersonic expansion

The pressure in the gas reservoir is critical. If it is too low atoms will unlikely collide with each other as they pass into the expansion jet. This collision limit is determined by the mean free path (λ) of the gas, namely the average distance a gas particle must travel between collisions. In the limit that $\lambda \gg D$ (orifice diameter) collisions are unlikely (effusive flow); conversely, if $\lambda \ll D$, corresponding to high pressure in the reservoir, atoms will undergo many collisions as they pass through the orifice. The regime of a supersonic jet is defined by $\lambda \ll D$. Collision will order the departing velocities of the atoms into a narrow range because slower atoms will be accelerated by collisions with more energetic partners moving in the same direction, and rapidly moving atoms will be decelerated by collisions with slower atoms. Compared to their relative speeds in the reservoir, the atoms will appear virtually stationary as they pass through the expansion region into the vacuum chamber. Therefore, as described by the Maxwell-Boltzmann distribution of speeds, the translational temperature will be low because the thermal energy of the reservoir has been converted into directed gas flow with near uniform gas atom speeds³.

A molecule passing through the orifice into the jet expansion will undergo on the order of 10^8 - 10^9 collisions before the translational temperature becomes too low and the divergence of the jet becomes too great. Before this point energy can be transferred from the internal degrees of freedom to the cold translational bath through collisions. The molecule endures an adiabatic $dq = 0$ reversible expansion, and does work to cool it as it enters the expansion. In this isentropic system $\Delta U = \Delta W$, where the work must be done by the gas in the expansion. Specifically in our experiments the RDX, HMX, CL-20, and model system molecules are seeded into the He/Ar carrier gas. As the gas goes through

the supersonic expansion the molecules of interest undergo collisions with the inert He gas. Understanding the cooling in the expansion process requires one to assume the expansion is sliced into infinitely thin pieces with their area perpendicular to the gas flow. At each slice the molecule comes to an equilibrium temperature through collisions perpendicular to the flow.

It is worthy of noting that the efficiency of cooling the rotational and vibrational degrees of freedom is different. Rotational cooling is far more efficient than vibrational cooling because the difference in energy between the different rotational quantum states is less than that of the vibrational energy quantum states. The more energy that has to be transferred the lower the success.

Our experiment uses a pulsed supersonic jet. Due to the very low pressure necessary, within the vacuum chamber, to support an ideal supersonic jet the concept of a pulsed nozzle was created. Continuous supersonic jets have a high gas throughput and therefore require very large vacuum pumps and chambers to support the necessary vacuum for the expansion. By introducing gas into the chamber in short bursts, since the detection and experiment are pulsed, the total gas throughput can be reduced. Pulsed supersonic jets reduce not only the consumption of the carrier gas and sample but also the necessity of large expensive vacuum pumps. The pulsed nozzle used in our experiments runs at 10 Hz and is externally triggered so that it is synchronized with the desorption laser, used in the MALD technique, as well as the fragmentation/ionization or emission laser used for the spectroscopy experiments. The molecules entrained in the helium carrier supersonic expansion gas from our pulsed nozzle cool to a calculated $T_{\text{translational}} = 1 \text{ K}$, $T_{\text{rotational}} = 10 \text{ K}$, $T_{\text{vibrational}} = 50 \text{ K}$. After expansion the cool intact

molecules pass through a skimmer (selecting only the coldest molecules in the molecular beam) and into the spectroscopy region.

Spectroscopy measurements

TOFMS, LIF, and pump-probe spectroscopy experiments were performed in efforts to elucidate the possible decomposition mechanisms as well as the dynamic parameters associated with the decomposition of the energetic materials (HMX, RDX, and CL-20) and their corresponding model systems. The following paragraphs will describe the concepts behind these spectroscopy techniques as well as the more general experimental techniques (alignment, timing, etc.). The nanosecond studies will be addressed first followed by the time resolved pump-probe studies.

Time of flight mass spectroscopy

A packet of ions of differing mass/charge (m/z) ratios, but equal energy or momentum, when projected into a constant electric field will be separated according to their mass to charge ratios. This concept defines how the TOFMS works. If a charge is placed within an electric field gradient it will feel a certain acceleration voltage. If the accelerated ion travels a fixed distance D to a detector, the mass of the ion can be determined from its flight time and the known acceleration voltage. Specifically, for our experiment a neutral molecule passes into the TOFMS region, it is then fragmented and ionized using resonant enhanced multi-photon ionization (REMPI) or non-resonant ionization. The positive ion produced from the fragmentation/ionization laser in the ionization region, is accelerated by +4000 V volts toward a microchannel plate (MCP) detector. For an accelerating electric field E_s , the following velocity equation can be found:

$$v = \left(\frac{2szeE_s}{m} \right)^{\frac{1}{2}} \quad (1)$$

where $ze=q$ is the total charge, E_s is the accelerating electric field applied, v is the velocity, and m is the mass of the ion. Knowing $v = \text{distance}/\text{time}$ the time of flight of the ions is

$$t_{\text{tof}} = \left(\frac{m}{2szeE_s} \right)^{\frac{1}{2}} D. \quad (2)$$

To ensure the proper time of flight and corresponding ion mass are being calculated a TOF mass calibration is performed using the flight times of at least two known masses⁴. This allows for determination of the calibration constants a and b in eq. 4 below.

$$\frac{m}{z} = at^2 + b \quad (3)$$

For our system eq. 4 gives $t = -1.3875 + 1.897\sqrt{m}$ where the time is in micro-seconds (Figure 3).

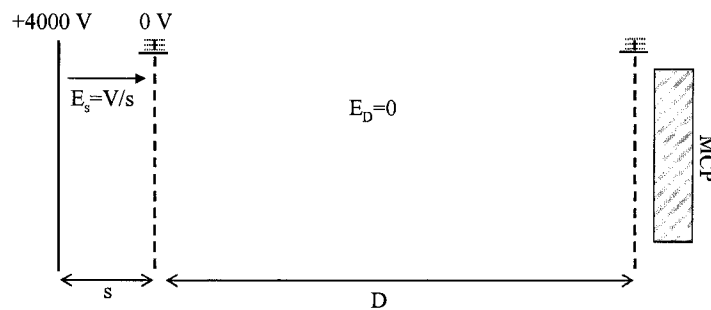


Figure 3. General time of flight setup.

REMPI

Our nanosecond TOFMS experiments utilize the resonance-enhanced multiphoton ionization (REMPI) of the initial decomposition product, the NO molecule. The energetic materials in this study have a decent UV absorption in range of 210 nm to 250 nm (see figure 3 in Chapter 1). Different ro-vibrational resonances for the NO molecule also fall within this wavelength range thereby making this initial product a good decomposition species to study. The energetic material (or model system) absorbs a photon(s) exciting it into a dissociative excited state. The molecule falls apart into different decomposition products, one being the NO molecule. The NO molecule goes through a two stage REMPI process in which the first step the molecules are promoted to an excited electronic state ($A^2\Sigma^+$ for the NO molecule) by the absorption of one (or more) photon(s). REMPI processes are usually regarded as single-photon resonant processes but it is not impossible to use two or more photons of lower energy to achieve the same task. Two qualifications must occur for the multi-photon resonant process to occur: 1) the combined energy must satisfy the resonance condition; and 2) all selection rules for the molecule must be upheld. For the multi-photon transitions to occur high intensity light must arrive at the molecule at the same instant in time. Once in the excited state the molecule can absorb one or more photons putting it above the ionization limit (Figure 4).

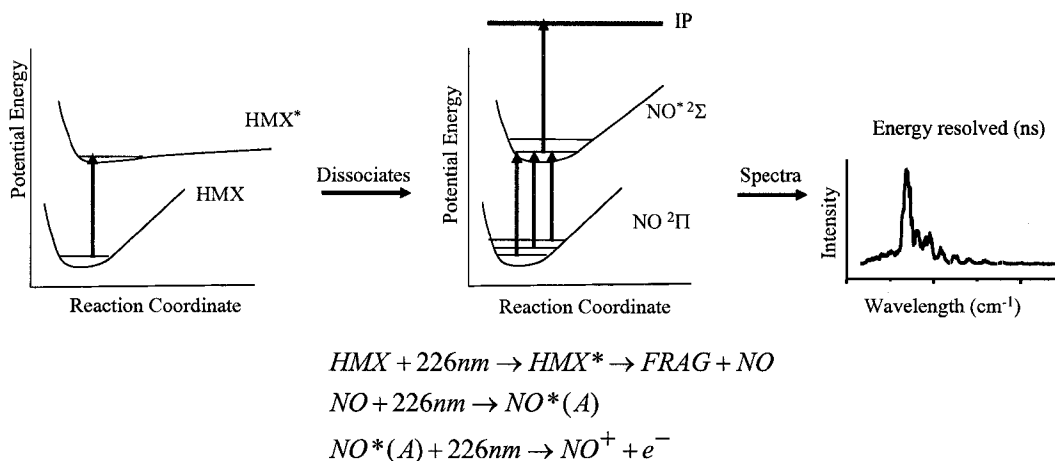


Figure 4. Excited state measurements: TOFMS setup for MRES spectra.

Comparisons of REMPI and direct (non-resonant) multi-photon ionization show that each process requires the same total number of photons absorbed but in REMPI the ionization probability is increased by breaking the ionization process into two sequential steps.

The technique of REMPI can be combined with TOFMS to obtain a MRES (mass resolved excitation spectra) spectrum for an ion of specific mass. In detecting the electronic transitions, of say the NO molecule, when the laser is tuned to a wavelength that is not resonant with a energy level in the excited state manifold of the neutral molecule then ionization is only possible via the non-resonant route and has a low probability. When the wavelength, energy, is scanned and becomes resonant with an intermediate rovibronic level, the ionization probability increases. This is observed by the increased detected ions. The MRES data correspond to the resonant populated rovibronic levels of the molecule in question. Figure 4 above exhibits the detection scheme used for the NO molecule.

In our TOFMS MRES experiments timing is critical. The nanosecond double and mixed dye laser output necessary to obtain the 226 nm light must arrive at the ionization region at the same time as the pulsed cooled molecular beam. These experiments require two lasers, the desorption laser and the fragmentation/ionization laser. The desorption laser, the pulsed nozzle opening, and the fragmentation/ionization laser timing are controlled by two Stanford Research Systems (SRS) delay generators. The delay generators output properly timed trigger pulses to the two lasers and the pulsed nozzle so that a cool molecular beam, containing the species of interest, arrives at the ionization region at exactly the same time as the fragmentation/ionization laser (See figure 7 below for a schematic.). The fragmentation/ionization laser forms the neutral decomposition products, REMPI ionization takes place, and specific mass ions are detected by MCP plate. Scanning the ionization laser wavelength results in an MRES spectrum that corresponds to the resonant rovibronic level transitions for the decomposition product. For the energetic materials and model systems in question the ($v'=0 \leftarrow v''=0,1,2,3$) transitions of the NO molecule were scanned.

Laser Induced Fluorescence (LIF)

In laser induced fluorescence (LIF) an electronic transition of the molecule is excited using a tunable nanosecond (0.2 cm^{-1} resolution) laser and any fluorescence generated is monitored. The general experimental setup is quite simple and illustrated in Figure 5.

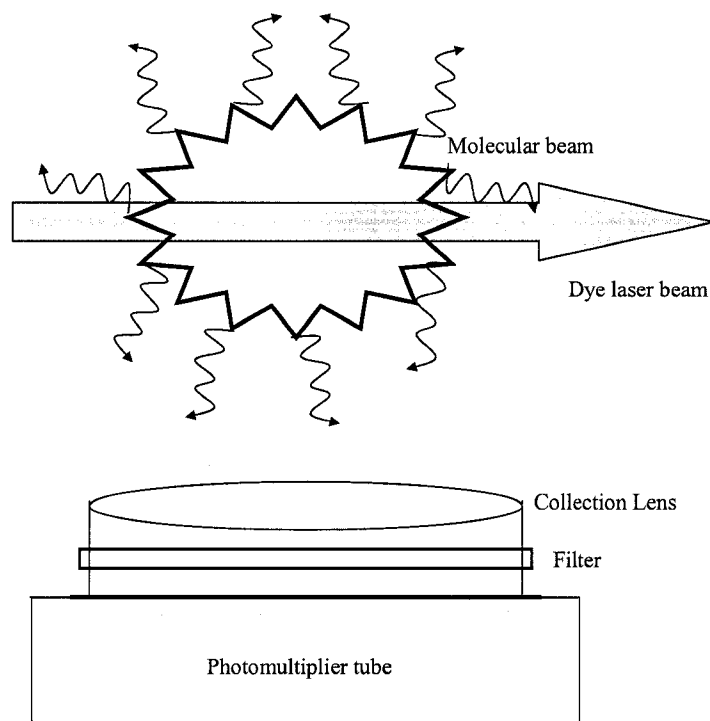


Figure 5. Generic laser induced fluorescence scheme.

In the general setup, tunable laser light is passed through the sample (molecular beam) and any fluorescence produced is collected off-axis, at a right angle to the laser beam by a collection lens. For our experiment the laser setup is a bit more complicated. We use two scannable lasers one of which is held at 226 nm to excite the molecule of interest (HMX or RDX) and a second one to probe for a specific decomposition product (OH)⁵. See Figure 6 below. The light is detected by a photosensitive device, a photomultiplier tube (PMT). The PMT is extremely sensitive and is capable of detecting a single photon. When the laser is off-resonance no fluorescence will be produced and the PMT will register no signal, but when resonant fluorescence is possible, absorption can be registered by detecting emission from the excited state. Therefore, a spectrum is obtained by measuring the fluorescence intensity as a function of laser wavelength. This specific spectroscopy method is called laser excitation spectroscopy³.

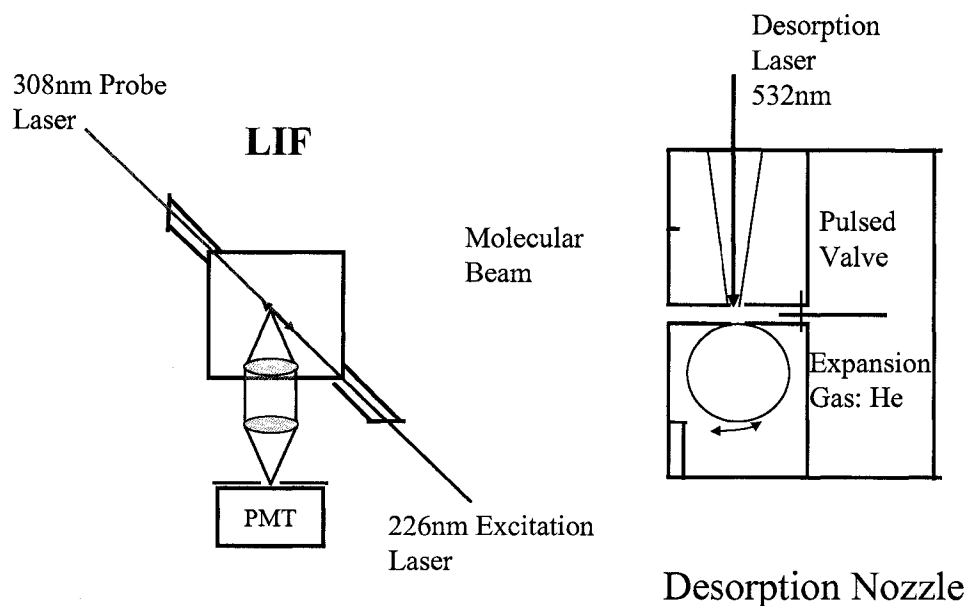


Figure 6. LIF experimental setup

Laser excitation spectroscopy, while similar to absorption spectroscopy, is dependent upon both the absorbance of the sample (RDX, HMX, or CL-20) and the fluorescence quantum yield of the excited state for the molecule being probed (OH). The fluorescence quantum yield is defined as

$$\Phi_f = \frac{\text{rate of photon emission by excited state}}{\text{rate of photon absorption}} \quad (4)$$

If all the molecules excited to the upper electronic state were to relax via only photon emission the fluorescence quantum yield would be one. However, other decay routes (non-radiative decay, e.g., intersystem crossing to a triplet state or internal conversion to the ground states,...) can lower the fluorescence quantum yield or even cause it to change from one excited state level to another.

LIF spectroscopy is very sensitive due to the low background signal received by the PMT at off-resonance laser wavelengths. A high signal to noise ratio can be achieved because the off-resonance signal can be made much smaller than the detected

fluorescence. One must properly account for any possible off-resonance signal detected by the PMT, namely laser scatter. This is minimized in a couple of ways: 1) by decreasing scatter sites (using baffled tubing for input/ output of the laser beam into the chamber); and 2) by using an optical filter, in front of the PMT, which will only transmit certain wavelengths.

The LIF experiments were done in efforts to detect the OH molecule. Observation of the OH molecule would suggest HONO is a possible precursor in the decomposition mechanisms of RDX and HMX. Unfortunately, the OH molecule has an IP = 13.1 eV making a non-resonant multi-photon absorption necessary for the ionization needed for the TOFMS experiments. This makes the LIF experiments a very practical alternative. The OH molecule is excited to its first excited state with 308 nm light⁵. Emission from the OH excited state would be equivalent to a MRES spectrum taken from the TOFMS setup. As previously mentioned the LIF experiments require two lasers to obtain the OH signal. The first laser excites the energetic material to its dissociative excited state and the second laser probes for the OH decomposition product. The two lasers enter the chamber 180° from each other and counter propagate perpendicular to the molecular beam. The arrival times of the two lasers and the laser desorbed molecular beam must be exactly in synch. In essence, this is a three laser experiment (desorption, excitation, and probe lasers) and the timing is controlled by two SRS delay generators. The internal 10 Hz triggering system of one delay generator is used to externally trigger the second delay generator keeping them synchronized. The two synchronized boxes are then used to externally trigger the rest of the equipment necessary for the experiment

(three lasers, pulsed nozzle, and box car). Please see Figure 7 for the electronic triggering schematic.

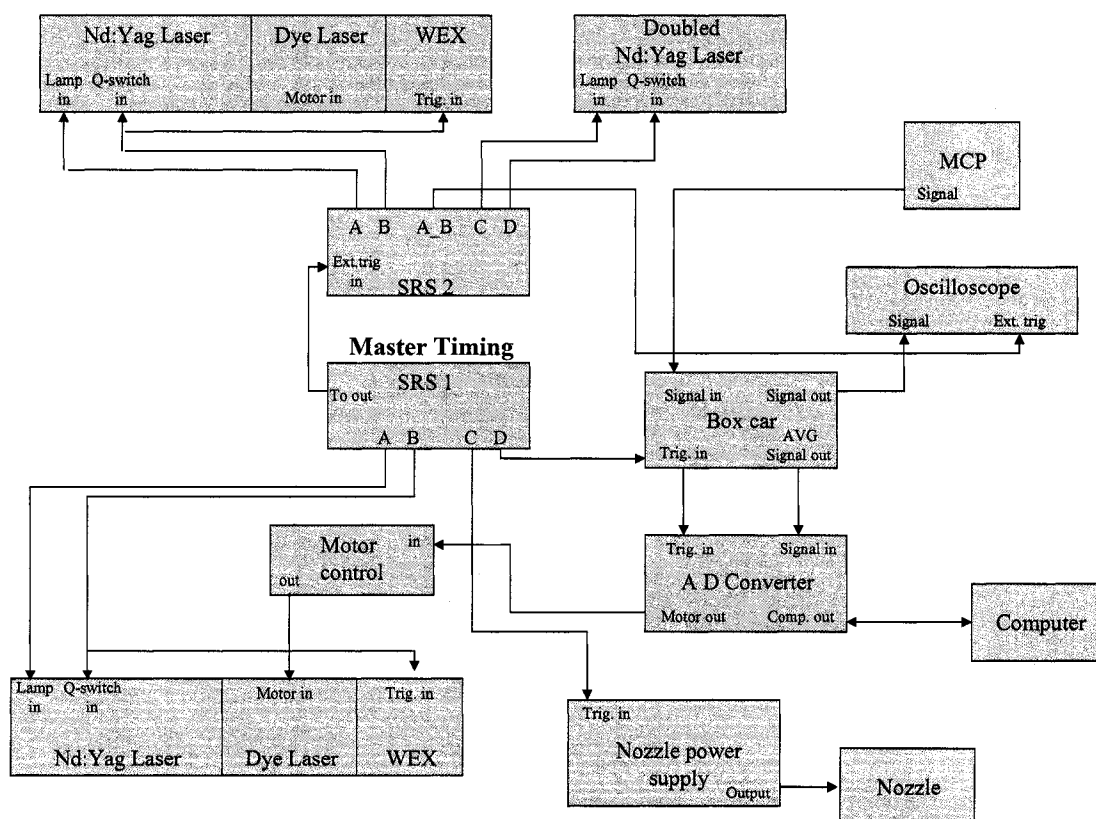


Figure 7. Electronic timing schematic for LIF experiment.

Time resolved spectroscopy

Femtosecond time resolved experiments involve a pump-probe configuration in which a pump pulse induces an excitation of the sample and the probe pulse looks for the response of the system to the excitation event created. The idea is to pump the sample, get it to behave the same way over and over again, and then probe it to find out what is happening over short intervals. Specifically, in our experiment, an ultrafast laser (226 nm) is used to pump the sample (molecular RDX, HMX, and model systems) to an

excited electronic state. The initial laser source is split into two beams, pump and probe, using a 50% beam splitter. The probe beam follows a different path which includes a variable delay line. The probe path length is changed by moving a motorized linear stage (Thorlabs). In essence a retro-reflector (two mirrors at 45° angles to each other) is positioned on a stepper motor controlled linear stage. As the stage is moved backwards the probe beam follows a longer path length than the pump beam (Figure 8). The linear stage can be moved in very small intervals (13 fs steps) giving high temporal resolution to the time evolution of some property of the system (decomposition product onset). It is important that the two beams, after following different optical paths, are directed and focused on the same spatial area in the sample taking care that the probe beam is always within the excitation beam.

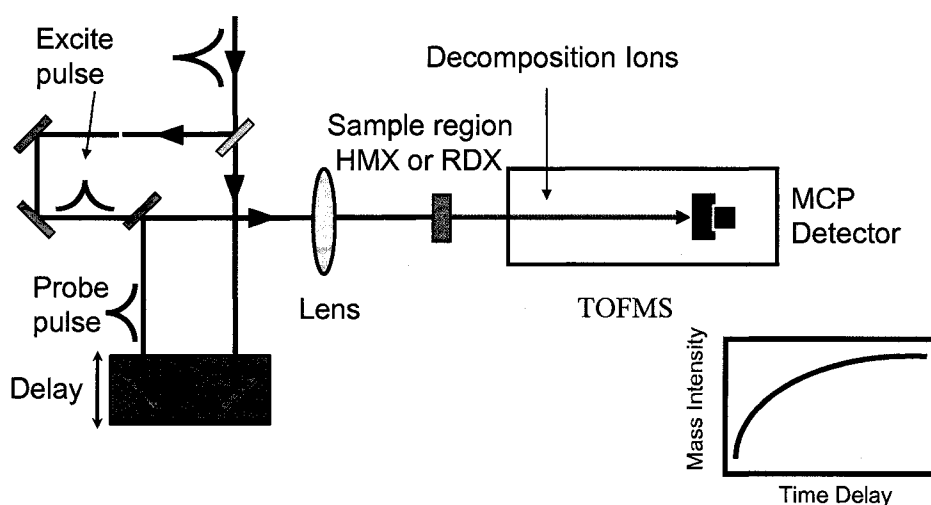


Figure 8. Generic femtosecond experimental setup.

The time resolved excited state decomposition experiments, performed on HMX, RDX, and the model systems, were done in efforts to measure the onset of the initial decomposition product, the NO molecule. These experiments use the TOFMS

experimental setup defined previously. The pump pulse excites the gas phase material and the probe pulse uses the 1+1 resonant absorption of the NO molecule to ionize it. Scanning through the time delay between the pump and probe yields information on the dynamics of the decomposition reaction. Namely, the onset time of the NO molecule is directly related to the decomposition dynamics of the electronically excited energetic material or model system.

For the pump-probe experiment to work one must ensure the two beams are overlapped temporally and spatially. The spatial overlap must be constant over the delay time scanned to ensure accurate measurements. Obtaining spatial overlap requires knowledge of the two beam paths. An ultrafast 226 nm light beam is split into equal pump and probe beams using a 50% beam splitter. The pump beam follows a defined path and is focused, by a curved mirror, into the molecular beam, exciting the sample, in the TOFMS ionization region (Figure 9). The probe beam, following a different path with a variable path length delay stage is recombined with the pump pulse using another 50% beamsplitter. The two beams, pump and probe, are made collinear over a 5 meter path length. The probe beam is focused by the same curved mirror into the molecular beam. To check for spatial overlap, gas phase furan, which has a non-resonant single photon but resonant two photon absorption at 226 nm, is used. When the two beams are overlapped spatially, yet not temporally, there will be a two times increase in the furan ion signal detected by the TOFMS. Due to the focusing of the two beams (pump and probe) slight alignment adjustments should drastically change the spatial overlap of the two beams.

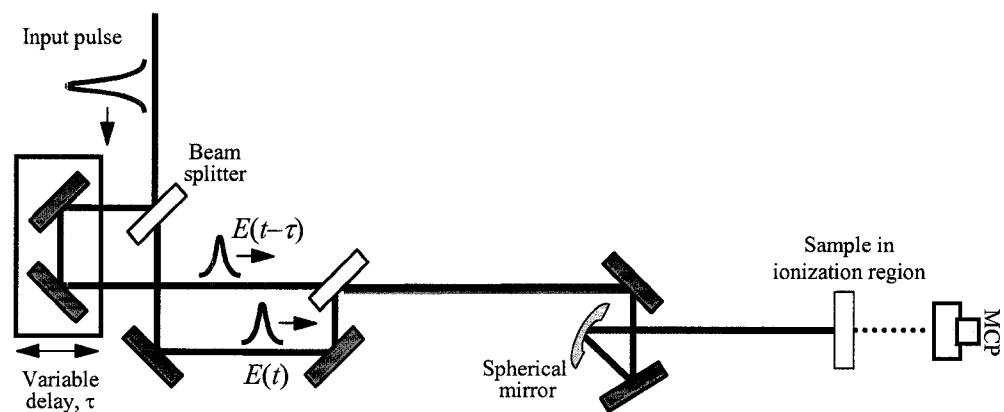


Figure 9. The pump-probe setup used in our experiment.

Temporal overlap can only be observed when there is also spatial overlap, thereby impeding the alignment procedure. Three different wavelength combination pump-probe studies were performed (226 nm/ 226 nm, 400nm/ 266 nm, 800 nm/ 800 nm). Each wavelength combination requires a different temporal overlap procedure. I will document each procedure in the following three paragraphs.

For the 226 nm/ 226 nm pump probe experiments the easiest method for finding overlap is to look at the two collinear beams on a fluorescing business card, for diffraction rings. As the beams are slightly overlapped in time many diffraction rings will be observed. When the time delay between the two beams is decreased ($\Delta t \sim 0$) and the spatial overlap is optimized, the beam pattern will change from diffraction rings to almost a beating pattern, somewhat like a constructive/ destructive interference pattern. Here you are looking at a very widely spaced diffraction size. Once the interference pattern is observed the non-resonant absorption of the furan molecule can be used to optimize alignment, in the molecular beam, and to exactly determine where $\Delta t = 0$ by scanning the delay between the pump and probe beam and recording the furan ion

intensity. See the autocorrelation measurements, in figure 12, for a representation of proper pump-probe overlap.

The temporal overlap of the 400 nm/ 266 nm pump-probe beams is quite different than the 226 nm beams. For the two color experiment the long lifetime of NO gas was utilized. The NO molecule has an excited state lifetime $>100\text{ns}$. Knowing this, the delay time of the probe beam was made much greater than the pump. The spatial overlap was adjusted to see the largest ion signal and the time delay was decreased until no enhancement was observed ($\Delta t \sim 0$). Spatial overlap was further optimized and the delay time was scanned again to find $\Delta t = 0$.

The 800 nm/ 800 nm pump-probe overlap required the use of a fiber optic spectrometer (Ocean Optics). The two collinear beams are directed into the spectrometer and when they are close to being overlapped both spatially and temporally an interference pattern, on the spectrometer display, will be observed. Similar to the 226 nm overlap, as the overlap of the two beams are optimized in time and space the interference pattern will become weaker but will have a “beating” pattern on top of it. Once close to the time and space overlap, the non-resonant absorption of the furan molecule can be used to optimize alignment and exactly determine $\Delta t = 0$.

The timing of the pump-probe experiments is key to a successful study. The femtosecond laser system can not be externally triggered; therefore the repetition rate of the oscillator, 91 MHz, is counted down to a 10 Hz signal. The 10 Hz signal, which must be in synch with the oscillator output is delayed properly and used to trigger the desorption laser, pulsed nozzle, and box car averager (Figure 10). The molecular beam and the fs pump beam must arrive at the TOFMS ionization region at the same time. In

acquiring data the probe beam is given a negative delay and scanned through the $\Delta t = 0$ point into positive delay. The response of the system excitation is probed through this process and recorded by observation of a particular ion intensity.

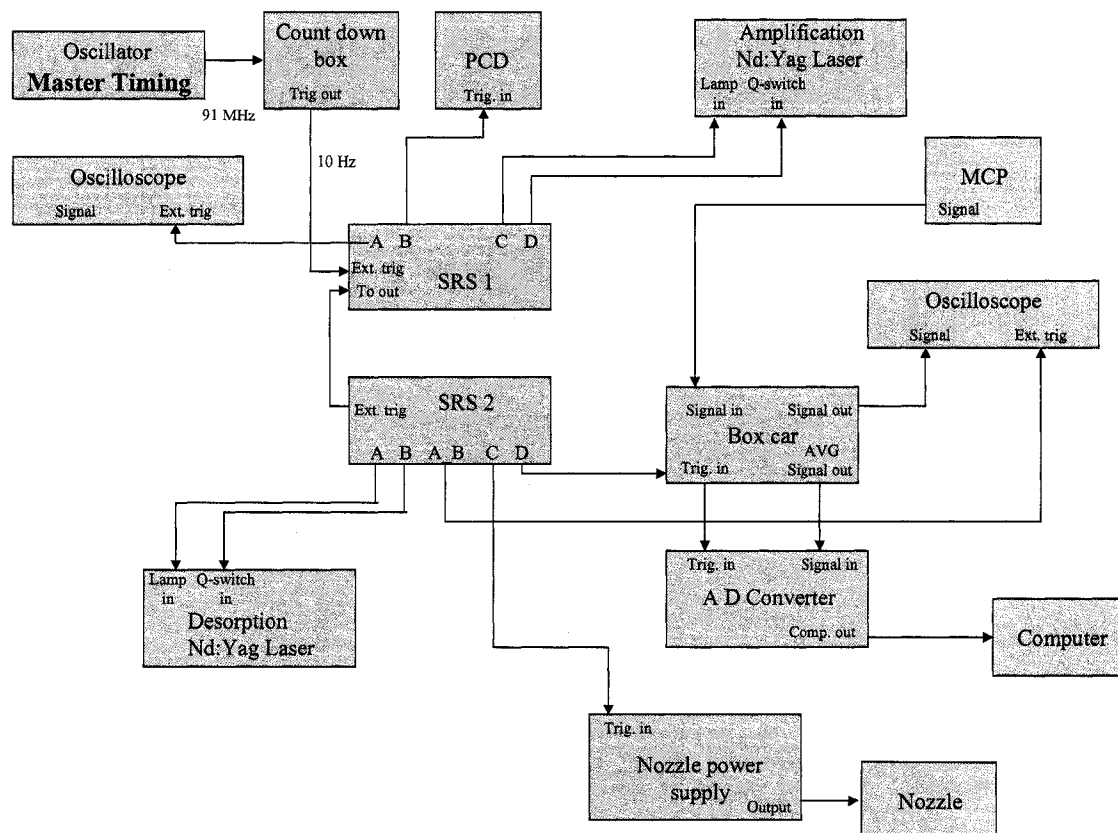


Figure 10. Electronic timing schematic for the femtosecond system.

Finally, to understand the time resolved experiments better, the time duration of the 226 nm light was measured using two techniques: a fused silica self diffraction autocorrelation method and the multi-photon non-resonant absorption of the furan molecule. The general idea behind both measurements revolves around the difference in a measured intensity (1st order diffracted light intensity or ion signal intensity) as the temporal overlap is changed between the pump and probe beams. Once again it is

imperative that the spatial overlap remains the same during the measurement. The optical setup for the non-resonant absorption autocorrelation measurements is exactly the same as in the experimental pump-probe setup. The self diffraction setup differed only in the fact that the pump and probe beams were not collinear (Figure 11). They crossed each other, at 20° angles, as they interacted with the non-linear medium fused silica. In both autocorrelation measurements the pump and probe beams are focused into the medium and the non-linear response for the medium is recorded (Figure 12). Autocorrelation measurements do not account for the spatial profile of the pump and probe beams. Assuming the two beams have a Gaussian intensity distribution a $\sqrt{2}$ correction factor must be used to determine the true time duration of the laser. The time duration measured for the 226 nm light is ~ 180 fs.

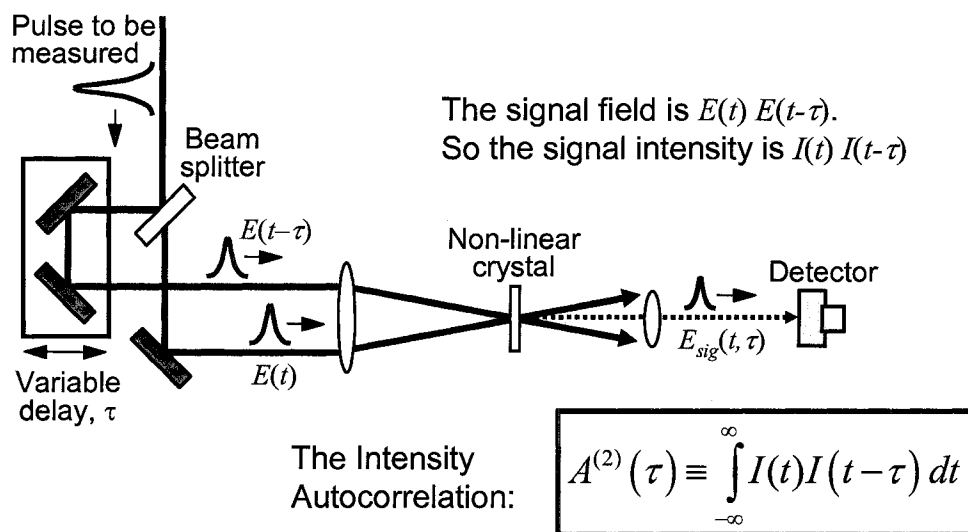


Figure 11. Generic autocorrelation schematic (figure from Rick Trebino).

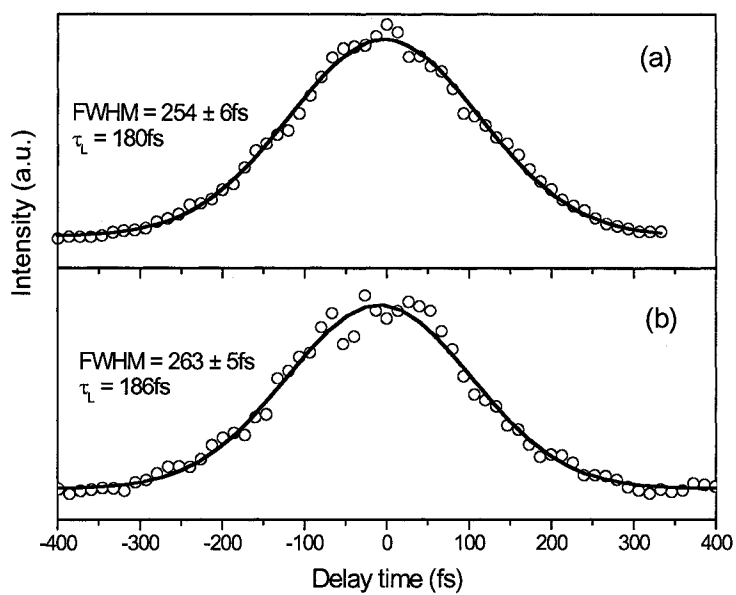


Figure 12. . Measurements of the femtosecond laser pulse duration at 226 nm using a self diffraction autocorrelator (a) and off-resonance two photon absorption of the furan molecule (b).

References

- (1) Im, H. S.; Bernstein, E. R. *Journal of Chemical Physics* **2000**, *113*, 7911-7918.
- (2) *Atomic and Molecular Beam Methods*; Scoles, G.; Bassi, D.; Buck, U.; Laine, D., Eds.; Oxford University Press: New York, 1988; Vol. 1.
- (3) Ellis, A.; Feher, M.; Wright, T. G. *Electronic and Photoelectron Spectroscopy*; Cambridge University Press.
- (4) Cotter, R. J. *Time of flight mass spectrometry*; American Chemical Society: Washington, DC, 1994.
- (5) Luque, J.; Crosley, D. R. *Journal of Chemical Physics* **1998**, *109*, 439.

Appendix 2: Femtosecond laser system

Overview

Ultrafast pulses can be utilized to monitor extremely fast processes, specifically the dynamics of fast photon induced chemical dynamics. The dynamics can be measured using a pump-probe setup in which a pump pulse excites the medium and a probe pulse further detects the outcome of the medium. The time delay difference between the pump and probe pulse defines the dynamics of the medium.

Ultrafast pulses provide higher peak laser intensities necessary for non-linear processes and allow for investigation of atomic, molecular, plasma and solid-state physics. Ultrashort pulses were first obtained using a colliding pulsed modelocked (CPM) ring dye laser. The downfall of this laser was its overall time limit (27 fs) and its instability, namely the deterioration of the gain material. The first broadband solid-state fs laser was confirmed in 1990¹. This self-modelocked Titanium doped sapphire laser was not only much more stable than the previous CPM fs laser but also much easier to operate and align. The solid state gain material, Ti: Sapphire, has a broad gain bandwidth (700-1100nm) that in theory can support pulses as short as 4 fs. This material absorbs in the blue/ green visible spectrum and has a relatively high gain cross-section.

The fs laser used in our experiment consists of a chirped-pulse amplification (CPA) system, which is further compressed and followed by an optical parametric amplification system. The entire laser system produces variable wavelength light with varying time duration (<200 fs). Specifically, the non-linear optical processes can

generate 2000 nm – 188 nm light. The CPA process allows for an increase in energy of a short pulse while evading high peak powers in the laser amplification process. The amplification process requires the short pulses to be stretched out in time via dispersion. The longer time duration of the pulse allows for more energy to be extracted from the gain medium and also diminishes the possibility of optical damage by decreasing the peak power seen by the gain medium.

The CPA process used for our experiment consists of an oscillator, a stretcher, and an eight-pass ring amplification cavity. After the pulses are amplified (10^6 gain) they are compressed back into a fs time duration (Figure 1). The amplified fs light has a center wavelength of 805 nm, 1.5 mJ energy, a 10 Hz repetition rate and 25 fs time duration.

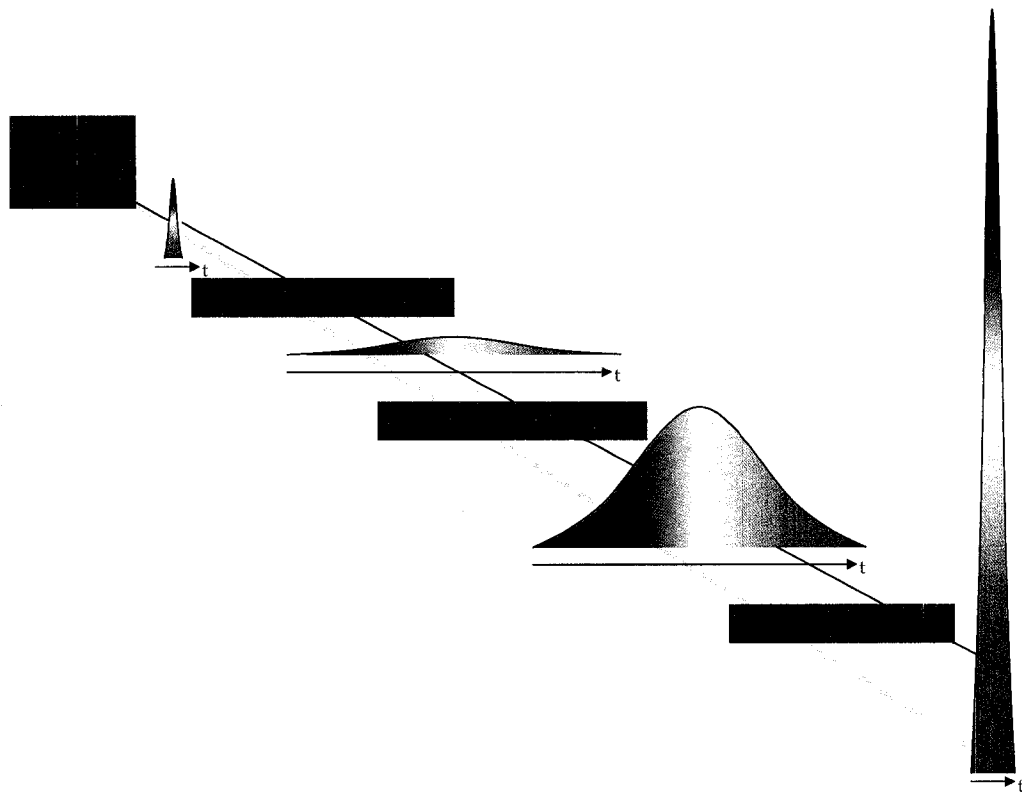


Figure 1. Chirped pulse amplification.

To obtain the high energy amplified fs light an initial low energy fs light source is produced by an oscillator laser cavity. The high repetition rate, low energy fs light out of the oscillator is then sent through a grating pair whereby the pulse time duration is stretched 3 orders of magnitude (fs to ps). The ps light then passes through a Pockels cell or optical shutter, which decreases the repetition rate to 10 Hz. This 10 Hz chirped light is then used as the seed beam for the amplification process. The amplifier consists of a ring cavity where eight passes through the cavity allows for a 10^6 gain. The high energy (2.5 mJ), 10 Hz, 800 nm light is then compressed back to fs time duration using a grating pair. Optical parametric amplification is subsequently instilled to obtain the variable wavelength fs light necessary for our experiments. The following sections will first delve into the concepts behind the laser setup and finish with a detailed step-by-step alignment procedure.

Oscillator

The oscillator used in our system (KM Labs) is pumped with 4.75 W of continuous wave (CW) 532 nm light (Coherent, Verdi Laser) and can run in two modes CW and modelocked. Figure 2 below shows the oscillator schematic. The CW 532 nm light enters the oscillator so that it is collinear with the cavity and is focused onto the gain medium. The generated 800 nm light must then pass through a prism pair, to compensate for the dispersion acquired in the crystal², reflect off of a high reflector and return along the same path so that it can pass out of the cavity through the output coupler. To obtain ultrashort pulses the gain medium must have broad bandwidth and the various frequencies generated in the cavity must be in phase or “modelocked”. The time duration of the laser pulse is directly proportional to the amount of in-phase bandwidth.

(Figure 2)

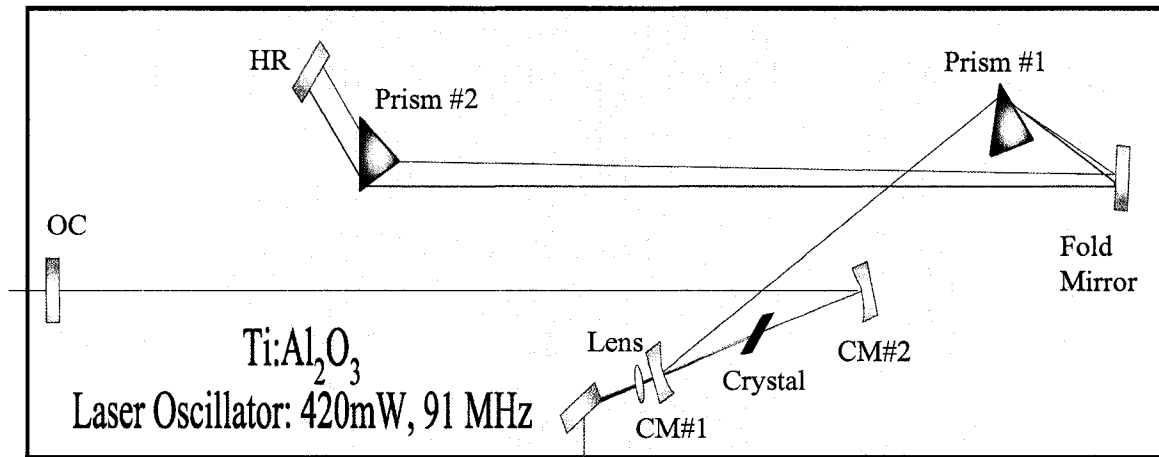


Figure 2. Femtosecond Oscillator

The Kerr lens effect allows for a modelocking mechanism to occur within the oscillator³. In a solid state laser the Kerr lens effect arises due to the nonlinearity of the laser crystal (Ti:Sapphire)⁴. This effect is dependent upon the non-linear refractive index of the Ti: Sapphire crystal. By matching the mode of the pump laser beam (532 nm) to that of the modelocked beam, the pump beam creates a “soft aperture” which will allow for cavity selection of the pulsed beam. If a noise spike is induced within the cavity, modelocking will occur. The spike will experience a higher refractive index or greater phase shift than the surrounding area allowing for more gain than the CW mode of the oscillator. The “spike” will build in intensity creating a stable oscillating pulse thereby modelocking the cavity⁵.

Dispersion causes different wavelengths of light to traverse a dispersive material or device at different speeds, thereby spreading a spectrum (pulse duration) temporally. Different wavelengths will experience different phase shifts (Φ) as they encounter a

dispersive material and the derivative of the phase shift with respect to angular frequency ($T(\omega) = \frac{d\Phi(\omega)}{d\omega}$) is defined as the group delay. Dispersion is best understood in terms of group delay; different frequencies will experience different group delays thereby spreading the spectrum temporally. The increase in pulse time duration due to dispersion is one of the main impediments to ultrashort pulse generation. For most materials dispersion will cause shorter wavelengths to lag behind longer wavelengths. These “positively chirped” or “positively dispersed” pulses will be broadened in time. The dispersion encountered in the oscillator must be corrected for to ensure most efficient modelocking occurs. If not corrected the wavelengths on either end of the broad spectrum will have different group delays and will not oscillate in synch with the main pulse in the cavity. The Kerr lensing effect will then eliminate them due to the lower amount of gain they will obtain. Dispersion control is imperative in order to obtain ultrashort pulses.

Within the oscillator, dispersion is controlled using a prism pair. The ‘positive chirp’ instilled on the pulse due to the dispersive gain material (Ti:Sapphire) is compensated for using an opposite negative chirp. The prism pair allow for the bluer parts of the spectrum to travel a shorter optical distance, which in effect allows them to “catch up” with the redder parts of the spectrum. This cancels out the positive dispersion obtained from the gain medium (see **Figure 3** below)

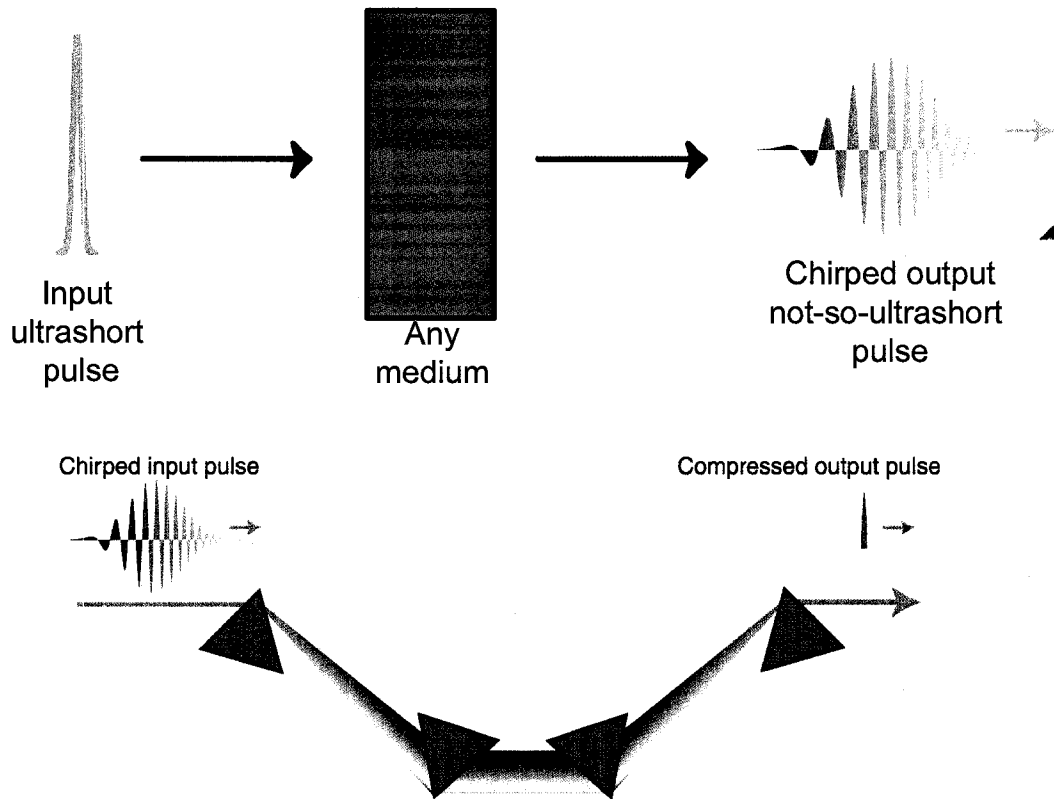


Figure 3. Concept of dispersion (www.physics.gatech.edu/gcuo/ultrafastoptics)

Our oscillator produces light pulses with a 790 nm center wavelength at a 91 MHz repetition rate. The cavity length defines the repetition rate. The output power is around 400 mW and the pulse has a bandwidth of 65-70 nm. Measurement of the pulse time duration using a frequency resolved optical gating (FROG) device gives a pulse duration of 50 fs. Light out of the oscillator is collimated using a 1 meter focusing lens and sent to the stretcher.

Stretcher

The stretcher increases the pulse time duration by introducing a frequency chirp onto the pulse. The time duration of the pulse out of the oscillator is increased by a factor of 10^3 - 10^4 from fs to ~ 100 ps. The frequency chirp is established using a grating pair

arrangement whereby the spectrum of the pulse is separated so that the different colors of light follow a different path through the optical system. Fig. 4 represents the stretcher used in our system except that we use an all-reflective design^{6,7} to avoid chromatic aberrations instilled on the pulse by the lenses. Because there is a telescope placed in between the grating pair, the distance between the second grating and the image of the first grating controls the dispersion of the stretcher^{8,9}. When this distance is negative the system stretches the pulse in time but when it is positive it compresses the pulse in time. The time duration of the pulse is stretched to avoid damage to the optics in the amplification process. After amplification the same process is used to compress the pulse back to short time duration thereby making a stretcher/compressor pair.

(Figure 4)

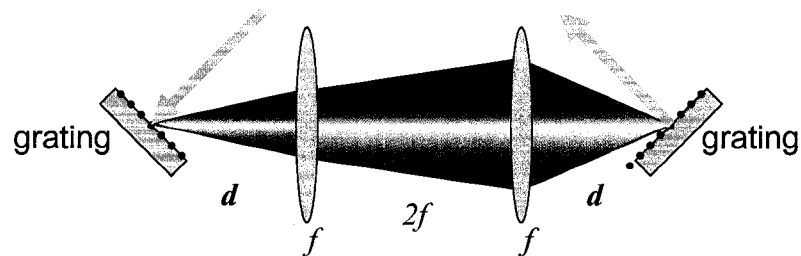


Figure 4. Stretcher schematic (www.physics.gatech.edu/gcuo/ultrafastoptics).

The stretcher contains two gratings anti-parallel to each other and separated by an even number of lenses. This setup induces a large amount of positive dispersion on a pulse and stretches it in time⁸⁻¹⁰. The first stretcher design contained two identical lenses, of focal length f , separated by $2f$ (Fig 4 above). The two anti-parallel gratings were a distance d from the nearest lens. In this design the necessary grating separation is

-2(f-d). The beam passes through the stretcher and a retroreflection mirror sends the pulse back through the system with a slight lateral deviation enabling separation from input beam so that it can be picked up and further sent to the amplifier. The stretcher in our experiment uses an all-reflective folded, single grating design, with a single spherical mirror and two flat mirrors⁶. This design allows for the stretcher to be optimized and the output chirp of the amplifier to be varied without misaligning the optical systems after the stretcher.

The pulse out of the stretcher has a time duration of about 100 ps and a repetition rate of 91 MHz. The amplifier, as well as everything else in the lab, runs at a rate of 10 Hz; therefore the stretched pulse must be counted down to a 10 Hz repetition rate. This is done using an optical shutter called a Pockels Cell. The Pockels cell contains a birefringent crystal (KDP) that can change the polarization of the input beam from horizontal to vertical. Every 10 Hz a large potential difference is applied across the crystal changing the polarization of the input beam. This process has a very short window (11 ns) allowing a single pulse out of the 91 MHz train to be selected. The vertically polarized pulse is picked out of the remaining 91 MHz pulse train by a polarizing cube. The polarizing cube allows the vertical polarized light to travel straight through the optic while the horizontally polarized light travels a different path and is blocked. The light entering the amplifier must be horizontally polarized. Therefore the resulting 10 Hz vertically polarized light passes through a half-wave plate, which changes its polarization to horizontal.

Amplifier

The 10 Hz 800 nm pulse train from the Pockels cell becomes the seed beam for the amplification process. Namely it stimulates 800 nm emission from the Ti:Sapphire amplifier gain material. The amplifier configuration is represented in Figure 5. It is an eight pass ring cavity that yields a 10^6 gain in energy. Specifically, the energy of the seed beam is 10^{-9} J while the amplified pulse is 2.5 mJ. The gain medium Ti:Sapphire was developed in 1982 by Peter Moulton¹¹. It has a high damage threshold ($2\text{-}5 \text{ J cm}^{-2}$), a high saturation fluence ($\sim 0.9 \text{ J cm}^{-2}$), a high thermal conductivity (W /m K) and a good peak gain cross section $\sigma_g = 2.7 \times 10^{-19} \text{ cm}^2$, thereby making it a fine high power amplifying material. Also Ti:Sapphire has a broad absorption around 500 nm making a doubled Nd:YAG laser (532 nm) ideal for pumping the gain material.

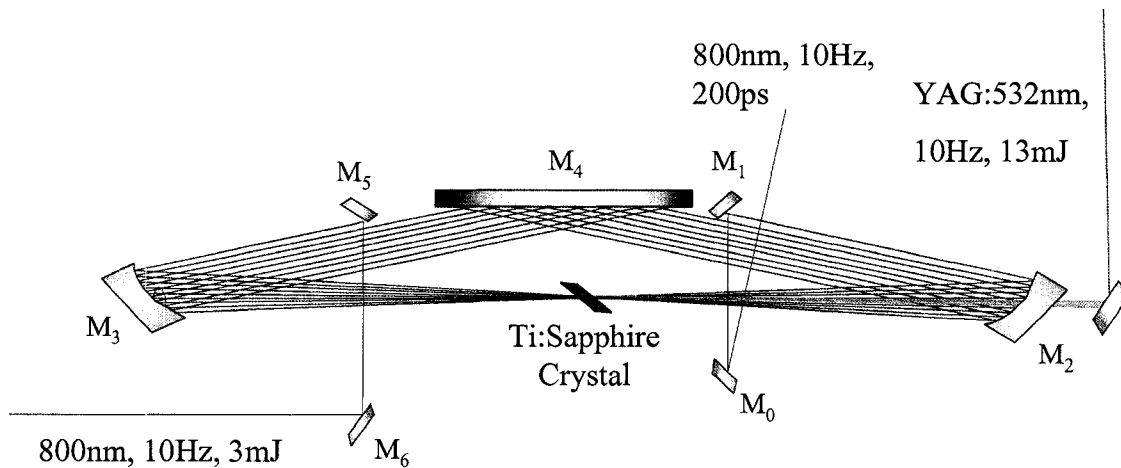


Figure 5. Amplifier- eight pass ring cavity.

Ideal beam characteristics are necessary for the 532 nm pump beam. Most importantly the beam must have a Gaussian intensity distribution without any “hot spots”. To ensure the pump beam has the best beam profile a telescope along with a spatial filter has been used. First a telescope collimates and decreases the size of the

beam by half (4-5 mm diameter). A spatial filter, which consists of pinhole located at the focal point of a telescope system, is then used to allow only the TEM₀₀ mode to propagate further. A TEM₀₀ mode focuses better than higher order modes and therefore the higher order modes are blocked by the 40 μm pinhole within the spatial filter. The resulting TEM₀₀ mode has a Gaussian intensity distribution with a good beam profile. This modified beam then passes through a focusing lens and is directed into the amplifier cavity along an axis similar to the seed beam. The 14.5 mJ 532 nm pump beam focuses approximately 2 cm before the Ti:Sapphire crystal and its 2 mm image is directed onto the crystal so that the pump and seed beam are overlapped both spatially and temporally.

The 3 μs radiative lifetime of the excited gain medium allows for the seed beam to easily pass through the medium 8 times stimulating emission so that an overall gain of 10⁶ can be obtained. The eight passes through the cavity must be parallel and come to the same point within the gain material. The main components of the amplifier cavity are the gain material (Ti:Sapphire), two 1 m center of curvature spherical mirrors, and one long flat mirror (Figure 8). The two spherical mirrors essentially form a telescope which collimates the beam. The gain material is located at the focal point of the telescope. The 0.25 % Titanium doped crystal must be cut along the crystal's c-axis. This allows for the pump laser and amplified pulse to be along the highest gain cross section giving the best amplification.

The final pass through the amplifier cavity is 'picked up' by an output mirror and sent through another spatial filter. This spatial filter selects the best 800 nm beam profile and increases the magnification of the pulse 5 times. The pulse size is increased to decrease the possibility of damaging the optics in the compressor. The amplified 800 nm

pulse has a center wavelength of 804 nm, 2.5 mJ of energy, and a 10 Hz repetition rate. This light is then sent to the compressor, which compresses the light back to fs time duration. A frequency resolved optical gating (FROG) system is instilled to measure the time duration of the compressed 800 nm fs light. A FROG trace from our laser system as well as examples of FROG traces for systems that are not well aligned can be found in Appendix III pictures, at the end of this chapter.

Compressor

2.5 mJ of 800 nm light with a time duration of ~100 ps is sent into the compressor. The compressor pairs with the stretcher in that it uses negative dispersion to decrease the time duration of the positively chirped pulse. The compressor consists of a pair of identical parallel gratings (Fig. 5). The optical path or transit time of shorter wavelengths will be shorter than that of the longer wavelengths. The optical path P along ABC in fig. 5 is expressed as:

$$P = \frac{L_g(1+\cos(\gamma-\theta))}{\cos\theta}.$$

The different angles γ and θ are found from the grating equation

$\sin \gamma + \sin \theta = \frac{\lambda}{d}$; d is the grating groove spacing¹². Longer wavelengths have a larger grating diffraction angle θ , which increases their optical path generating a negative chirp.

(Figure 6)

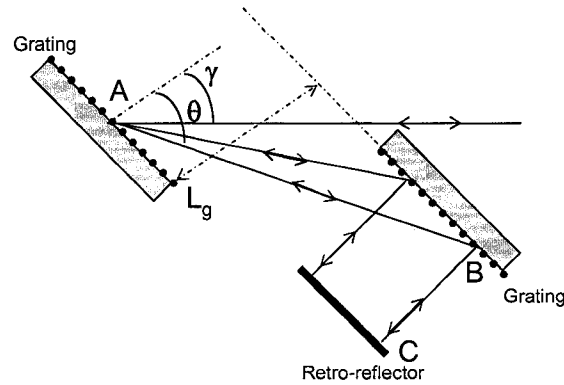


Figure 6. Pulse Compressor

After compression the amplified pulses have a measured time duration of 25-30 fs, a center wavelength of 804 nm, and a repetition rate of 10 Hz. These pulses are further used to pump the nonlinear optics of our optical parametric amplifier.

TOPAS

The TOPAS (traveling-wave optical parametric amplification of superfluorescence) allows for generation of a wide range of wavelengths (2 μm to 188 nm). Pumping a BBO crystal in a type II phase matching configuration produces the tunable wavelengths. The crystal produces two different wavelengths, a signal and idler for a specific BBO crystal orientation when phase matching occurs. The TOPAS operation is built upon a second order nonlinear optical process, the three photon parametric interaction occurring within a noncentrosymmetric crystal. Our 800 nm pump pulse (ν_3) provides two other frequencies (ν_1, ν_2), the signal and idler, when it interacts with the nonlinear crystal and upholds the frequency matching condition:

$$\nu_3 = \nu_1 + \nu_2.$$

Superfluorescence is generated in the first of a five stage process and is used as a seed beam for the remaining 4 passes through the cavity. The second and fourth passes

through the crystal pre-amplify and shape the beam. The third pass through the crystal has negligible amplification, but the fifth pass, which is pumped by the bulk of the pump energy significantly, amplifies the energy of the parametric pulse. It is essential for the pump beam to have high spatial coherence and no spatial or temporal beam distortion. The pump beam must also be “non-tilted” meaning the pulse group fronts (intensity contours) must not be tilted with respect to the perpendicular of the beam propagation direction¹³ (see Figure 7 below). These characteristics along with a carefully adjusted pump beam size in the pre-amplification stages yield an output beam with a divergence close to the diffraction limit¹⁴.

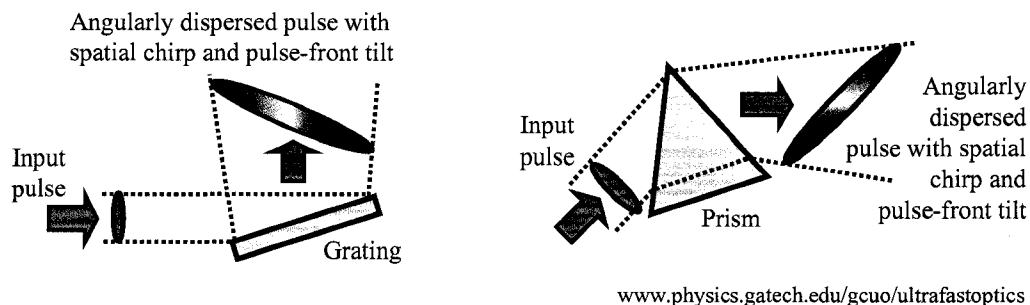


Figure 7. Spatio-temporal distortion is known as pulse-front tilt. It occurs when different frequency components of the beam propagate at different angles.

The wavelength necessary for our experiment, 226 nm, is produced from the third harmonic of the signal at 1260 nm. The third harmonic of the signal beam at 1260 nm, 315 nm, is mixed with 800 nm light yielding the necessary 226 nm light.

ALIGNMENT

This section will include a combination of instructions given by KMLabs, Coherent Laboratories, as well as alignment instructions for our homemade amplifier

cavity. I have also included a bulleted stepwise alignment procedure for the oscillator and hints or suggestions for alignment of other sections of the laser.

Oscillator Alignment (complete realignment):

CONTINUOUS WAVE (CW)

Note: Initial oscillator alignment should be carried out at very low 532 nm pump power (.2 W). Only turn up the pump power (4.75 W) when the cavity is aligned well enough to obtain lasing. See figure 2 above for oscillator schematic.

1. Take out all of the optics on the rail (lens, curved mirror 1, crystal, and curved mirror 2).
 - a. Remove the curved mirrors from their mounts; don't remove the mounts.
2. Propagate the 532 nm continuous wave pump beam straight down the rail. Use the aperture to ensure the 532 nm beam is properly positioned (height and horizontal) at the beginning and end of the rail. The green halo should be even around the aperture.
3. Replace the lens. Move the lens forwards and backwards along the rail and observe the position of the green pump beam on the aperture at the end of the rail. If the green pump beam is hitting the center of the lens, as it should, there should be no movement in the pump beam as the lens position is changed.
4. Replace the 2 curved mirrors. Ensure the green beam is still somewhat centered on the aperture at the end of the rail (Note: not much care is taken

in doing this, just make sure that the green beam is centered on the aperture)

5. Replace the crystal.
 - a. Move the crystal back and forth along the rail to make sure that there are not any specks of scatter. Scatter indicates crystal damage. If there is damage move the crystal until the scatter disappears, but ensure the green beam is not too close to the copper crystal holder.
 - b. Place the crystal along the rail so that the beam hits its center.
 - i. To ensure the angle of the crystal, with respect to the pump beam, is correct one can also unscrew the phillips head screws on the crystal mount and slightly rotate the crystal. Look for the green reflection off of the crystal. The reflection should be located on the other side of the oscillator near prism # 1. Rotate (left and right) crystal slightly until green reflection is most dim. Tighten screws on crystal mount.
6. Rough alignment of curved mirrors # 1 and # 2 (CM #1, CM # 2)
 - a. CM # 1
 - i. Make sure the large circular fluorescence height is correct before prism 1, after prism 1 and behind the fold mirror. Make the necessary adjustment with CM # 1 mirror mount.

- ii. Fluorescence should clip a little bit off of the front of prism # 1.
- b. CM # 2
- i. Use CM # 2 mirror mount to center the green pump beam on the output coupler (OC).
 - ii. The approximate position of curved mirror 2 along the rail is determined by observing the fluorescence. Move CM # 2 until the fluorescence focuses about 5-10 cm after the OC. (If the focus occurs further than 10 cm after OC it indicates the curved mirror is too close to the OC.)

Crystal: After both CM # 1 and CM # 2 are roughly adjusted, check the fluorescence before prism 2. There should be a linear focus within the larger fluorescence spot. Move the crystal along the rail until this is observed.

7. Minimum deviation (Only necessary if prisms are replaced.)

- a. Prism #1
 - i. Place a card by the HR moving the prism # 2 out of the way.
 - ii. Loosen the prism mount-make sure that you hold the mount because once loosened it rotates as well as translates and we only want rotation.

iii. In rotating it you will see the image contract along its horizontal direction and then return to its initial position. The prism should be locked down right before the image starts to contract.

b. Prism # 2

- i. Repeat the same process for prism # 2
- ii. To look at the image you have to really misalign the HR reflection – the reflection should hit behind the green turning mirror.

8. Fluorescence overlap

- a. Observe the incoming and reflected beams between the HR and prism # 2. Adjust the HR to overlap the two beams.
 - i. This is accomplished by using a thin card. Move it in and out of the incoming and reflected beam adjusting the HR mirror to obtain overlap.
- b. Observe the incoming and reflected beams between the OC and the aperture. Adjust the OC to ensure the reflected green beam is overlapped with the fluorescence/lasing.
 - i. There will be a few green reflections due to the wedge design of the OC. Align with the brightest green beam reflected; it should also have fluorescence (red) reflected with it.

9. Repeat procedure 8 a couple of times. Aligning one side of the cavity (OC) tends to misalign the other side (HR) therefore this is an iterative process. Once there is overlap at the HR and OC turn up the 532 nm light (4-5 W) and look for lasing. It is easiest to find lasing if the cavity is over pumped (532 nm > 4.75 W). Use the HR and OC to peak up power.
10. Observe the mirrors. Lasing should:
 - a. Reflect off the center of CM # 1 and OC,
 - b. Be reasonably well centered on the HR and fold mirror, (it should be at least 2/3 centered because one only sees the bluer part of the lasing spectrum and one wants to make sure the red part of the spectrum, to the right, is not clipped)
 - i. To move the lasing spot on the HR use the fold mirror (note: fold mirror is extremely sensitive so only small adjustments are necessary)
 - ii. CM # 1, the fold mirror and the HR are coupled. To obtain a horizontal movement of the lasing spot on the HR change the fold mirror and then tweak up power using the HR.
 - iii. Only small adjustments should be done. Example: a small adjustment of the folding mirror will cause the lasing to stop, get it back by adjusting the HR.
11. Check the red and green spot overlap on CM # 2. Make sure that they are collinear through the crystal. by When they are overlapped and the power is optimized they should be

1. vertically centered on CM # 2,
 2. offset horizontally from the center (to the right),
 3. $\frac{1}{2}$ overlapped, the green beam should be closer to the center of CM # 2 than the red beam.
12. Now optimize everything in the oscillator for power. Use the following procedure.
- a. Optimize in the following order: OC, HR lens, crystal, and CM #2.
 - b. For the OC and the HR make very coarse adjustments $\frac{1}{2}$ turns.
 - c. Move the lens until maximum power is achieved.
 - d. Move the crystal until maximum power is achieved.
 - e. Move CM#2 until maximum power is achieved.
13. Optimize the OC, HR, lens, crystal, and CM # 2 three times (at least) until the output power doesn't change more than 5 mW.
14. Check that there is still a focus after the OC (5-10 cm) and a line focus before prism #2.
15. Make sure that you are on the inside of the outer stability zone. The power should fall off quickly at the outer edge of the outer zone (smaller micrometer reading). Moving CM # 2 towards the crystal from the outer edge of the stability zone, the power should increase, fall off, and then increase again. This power variation defines the inner and outer stability zones.

16. If the foci are not about correct, and they probably won't be, adjust them until they are about correct and optimize the cavity again. The two foci are the CM # 2 focus after the OC, and the crystal focus before prism # 2.
17. Carefully check the lasing height. The height should be 59 mm.
 - a. Ensure the height before the OC is correct. Fix it with CM # 2 if need be and then tweak power back up with the OC.
 - b. Check height before HR in two places:
 - i. before prism # 1 (fix with CM # 1 and tweak up with HR)
 - ii. before prism #2 (fix with fold mirror tweak up with HR).
 - c. Check the height at the OC again, and repeat the process 2 times.
18. Optimize everything in the cavity again- OC, HR, lens, crystal, and CM #2 - until everything is stable to ~5 mW.
 - a. Average power obtained is about 1150 – 1200 mW.
19. Check the foci again and adjust appropriately.
20. Look for a good beam mode (TEM_{00}) by slightly moving CM # 2. Propagate the beam about two meters and monitor the beam. Once a TEM_{00} has been found optimize the OC, HR, lens, and crystal one more time.
 - a. Note: very slight changes in CM # 2 position will give different TEM modes.
21. After optimizing the best looking mode note the power and micrometer readings. This completes the CW alignment of the cavity.

MODELOCKING

22. Move CM # 2 in towards crystal until you get an elongated shape, like a football.
 - a. As you move the curved mirror # 2 in toward the crystal you might get weird looking modes, stars ,boxes etc.
 - b. When you have an elongated football shape you are almost at the correct position. The power should also be about 350 mW.
23. Try to modelock (ML) the laser by modulating prism # 2. When the laser modelocks tweak up the power with OC and HR.
24. Move CM # 2 in towards the crystal a little more until power decreases to 220 mW. Tweak up power again with the OC and HR.
25. The CW power should be about 250 – 350 mW with a 100 mw discrimination between the CW and ML powers.
26. Optimize the bandwidth by adjusting the prism separation.
 - a. To make the spectrum contain more blue wavelengths pull out (less glass) prism # 1 and push in (more glass) prism # 2.
 - b. If you change the prisms a couple of times tweak up the HR and OC to maximize the power and cavity alignment.
 - i. Note: Spectral chirp comes from minimum deviation of the light not prism insertion.
27. Check for self Q-switching.
 - a. Use an analog scope with a time setting of 1ms. If self Q-switching is present there will be huge oscillations on the scope

screen. Another indication that the oscillator is self Q-switching is very high power output.

28. Once you find a good prism pair insertion you can maximize the output power by adjusting the crystal; slightly move it along the rail until you get the best power.
29. If you have CW breakthrough adjust the prism insertion (for too much glass pull out one prism and push the other one in a slight bit this is an iterative process so try moving each prism both ways until the spectrum has the correct shape and is stable) and adjust CM #2 a tiny tweak. CW breakthrough can be observed with the help of a spectrometer. There will be a huge spike within the output laser spectrum.
30. Additionally, if you make huge adjustments to the prism pair separation while in the ML position you might completely misalign the cavity. To account for this bring CM # 2 back to the CW position and optimize everything (OC, HR, lens, and Crystal) check for the focuses and start mode locking procedure again. Move CM # 2 in and look for mode elongation etc.

Stretcher (KM Labs manual):

The Stretcher works on the principle of ordering the various frequencies of an ultrashort pulse, in time. The effect is the lengthening of the ultrashort pulse, and the frequencies arriving from red to blue. Figure 6 shows the conceptual layout of the pulse stretcher.

(Figure 8)

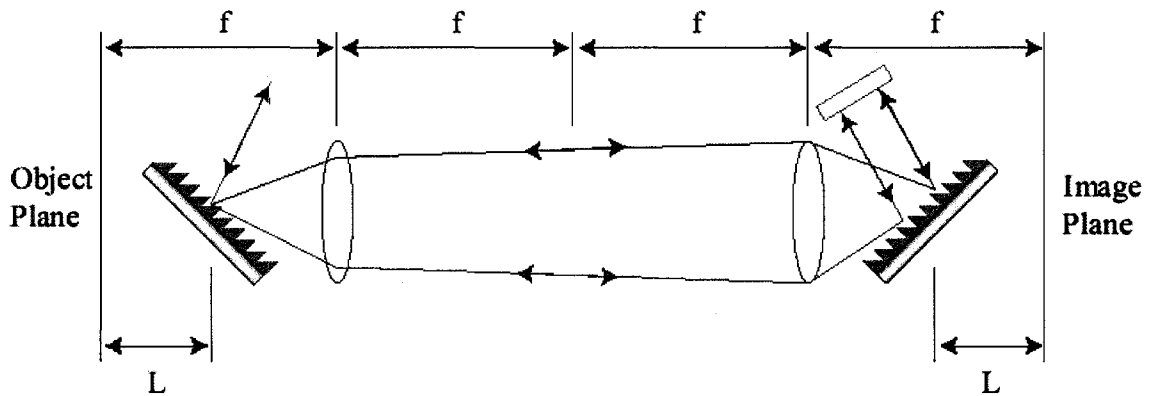


Figure 8. Schematic diagram of ultrafast pulse stretcher. L is related to the length of the stretch factor.

Where f is the focal length of the lenses (or mirrors), and L is the stretch factor length. The laser beam is directed onto a diffraction grating (object), and then imaged to another grating (image), the beam is then retro-reflected back through the system to put all the frequencies back into a single spatial mode. The gratings are then moved toward each other out of the object and image planes. This gives a differing path for the red and blue frequencies, and thus a positive chirp or stretch. If the gratings are moved away from one another, we get a negative chirp (compressor), and when they are in the object and image planes we get no chirp.

When a pulse has a “chirp”, this means that it has spectral phase other than linear. In the stretcher it is the spectral phase that gives us the stretch or chirp needed for amplification. This spectral phase can be distorted due to imperfect optics and if there is material in between the stretcher and compressor. Your KMLabs stretcher therefore contains no lenses, but mirrors to remove chromatic aberrations, and high order spectral phase distortion. Figure 7 shows the KMLabs layout of the stretcher.

(Figure 9)

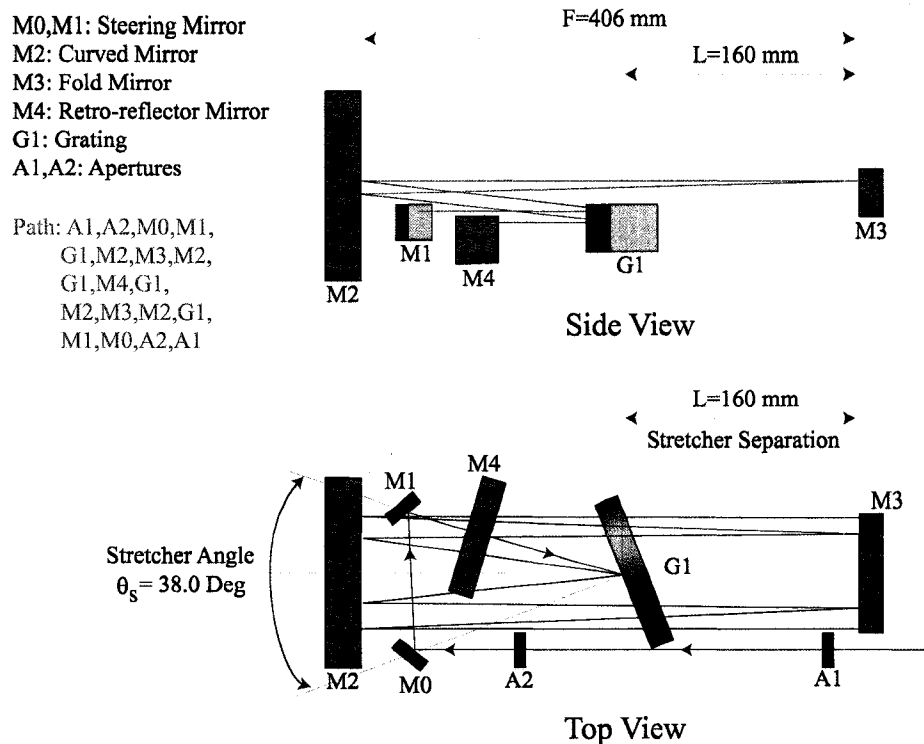


Figure 9. Diagram of KMLabs stretcher setup.

The stretcher separation is given by L , and the stretcher angle is given by θ_s . This simple design is not only easy to use, but very compact. There are 4 major components; the grating (G1), the curved imaging mirror (M2), The fold mirror (M3), and the retro-reflector mirror (M4). The path through the stretcher is quite easy to understand. The beam comes in through the apertures (A1,A2), and is directed to M1 from M0. It is then diffracted off of G1 and the light is then captured by M2. The light then goes to the fold mirror (M3), then back to M2. From there it is directed back to G1 and finally to the retro-reflector (M4). The path is then reversed and displaced slightly by M4. The beam can then be picked off after A1. It is suggested that a small vertical displacement is used to avoid spatial separation of the frequencies, or spatial chirp. The top part of Figure 7 shows how the first pass through the stretcher propagates vertically.

There are two translation stages on the KMLabs stretcher. The one for G1 is for adjusting L, or the stretch factor. The one on M3 is for proper imaging of the beam, and is pre-adjusted. The imaging can be checked by propagating the output of the stretcher over ~ 10 m and adjusting the stage to remove any distortions of the beam. The beam diameter entering the stretcher should be ≥ 2 mm. This is to allow a relatively low off-axis distortion inside the stretcher. The average power on the grating can also lead to distortion of the output due to thermal loading and should be avoided. The tested parameters for the stretcher are 400 mW, in a 2 mm beam diameter which is ~ 13 W/cm². This step-by-step procedure should get you started by helping you align the stretcher for use.

1. Set the operating angle (~ 10 deg) by moving M1 to approximately the right position. You can also put a mark on the top of the mirror to designate 10 deg. Refer to Figure 7.
2. Set the height of M1 to the same height as G1 (top to top), and lower M4 all the way down.
3. Set the height of M3 so that the middle of the mirror is at the same height as the top of G1.
4. Level the input beam to the same height as the top of M1 (minus the beam diameter), using an external mirror and M0.
5. Direct the beam to the center (horizontally) of M1, and from M1 direct the beam to the top of G1 in the center. Rotate G1 so that the center of the spectrum of the 1st order (most intense order) is at the center of M2. You

can also use the CW mode of your laser to find the center wavelength, and direct that to the center of M2.

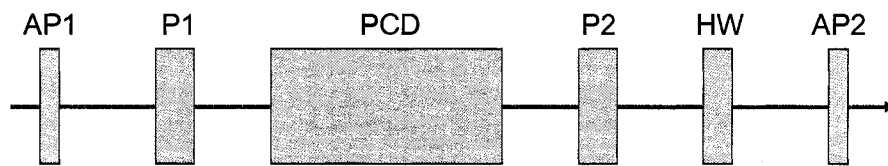
6. With the tilt adjustments on G1, adjust the spectrum until it is ~ 1 cm above M1 as it passes by.
7. Now make sure that the spectrum is level. By adjusting the tilt adjustments on G1, make sure that the blue end of the spectrum is at the same height as the red end of the spectrum, keeping the beam ~ 1 cm from the top of M1.
8. Now that the beam is level and centered ~ 1 cm from M1 on M2, direct the beam to M3, and center the spectrum using the adjustments on M2.
9. Adjust M3 to again center the spectrum back onto M2 but make sure the return beam is ~ 5 mm from the first reflection on M2, Figure 2 side view. The beam should then propagate to G1, and hit just below the incident beam.
10. Adjust M4 so that the last reflection from G1 just hits the top, making sure that the beam is not clipped on the top of M4.
11. Direct the beam from M4 back to G1, at the same spot the reflection came from. The beam should trace itself back through the entire system, and an output beam should be detected propagating the opposite direction outside the stretcher.
12. Adjust M4 so that the output beam is just under the input beam.
13. By looking at the beam on a fluorescent card adjust the translator on M3 so that the beam appears round. This adjusts the focal length of the

telescope so that there is no spatial chirp. The spatial chirp can be further reduced by use of a long path length into and out of the stretcher $\sim 1-2$ m. The beam should also be ~ 2 mm in diameter, and under 500 mW average power.

14. Pick off the lower beam for use. Note if the beam looks distorted at the output, G1 may be thermally loaded, and causing a distortion of the surface of G1. There are a few solutions; first, lower the power level by putting the stretcher after the pockels cell chain (multi-pass amplifiers), second, increase the beam diameter, which may increase spatial chirp.

Pockels cell:

Mount your Pockels cell driver (PCD) using either the holes on the bottom, or the holes on the side of the device's base plate. This option allows you to choose between an upright mounting position and a laid down position, depending upon any height/breadth restrictions. Figure 10 below for optical layout.



AP1: Aperture 1

P1: Cube Polarizer (set for P polarization)

PCD: Pockels cell driver

P2: Cube Polarizer (set for S polarization)

HW: Half-wave plate (rotates S polarization back to P)

AP2: Aperture 2

Figure 10. Optical setup of PCD. Output from the PCD has a 10 Hz repetition rate and is the seed beam for the amplification process.

Initial Setup:

You will need two polarizer; KMLabs suggests calcite glan laser polarizers from Karl Lambrecht

1. Align the beam to be sliced so that it is level, and at the correct height.
2. Ensure the beam is well collimated.
 - a. Caution: An un-collimated beam will greatly reduce the device's performance.
3. Insert the first polarizer into the beam oriented to the beams linear polarization.
4. Insert the second polarizer about 20cm away, so that it s oriented 90° from the input beam's polarization direction (Without the Pockels cell, the second polarizer should entirely extinguish the beam.)
 - a. Note: Use an escape window polarizer for high average and high peak powers.
5. With an IR viewer, a CCD camera, or a photodiode, look at the transmitted beam and adjust the second polarizer rotation to achieve complete extinction of the light.
6. Insert the PCD device into the beam, between the two polarizers. Center the beam through the apertures located on either side of the device. Make sure the adjustment screws are unobstructed for future use.
7. Again look at the transmitted beam through the second polarizer. Turn the adjustment screws on the PCD device, to again achieve complete extinction of the light.

- a. Note: A piece of lens tissue placed in front of the first polarizer, will create a dark cross after the second polarizer. Adjust the screws so that this cross is centered within the beam. This will result in maximal extinction.
8. The initial optical alignment is complete.
9. You should water cool your PCD unit when running above 1 kHz. Active cooling is not necessary at or below 1 kHz, but is strongly recommended, to prevent thermally induced drift of the temporal window.
 - a. Note: cooling water should be distilled water at a pressure of < 20 psi, and at least 2 degrees below room temperature.

Initial power up

You will need a high voltage power supply, the 15 DCV power supply, and a TTL trigger signal.

CAUTION: Do not make or break any connections when any power is applied to the PCD unit. Before you connect/disconnected any cables, verify that BOTH the PCD toggle switch is off, AND the high voltage supply is off. Read through all of the following fourteen steps before beginning with step number one.

1. Ensure that the power switch on the PCD control panel is in the “off” position.
2. Plug the 15 VDC power into the control panel.
3. Turn on the device’s toggle power switch; ensure that the red LED illuminates; then turn the device back off.
4. Ensure that the high voltage supply is set at ~6.8 kV. (This voltage must be kept below 7.5 kV. Higher voltages can damage your PCD device.)

5. Ensure that the high voltage supply is switched off.
6. Connect the high voltage cable between the high voltage supply and the PCD control panel.
7. Connect the TTL BNC connector to the device.
8. Apply the TTL signal. The TTL signal must be between 3-5 V Max, < 50 % duty cycle, and terminated at High Z ($\sim 1 \text{ M}\Omega$).
9. Place a fast photodiode ($\sim 1 \text{ ns}$ response) at the output of the second polarizer, and verify that no pulses are being transmitted.
 - a. Note: A half-waveplate, placed between the first polarizer and the PCD device, will defeat the PCD. The beam will then pass through the second polarizer, allowing you to align the photodiode with the PCD powered off.
10. Turn the PCD toggle switch on. The red LED should illuminate.
11. Turn on the high voltage supply.
12. Look for the picked pulse using the photodiode.
13. Adjust the TTL timing signal to select a single pulse.
 - a. Note: The PCD device experiences a temporal drift until it thermalized. The characteristic thermalization time is approximately 20 minutes.
14. If multiple pulses appear no matter what TTL delay is set, adjust the window width potentiometer located on the end plate of the PCD (small trim pot). Also adjust this if your application requires a larger window.
 - a. Note: The TTL signal must be locked to the pulse train being picked, or the pulse through the PCD device will vary wildly.

Daily Power-up/ Power-down

CAUTION: Do not make or break any connections when any power is applied to the PCD unit. Before you connect/disconnect any cables, verify that BOTH the PCD toggle switch is off, AND the high voltage supply is off.

This section assumes that all cables are attached, and the system has been previously powered up. If either assumption is untrue, go to previous two sections.

You may apply the laser at any step during power-up.

1. Ensure all cables are connected.
2. Turn on the cooling water.
3. Apply the TTL signal to the BNC timing input.
4. Turn on the toggle switch on the PCD control panel.
5. Ensure the high voltage is set will below 7.5 kV (preferably at ~6.8 kV).
6. Turn on the high voltage power supply.
7. Allow the PCD device to warm up for approximately 20 minutes.
8. Observe the photodiode output to ensure that a single, full pulse is passing through the PCD.
9. If necessary, adjusting the timing input and/or potentiometer to select a single pulse.

Daily Power-down

1. Block the input light.
2. Turn off the high voltage supply.
3. Turn off the PCD control panel toggle switch.
4. Turn off the cooling water. (No delay-time is necessary.)
5. Turn off photodiode is applicable.

Amplifier:

For proper alignment of the amplifier cavity it is imperative that the nine passes through the cavity are parallel. An alignment card will help to ensure this occurs.

alignment card:

1. The alignment card is 13.5 cm by 5 cm.
2. Draw a horizontal line across the card at a height of 12.7 cm. This corresponds to the height of the beam through the cavity.
3. Draw nine vertical lines. The fifth line should be at the center of the card (2.5 cm) and the lines should be separated by 3 mm. These lines correspond to the passes through the cavity.

Cavity alignment: (See figure 5 in the overview.)

This alignment is iterative. Mirror M_1 is on a micrometer stage. Start the alignment with M_1 at a micrometer reading of 15 μm . After each iteration, move M_1 closer to the cavity crystal. Increase the micrometer reading about 50 μm for the first few iterations. When the cavity is becoming properly aligned more passes will be observed. After the seed beam passes through the cavity twice decrease M_1 's micrometer movement to 10-15 μm per iteration.

The 10 Hz, 800 nm seed light enters the amplifier cavity via mirrors M_0 and M_1 . The beam should be centered on M_0 but on the far left of M_1 .

1. Ensure the input beam from the pockels cell is level. Using the alignment card check the height between M_1 and M_2 . If the height is not level correct it using M_0 and M_1 .
2. Direct the input beam to M_2 .
3. Using the alignment card, place the edge of the card on the outside edge of M_2 . Using M_1 , direct the beam to the first vertical line on the card. This is pass 1.
4. Using M_2 , direct the beam through the crystal to M_3 . Place the alignment card on the edge of M_3 . Use M_2 to adjust the beam so that it is the proper height and hits the first vertical line on the alignment card.
5. Ensure the height of the beam is correct at M_4 . Use M_3 to direct the beam to the right side of M_4 . The first pass should hit M_4 1-2 mm from its right most edge.
6. Adjust M_4 so that the first pass through the cavity hits the second vertical line on the alignment card at the proper height. Using the alignment card, one should look at the incoming and first pass through the cavity at the same time. Each pass should be centered on its respective vertical line.
7. This concludes one iteration.
8. Move M_1 closer to the crystal using the micrometer stage. At the beginning of the alignment procedure move M_1 about $50\mu\text{m}$ per iteration. As soon as two passes make it through the cavity decrease the amount per iteration M_1 moves closer to the crystal. The alignment tends to 'pop' into place. For example after an iteration you will have three passes through propagating through the cavity. The next iteration could give you eight passes.
9. Repeat steps 2-8 until 8 evenly spaced passes are going through the crystal.

10. Insert the mask. The mask is made from a simple thin piece of Al 5 cm x 2 cm. Nine 2 mm holes spaced 3mm apart, from center to center, are drilled through the mask. The main purpose of the mask is to reduce the amplified stimulated emission (ASE) in the amplifier ring.
11. Using M_5 and M_6 direct the final pass out of the cavity.
12. M_5 and M_6 are also used to align the beam through the telescope/spatial filter.

Crystal Replacement:

When the crystal needs replacing, first remove it from the large copper holding device. The crystal is enclosed in another copper sleeve. Carefully loosen (2 screws) the sleeve and the crystal will fall out. When working with the crystal wear gloves. It is not good to get oil on the crystal face.

1. Place new crystal into copper sleeve. There is a proper direction due to the cut of the crystal. Do not tighten copper sleeve too much because it might stress the crystal.
2. Place crystal within its sleeve back into large copper holding device.
3. The crystal must be level in the holding device and at a 64 degree angle to the incoming beam.
 - a. The crystal mount is on a rotation stage which allows one to measure the angle to the incoming beam.
 - b. Rotate the stage so that the incoming and retro-reflected beam overlap at M_2 . This is the 0 degree angle.
 - c. Adjust the crystal sleeve within the large copper holder to make sure the incoming and reflected beam are the same height at M_2 .

This ensures the crystal is level. There are two tapped holes in which Teflon screws can be mounted. These two screws make it easier to adjust the crystal sleeve.

- d. Rotate the stage back 64 degrees. Make sure to lock the stage.
- e. The crystal should now be level and at the proper angle.

Compressor (KM Labs manual):

Compression of the pulses is accomplished by reversing the process of stretching. This is typically done with a simple grating pair. The grating pair imparts a negative chirp to the pulse. The important function of a compressor, other than compressing the pulses, is that it must be high in efficiency. It makes no sense to amplify your pulses (expensive) and then throw away the energy in your compressor. Here at KMLabs we have developed a compressor design that maximizes the efficiency of the compressor to ~ 70 %, where typical compressor designs can only achieve ~ 50 %. The layout of the KMLabs compressor is simple, and diagramed in Figure 9.

(Figure 11)

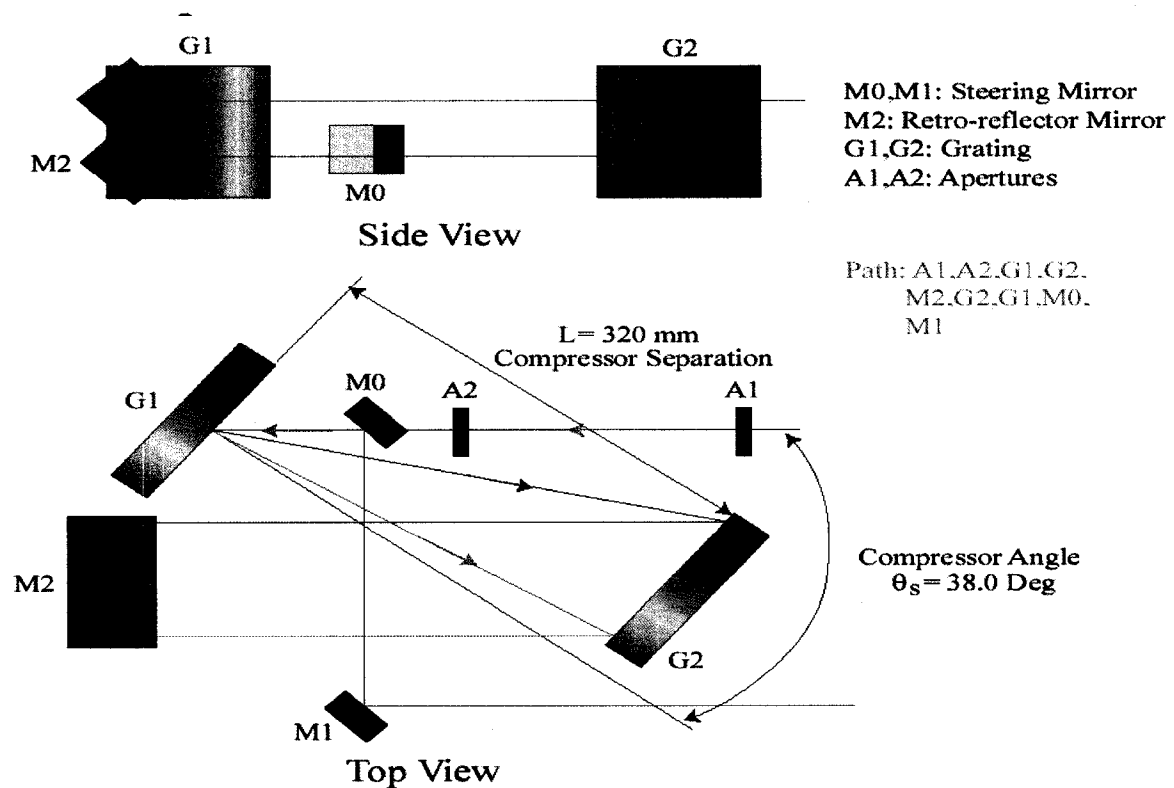


Figure 11. Compressor

The compressor length is given by L , and the angle is given by θ_s . The compressor is very simple to align. First the beam goes through apertures A1, and A2. It is then diffracted off of G1 and then off of G2 where the frequencies are collimated. The beam then is retro-reflected by M2 and periscoped down to hit a lower spot on G2. The beam is then reassembled by G1, and M0 extracts the beam from the compressor, while M1 sends it out. The vertical displacement of the beam can be seen in the upper part of Figure 9. It is suggested that the average power fluence on the Gratings be below 7 W/cm^2 to avoid thermal loading, and subsequent beam distortion.

This step-by-step procedure should get you started by helping you align the compressor for use.

1. First get the beam level and straight.
2. Adjust the apertures A1 and A2, so that the beam goes through the center of each.
3. Open apertures and reflect beam off of G1. The brightest order (1st) is the beam used.
4. Level beam with tilt adjustments. Make sure that the blue side of the spectrum is at the same height as the red side of the spectrum.
5. Adjust angle, ~10 deg minimum. Or 38 degrees on rotation stage indicator. (28 deg littrow angle plus 10 deg incident angle.)
6. Adjust G2 translation so spectrum fits in the middle of G2.
7. Adjust G2 tilt to level beam and spectrum as in step 4. Set G2 rotation stage to same number as G1.
8. Adjust M2 so beam is not clipped upon entry. Adjust horizontal M2 adjustment so that the beam reflects back to G1, under the input beam.
9. Adjust height of M0, so that output beam can be extracted, and send the beam to M1 for output.

TOPAS:

The final part of this appendix describes the TOPAS alignment. The first few pages highlight the day-by-day procedures we use to align the TOPAS for 226 nm light. The remainder of this section consists of the manual obtained from Light Conversion/ Coherent Lasers. If read in full the manual is actually very helpful.

Day-by-day Alignment of TOPAS for 226 nm light:

1. Ensure inputs, to TOPAS and TOPAS-UV, are blocked; this is easily done with two business cards.
2. Ensure the 800 nm light is passing through the center of the iris before the compressor and after the periscope for the TOPAS.
3. Measure the 800 nm light energy directly after the compressor it should be about 1.4 mJ with a standard deviation of $\sim 60 \mu\text{J}$
4. Remove the business card blocking the input to the TOPAS.
5. Observe the output directly after TOPAS with settings for 226 nm light.
 - a. Output beam should have an oval shape and be red in color.
6. If you observe the red light use the mirror closest to the TOPAS to optimize the intensity and shape. (If you do not observe red light, even after tweaking the mirror a bit, consult with the TOPAS manual. It is likely you will have to open the TOPAS and realign the pinholes within. This procedure is well described in the manual.)
 - a. At this point you can use a 60° prism to separate out the different wavelengths of light. We usually monitor the light after the third crystal box.
 - b. Measure the energy of the 315 nm light after the prism. It should be around 15-20 μJ .
 - c. Optimize energy and beam shape by slightly tweaking the two input mirrors to the TOPAS.
7. Once the 315 nm light is optimized, look for the 226 nm light. The prism must still be in place to observe the separated 226 nm light.

- a. First remove the second business card blocking the 800 nm light to the TOPAS-UV station.
- b. Use a good fluorescing business card to observe the 226 nm light.
 - i. The 226 nm light is seen best with the lights off.
 - ii. If you do not observe 226 nm light, first adjust the UV delay. With the UV delay you can usually observe some 226 nm light.
 - iii. Once the light is detected, optimize the intensity and shape by overlapping the 800 nm light from the TOPAS-UV with the 315 nm light from the TOPAS.
- c. Slight adjustments to the amplifier delay can also increase the 226 nm energy.
- d. 226 nm light output should be on average 3 μJ , but this is highly dependent upon the 800 nm pump power and stability.

Note: The stability of the 800 nm pulse is imperative. Monitor the amplified pulse before the compressor with a photodiode. Ensure only one pulse is being amplified. Adjust the pockel cell timing to select a single stable pulse if multiple pulses are observed.

(Coherent manual)

1. DAY-BY-DAY ALIGNMENT OF TOPAS

Below you will find description of the procedures that you should perform when starting TOPAS operation.

1. Warm-up the TOPAS pump laser and perform day-by-day checking/adjustment procedures recommended by the laser manufacturer. Verify the TOPAS pump

- energy is set to the specified/ usual value.
2. Start the TOPAS software WINTOPAS and tune the TOPAS to a checkpoint wavelength(s). Verify the TOPAS output energy at that (those) wavelength(s) corresponds to the specified/ usual value.
 3. If the TOPAS output energy at the checkpoint wavelength(s) is lower than the specified/usual values, check the Signal+Idler (S+I) energy with no mixing crystals involved and ensures it corresponds to the specified/ usual values.
 4. If S+I output is OK, reset a Mixer(s), which produced lower output. Measure a new Mixer offset if needed.
 5. If S+I output is low, try to restore the output energy by fine adjustments of the pump beam steering mirror closest to the TOPAS input.
 6. If S+I output is low after the fine adjustment of the input mirror, reset the TOPAS motors.
 7. If all the above do not help to get the specified/ usual TOPAS output, proceed to the TOPAS diagnostics and realignment section (Part III), which will help you detect and fix the problem. We recommend reading Part II before starting with Part III.

Be careful when aligning the pump input direction. Any pump beam should fit the aperture of the nonlinear crystal. If the pump beam hits the crystal holder a deposition of metal particles will occur on the crystal surface and eventually cause damage to the crystal.

2. TOPAS DESCRIPTION

In this chapter we present the general principles of the TOPAS design and will try

to give a detailed feeling to the reader about what's going on at each stage of parametric amplification in the TOPAS. An alignment procedure will follow in the next part of manual.

2.1 Principles of TOPAS design

TOPAS configuration.

TOPAS employs one stage of generation of superfluorescence (SFL) and four light amplification stages arranged in a single BBO. Generator of SFL (first pass through the nonlinear crystal) serves as a seeder emitting broad-banded superfluorescence. Preamplifiers (second and fourth passes through the nonlinear crystal) shape the beam acting as a small amplifying aperture placed in the far field of the seeder. In the third pass through nonlinear crystal the amplification usually is negligible. The last amplification stage (fifth pass through nonlinear crystal), which usually is pumped by the bulk of the available pump beam energy, boosts the energy of the parametric pulse. With a pump beam of high spatial coherence and carefully adjusted pump beam size in the pre-amplification stages, the *TOPAS* emits a beam with a divergence close to the diffraction limit. The *TOPAS* configuration has the advantage that dielectric mirrors of relatively narrow-bandwidth and low dispersion are used to direct the pump beams. In the beam path of the signal pulse metal-coated mirrors are used. In this way, full tuning range can be covered without replacing the optics.

Wavelength Tuning

Wavelength tuning in the TOPAS is performed by nonlinear crystal rotation in phase matching plane. The changing of crystal angles raises problems related to beam/pulse displacement. In the *TOPAS* these problems are solved in part by using a quartz

compensation plate that is tilted along with the crystal, and in part by time delay units that are controlled by the stepper motor.

Nonlinear Crystals

A BBO crystal with pump wavelengths ranging from near UV to near IR is operated in a type II phase matching configuration. The maximum available signal frequency can be defined as $\nu_s = \nu_p - \nu_{abs}$, where ν_s is the maximum signal frequency, ν_p is pump frequency and ν_{abs} is the IR absorption edge that equals approximately to 3300 cm^{-1} . The type II phase matching has a serious advantage of comparatively narrow gain bandwidth and allows for generation of $<1 \text{ ps}$ pulses with time/bandwidth product well below unity. The bandwidth does not increase at the degeneracy which is the case for type I phase matching since full degeneracy does not exist. For type II phase matching the polarization of signal and idler waves are orthogonal even if frequencies are equal. This also gives a possibility to separate signal and idler waves using polarizers.

Grating Frequency Selection

In order to reduce the spectral width and to stabilize its shape a diffraction grating is installed between the pre-amplification stages. When tuning the *TOPAS* the change of grating angles is controlled by the stepper motor that is synchronized with the nonlinear crystal rotation.

When the *TOPAS* is pumped by femtosecond pulses the spectrum of parametric pulses is formed by a nonlinear amplification process itself. Nevertheless, the employment of a grating makes the operation of the *TOPAS* more reliable and simplifies the procedures of femtosecond *TOPAS* calibration.

Crystal Protection and Control Electronics

In order to protect nonlinear crystals against atmosphere humidity the AR/protective coatings optimized for pump wavelength are used in combination with permanent crystal heating. Temperature controller keeps the crystal temperature at about 40°C. The temperature controller is assembled on a board that interfaces the stepper motors with IBM compatible PC via a parallel printer adapter. One board can control up to 6 stepper motors, and four boards can work in parallel.

Pump Laser Options: Power Levels, Wavelengths, Pulsewidths

The TOPAS can be pumped with different kinds of lasers whose wavelength can range from UV up to near infrared. Obviously, a short wavelength pump appears to be more attractive since a larger wavelength range can be covered in a basic TOPAS unit. However, with femtosecond pulses group velocity mismatch becomes relevant. It increases with shorter pump wavelength thus limiting application of UV pump sources. So far, the operation of *TOPAS* has been tested when pumped with 0.2 - 30 ps pulses of SH of Nd laser, 7 - 30 ps pulses of TH of Nd:YAG laser, 0.02 - 2 ps Ti:Sapphire laser fundamental pulses, 0.5 - 2 ps pulses of SH of Ti:Sapphire laser, femtosecond dye laser pulses of 0.6 μm . In all the cases energy conversion into parametric radiation of ~20% and more were achieved. An important feature of the *TOPAS* design is that it can be matched to pump sources with peak power ranging over orders of magnitude. The minimum 150 fs pump pulse energy ensuring > 10% parametric conversion is around 100 μJ . No limitations for pulse repetition rate up to 10 kHz were observed.

Additional Options for Frequency Conversion

The output of *TOPAS* can be frequency doubled and quadrupled in the same way as output of a conventional laser. Moreover, the presence of three wavelengths at the

output offers extra possibilities. First, both signal and idler waves or their harmonics can be mixed with the rest of the pump for sum frequency generation thus shifting the tunable radiation towards blue. Therefore, using optional nonlinear frequency converters one can obtain the tunable radiation down to ~ 190 nm. Second, difference frequency can be produced mixing signal and idler waves. This process transfers the wavelength of tunable radiation to mid-IR covering 2.4 –20 μm wavelength range. We should note, that in the case of Ti:Sapphire laser, the use of difference frequency generation from the *TOPAS* output allows one to overcome the problem of one and/or two photon absorption of the IR transparent crystals.

2.2 First, second and third passes: formation of the seed

The first three passes in TOPAS are used for the generation and pre-amplification of the stable seed pulse for subsequent amplification stages

In Fig. 10 you can see the schematics of the first three passes through nonlinear crystal in TOPAS.

(Figure 12)

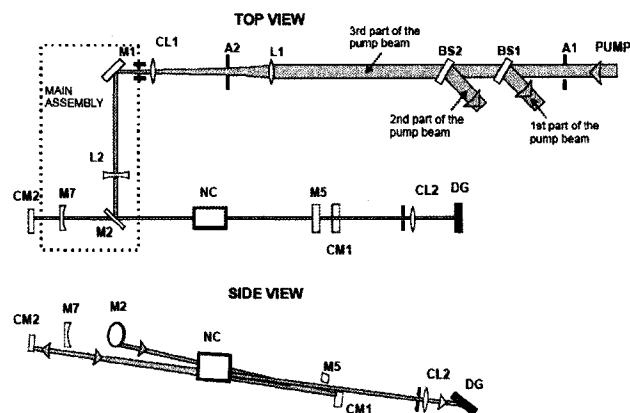


Figure 12. Top view and side view layout of the first, second and third passes beam paths inside the TOPAS.

The incoming pump beam is split into three components by means of beam splitters (BS1 and BS2) upon entering the TOPAS. The first two are going to be used for the fourth and fifth passes (seed amplification). The third component is the light that passes through BS1 and BS2 to be reflected by the mirrors M1 and M2 in the main assembly towards the nonlinear crystal (NC) and is referred as the first pump that generates parametric superfluorescence (SFL) signal (a seed) inside the TOPAS. This latter component of the light will do in total three passes in the NC, which they will be called respectively the first, second and third passes. 1-3rd passes use both spherical (L1, L2) and cylindrical (CL1, CL2, CM1, CM2) optics to shape the beam, thus it is normal that the beams have no spherical symmetry in the 1-3rd passes.

1. The first pass goes from the lower edge of M2 to the upper part of CM1. That first pump pulse through the NC is used for producing the SFL. The optimum pump intensity for producing of SFL is set at the installation adjusting aperture A size and cylindrical telescope consisting of lenses L1, L2 and CL1. (Typical shape of pump beam with SFL, seen as sum-frequencies: pump plus signal, pump plus idler, SH of signal and so on, is presented in **Photo 1**).

The second pass is the backward reflection from CM1, through the NC, to CM2. This second pass amplifies the collinear components of SFL produced in the first pass. TOPAS pumped by ~800nm light generates IR wavelengths (~1.1-1.6 μm for signal and ~1.6-2.6 μm for idler waves), which are not visible to the human eye. However some IR wavelengths get mixed with the pump in the same NC and produce a weak visible output. Thus one can see a visible beam (e.g. green when signal is set to ~ 1500 nm or reddish when signal is set to ~ 1200 nm) overlapped with the pump starting from the second pass

(SFL after the first pass it is usually too weak to be seen). The visible light follows approximately the same path as the true signal and idler beams and can be used as guidance in the TOPAS alignment and as an indication of parametric conversion.



You can see the pattern of light corresponding to amplified SFL placing the card behind the main assembly in front of CM2 (Photo 2).

Note. You should distinguish the visible light caused by parametric light generation from the light that appears due to the supercontinuum generation. Supercontinuum generation starts at pump intensities slightly higher than compared to the threshold for SFL and emerges as a white light or colored center-symmetric rings at the output of crystal.

(Photo 3).

Caution! Remember that threshold of supercontinuum generation and optical damage of the crystal is rather close. Don't work in the condition of supercontinuum generation for a long time.

The third pass is the reflection from CM2 through the NC to the diffraction grating (DG). In the third pass the beam of amplified SFL goes just above CM1 and hits the center of DG. The beams of the first three passes do not overlap in space but are in the same vertical plane.

Notice that the beam after the third pass through the NC goes through the assembly of slit and cylindrical lens CL2. The slit transmits only the central portion of beam and acts as a cursor for proper alignment of the TOPAS. The beam is then collimated by CL2 and hits the center (axis of rotation) of the DG.



You can see pattern of the preamplified parametric light by placing the card behind and in front of the slit and CL2 assembly. . (Photo 4 and Photo 5 correspondingly).

2.3 Fourth pass: pre-amplification of the seed beam.

The fourth pass in TOPAS is employed for the formation of stable, nearly transformlimited and low diffraction seed for the power amplifier of TOPAS.

After three passes we basically have relatively weak, broad-band parametric radiation with significant divergence in the vertical plane. The amplification in the fourth pass through the nonlinear crystal shapes the parametric signal acting as a small amplifying aperture placed in the far field of the seeder. The schematic of the seed pulse pre-amplification in the fourth pass is presented in Fig. 11.

(Figure 13)

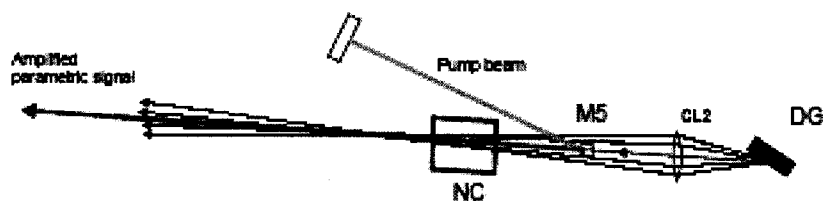


Figure 13. Scheme showing the principle of the pre-amplification in the fourth pass.

The seed beam is spread in spectrum in plane of the NC by means of DG and CL2. The fresh portion of pump is delivered to NC at the fourth pass using a thin mirror M5. The TOPAS is aligned in a way that the parametric signal pulse is overlapped both in space

and in time with the pump pulse. Since pump beam waist on the crystal is significantly reduced by a telescope, only part of the spectrum of the diffracted seed beam will be amplified. As a result, the amplified parametric radiation has a diffraction that is close that of the pump beam. Notice that employment of the grating serves several purposes: i) to narrow the amplified signal spectrum; ii) to separate signal, idler, and pump in space; and iii) to make wavelength tuning more precise in the wavelength range close to NC absorption band.

The grating rotation stage is driven by a stepper motor. When tuning the *TOPAS* the appropriate grating angle is set by the *TOPAS* control software. The diffraction grating is operated in autocollimation mode. It should be noted that due to the limited range of the rotation stage different grating diffraction orders are used in order to cover all of the tuning range.

In picosecond operation mode the diffraction grating is operated at high diffraction orders for maximum spectral resolution and high diffraction efficiency. Incidence angle usually is in between 70 and 40 deg. In femtosecond mode the grating is operated at incident angles between 10 and 30 deg. At these angles the grating dispersion is low and diffraction efficiency is high enough.

The arrangement of beams in fourth pass through the nonlinear crystal is presented in Fig. 12.

(Figure 14)

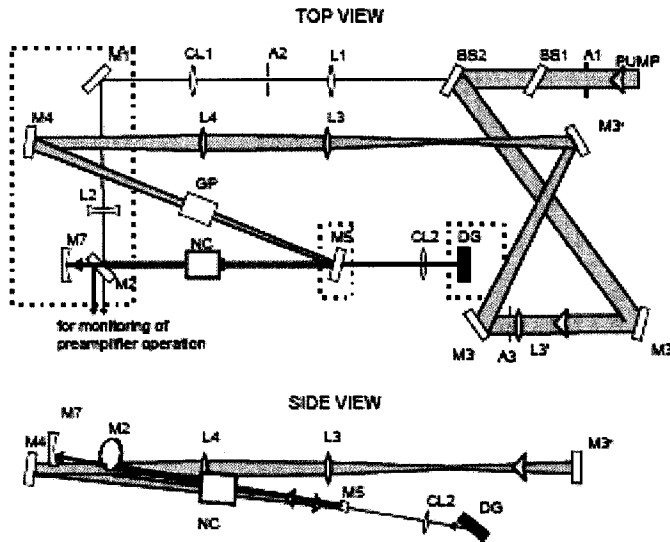


Figure 14. Top and side view layout of the light path of the fourth pass inside the TOPAS.

The beam reflected from BS2 is used as a pump for signal amplification in the fourth pass through the NC. It passes the zoom telescope, consisting of lenses L3', L3 and L4, and after reflecting from M4 and M5 it enters the NC. After the telescope the pump beam focuses and, usually, has the beam waist at the plane of NC. The beam waist radius is optimized for the maximum signal amplification rate: the pump intensity should be just below the threshold of parametric superfluorescence and/or continuum generation.

Before entering the NC the pump beam then passes a fused silica plate (GP) which compensates for the lateral displacement of the beams introduced when crystal changed its angle in the first three passes. This ensures that the pump beam hits the mirror M5 always at the same spot as the seed beam.

Then, M5 reflects the pump towards the NC. The seed pulse (signal) reflected from the DG passes M5 to meet the pump pulse at the reflecting surface of M5. The DG is mounted on a delay stage and one could adjust the temporal delay between the seed and pump pulses for their overlapping in time. This is the DELAY 1 adjustment. The

optimum delay is set during installation of TOPAS but could need adjustment when the 4th pass alignment is changed.

In the NC only almost collinear spectral components of the seed diffracted by DG are amplified due to small pump beam size. When tuning the TOPAS the DG is rotated in accordance with the NC crystal angle change. In this way the spatial overlap of the appropriate spectral components with pump beam is ensured in all tuning range.

Then, the pre-amplified seed beam goes through M2 (dielectric mirror M2 is of high reflectivity only for ~ 800 nm radiation at 45° incidence). The concave Al mirror M7 directs the amplified seed beam backwards slightly above the NC.



You can monitor the preamplifier operation by placing a paper sheet at the side edge of the main assembly (see “for monitoring of preamplifier operation” in Fig. 12). Two bright visible spots (partial beam reflection from the substrate of M2) can be seen on the paper sheet. The intensity of the spots should significantly change if either of pump or seed (1-3rd passes) is blocked.

2.4 Fifth pass: final amplification.

At this point, we have a seed beam that has been pre-amplified in the fourth pass through the NC. This seed radiation is coherent to great extent both in space and time and will be amplified to its final power level in the 5th pass by using the bulk of the incoming pump beam. In order to have high energy conversion efficiency at the last pass through the NC the seed and fresh pump beams are matched in size. Obviously, the seed and pump pulses should overlap both in time and space.

The schematic of the final amplification stage is presented in Fig. 13.

(Figure 15)

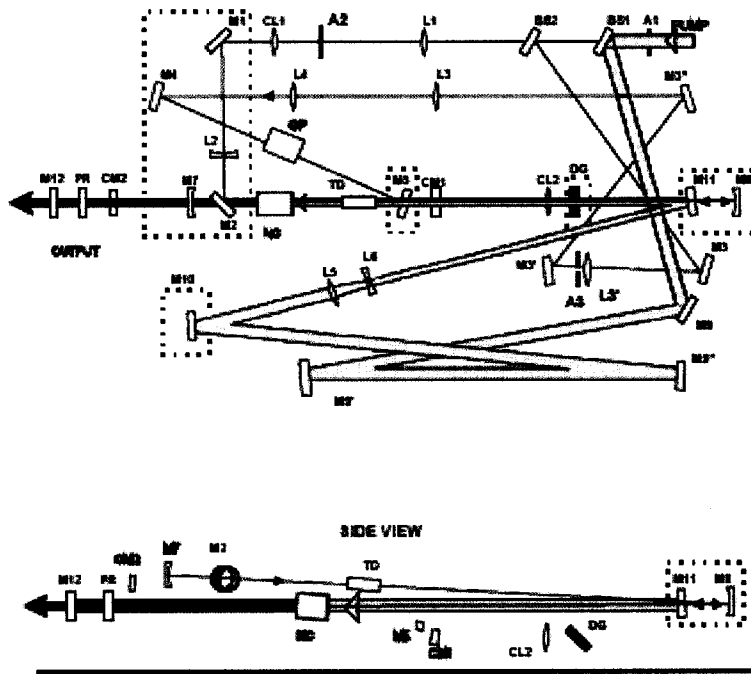


Figure 15. Top and side view layout of the light path of the fifth pass inside the TOPAS.

The seed beam reflected from M7 comes above the NC and passes the time delay crystal (TD). The TD crystal separates the signal and idler pulses in time. A bright visible spot is seen in front of the TD as an indication of effective seed pre-amplification in the 4th pass (**Photo 6**).

The spot should disappear if either the 4th pass pump or the seed (1-3rd passes) is blocked (**Photo 7** and **Photo 8**). The mirrors M7 and M8 form a telescope that expands and collimates the seed beam. M8 directs the seed beam to the NC for final amplification.

The main part of the pump reflected by BS1 is transported to the NC by a series of high reflecting mirrors (M9, M9', M9'', M10, M11). The mirror M10 is installed on a computer controlled mechanical delay line (DELAY 2) allowing for fine time delay

adjustments when tuning TOPAS. The telescope consisting of lenses L5 and L6 allows for setting the optimum pump intensity on the nonlinear crystal: the pump intensity should be high enough to saturate amplification, but at the same time it should be below the threshold of SFL and supercontinuum generation.

The TOPAS is aligned such that the 5th pass pump beam overlaps the parametric signal at M11, in the nonlinear crystal, and in the far field at the output of *TOPAS*. In other words a collinear amplification configuration is used in the TOPAS. Notice that the 5th beam pass lays in same or is parallel with the plane containing the beams of the 1st - 4th passes.

In the final amplification stage the parametric pulses are amplified from the level of several microjoules to the specified output energy and transmitted through mirror M12. M12 blocks the pump, but allows the parametric pulses to come out of the TOPAS.

In particular TOPAS models, on customer request, the polarization rotator (Berec compensator) is installed at the output of TOPAS. This unit enables the user to set the vertical polarization for both signal and idler pulses.

Once installed the TOPAS, usually, needs no adjustment of its element angles or positions. Crystal rotation (tuning), grating rotation stages, and the delay line are moved by stepper motors controlled from the computer. The TOPAS software drives the stepper motors with reference to data in the tuning curve file. The tuning range of the TOPAS output can be significantly broadened by means of optional frequency converters (harmonic generators, sum and difference frequency generators) enabling the user to cover the wavelength range from deep UV to mid-IR.

If the pump characteristics are as specified above, the failure of the TOPAS's

normal operation could be due to several reasons:

- The input pump beam direction is changed
- The calibration of the stepper motor(s) is lost
- There is optical damage to a certain optical element.

In the following chapters you will be presented with detailed instruction for the TOPAS diagnostics and alignment procedures that will help you to restore the specified TOPAS operation.

3. TOPAS DIAGNOSTICS, REALIGNMENT AND RECALIBRATION

The femto/pico second pulses of several different wavelengths can be used as a pump for different TOPAS models. The basic principles of TOPAS diagnostics and alignments are the same, however the appearance of the beam colors are different.

When the *fundamental of Ti: sapphire laser is used as a pump* its radiation is almost under the range of human vision, the parametric radiation is in the infrared. Therefore, use the visible light that appears due to non-synchronous generation second harmonic and sum frequency in nonlinear crystal as a guide for the axial components of superfluorescence and amplified parametric radiation. The pump beam direction can be traced by observing the signal of the nonsynchronous second harmonic of the pump (blue light spots). The dielectric mirrors are well transparent for a light in visible.

When the *TOPAS is pumped by the SH of a neodymium laser or the SH of a Ti:Sapphire laser* a pump beam is well visible along the entire beam path in the *TOPAS*. In order to visualize the beam path of the parametric radiation in case of pumping by the SH of Nd lasers it is advisable to perform diagnostics and alignment procedures when the *TOPAS* is tuned for generation at wavelengths 650 -700 nm. If the SH of the Ti:Sapphire

is used as a pump tune the *TOPAS* to the 530 -570 nm wavelength range.

When the *TOPAS* is *pumped by the third harmonic of a neodymium laser* the pump beam could be monitored using the fluorescence of white paper illuminated by the UV pump radiation. The signal parametric radiation is visible in all tuning range.

The following subchapters presents the diagnostic and alignment procedures for *TOPAS* models pumped by the fundamental of a Ti:Sapphire lasers ($\lambda \sim 800$ nm).

THE PROCEDURE OF TOPAS DIAGNOSTICS AND REALIGNMENT CONTAINS TWO MAJOR STEPS. THE FIRST STEP IS A VERIFICATION PROCEDURE (Chapters 3.1-3.3). NO OPTICAL ELEMENTS SHOULD BE TOUCHED. THIS IS ONLY A DIAGNOSTIC PROCEDURE. SOME EXTERNAL MIRRORS MAY BE TWEAKED, BUT NOTHING INSIDE THE TOPAS SHOULD BE TOUCHED.

3.1 Diagnostics: pump beam and pulse parameters

If possible, check the contrast ratio of the pump pulse. Check that the pump laser performance and the *TOPAS* pump beam parameters such as energy, pulse duration, and beam quality correspond to the specified values. The laser energy should be approx. **1.4 mJ, pulse at 10Hz, 30 fs time duration**, beam profile _____.

using a fast photodiode. The contrast ratio should be $> 1/100$ (or 100, depending on convention). Pump polarization for *TOPAS* must be horizontal.

3.2 Diagnostics: TOPAS optical elements

If the pump is OK, check the *TOPAS* optical elements (especially the main BBO crystal) for possible damage and deposited dust.

3.3 Diagnostics: TOPAS alignment

If pump beam and the optics of *TOPAS* are OK, check the *TOPAS* alignment:

1. Reset all *TOPAS* motors if not done yet (unnecessary reset is not recommended).

Set the signal WL to ~ 1300 nm.

2. (PUMP FOR ALL PASSES BLOCKED) Check that the input beam is centered on the input aperture A1.

3. (PUMP FOR 4TH, 5TH PASSES BLOCKED) Check that the beams after the first and third passes are in one vertical plane by placing a card before CM1 (see Fig. 14).

When scanning in the vertical with the card, you should see the first and third passes alternatively. The pattern of parametric light after second pass can be seen placing the card in front of CM2 (**Photo 2**).

(**Figure 16**)

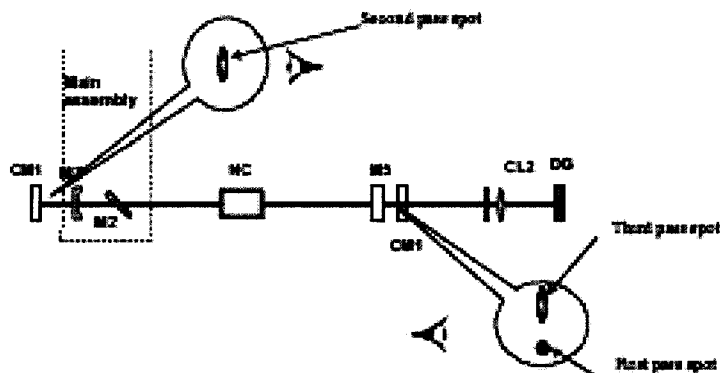


Figure 16. Views of the beam spot configuration on the card when checking for the first, second, third and fourth passes.

4. (PUMP FOR 4TH, 5TH PASSES BLOCKED) Check that you get a parametric SFL signal after the third pass (one should see some visible light overlapped with the 800 nm light). Look on a white card placed before CL2 (**Photo 5**). SFL (VIS light) must be strong and stable. Notice that SFL is more divergent in vertical plane (In **Photo 2** one can see beam without significant clipping).

5. (PUMP FOR 4TH, 5TH PASSES BLOCKED) Check that the third pass beam is just above of the first pass beam and its central most intense part goes right through the horizontal slit of the CL2 holder (**Photo 4**).

(**Figure 17**)

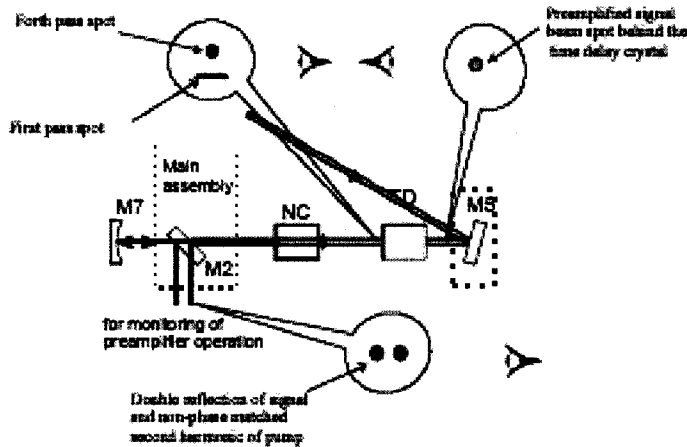


Figure 17. Views of the beam spot configurations on the card when checking for the preamplification at the fourth pass.

6. (5TH PASS PUMP BLOCKED) Check that the spots of the pump beam for the fourth and the first passes are in the same vertical plane by placing a card before the NC (see Fig. 15). Place the card at the maximum possible distance from the NC in order to prevent depositions on the crystal face in case card burns.

7. (5TH PASS PUMP BLOCKED) Check that you get amplification in the fourth pass. You should see two bright visible blue (non-phase matched SH of pump) and green-yellow (non-phase matched sum-frequency of pump and SFL) spots going away from the main assembly towards M10 (**Photo 7**). Likewise, you could see an intense visible beam (from signal & idler sum frequency with the pump) when placing the card behind the TD crystal (**Photo 6**).

8. (5TH PASS PUMP BLOCKED) Check that the pre-amplified parametric beam after reflection from M8 goes through the NC with minimum clipping by placing the card at the output of TOPAS.

9. (ALL PUMPS UNBLOCKED) Placing the card at the output of TOPAS check that the pump beam for 5th pass goes through the NC with minimum clipping.

10. (ALL PUMPS UNBLOCKED) Verify that the pump and the seed beam are collinear in the fifth pass monitoring the patterns of parametric light and pump at the distance of 5- 10 m from the output of TOPAS. These patterns should overlap. Also, check that the spectral components of parametric light are not separated in space.

Try to restore the alignment by tweaking just the external beam routing mirrors. If that is not possible, refer to the next section that describes more detailed realignment procedure of the TOPAS.

Be careful when aligning pump input direction. Any pump beam should fit the aperture of nonlinear crystal. If pump hits the crystal holder a deposition of metal particles on the crystal surface eventually will cause damage to the crystal.

THE SECOND MAJOR STEP IS THE REALIGNMENT PROCEDURE ITSELF (Chapters 3.4-3.6). IN THAT CASE, OPTICS INSIDE WILL NEED TO BE ADJUSTED AND THEREFORE, AFTER REALIGNMENT PROBABLY A RECALIBRATION OF THE TOPAS SHOULD BE PERFORMED. THIS PROCEDURE IS FOR TRAINED PERSONS ONLY AND REQUIRES A LOT OF ATTENTION AND UNDERSTANDING.

3.4 Realignment: First, Second and Third passes: seed signal

The goal is to achieve a strong and stable amplified SFL after three passes in the NC

by accurately aligning the beams and adjusting the pump parameters.

1. Block the beam paths of pump for 4th and 5th passes.
2. Check that the input beam is centered on the input aperture A1 and aperture A2. If needed, align the incoming beam position and direction using the external steering mirrors.
3. Check that the beams of first three passes are in the same vertical plane. It is convenient to check the beam positions at CM1 mirror (see Fig 14): The beam after the first pass should strike the top edge of CM1 and after the third pass should go right above the first pass beam. Try to align beams by fine adjustment of the external mirror.

 Notice that if one wants to align the TOPAS at a different signal WL, it is possible by manually turning the crystal (using the appropriate stepper motor knob), it is possible to change the color of the superluminescence seed (e.g. for signal at 1500 nm ~ green, at 1600 nm ~ yellow, at 1300 nm ~ purple)

4. If you cannot see the 3rd pass beam, check that the beam after second pass through NC hits the mirror CM2 (see Fig. 14). If you cannot obtain beam pattern on CM2 by adjusting the external mirrors, try to adjust the CM1.
5. The central part of the amplified SFL should pass in between CM1 and M5 and should go right through the horizontal slit of CL2 holder. If the beam pattern does not fit the horizontal slit of CL2 holder, first try to get the right alignment by adjusting the external mirror. If the beam after the third pass still does not go through the slit, adjust the tilt of CM2.

 Notice that the beam patterns after 2nd and 3rd pass should be

vertically stretched because in first three passes the beams are focused to a horizontal line in the NC by means of cylindrical optics (CL1, CM1 and CM2).

6. Check that when aperture A2 is closed (or smaller diameter), the visible SFL signal disappears. This is due to the fact that by closing the A2, the power in the crystal drops (energy goes down and beam diameter increases in focal point) and the power is no longer high enough to produce SFL.
7. Monitoring the signal of the SFL in front of CL2 gradually start to open A2. Find the optimum size of A2 when the parametric light is stable and strong enough (**Photo 1**), but the signal of supercontinuum is absent or very weak.

Caution! Remember that threshold of supercontinuum generation and optical damage of crystal is rather close. Don't work in condition of supercontinuum generation for a long time.

8. If you cannot get any visible light after the third pass with A2 fully opened, it may indicate that the pump laser is not working properly. Proceed further only after making sure that the pump is optimized and that the first TOPAS passes have no damaged optics including the NC. Indication of damage is scattered pump beam and/or strong white-light (continuum) generation. Also check that the NC angular position is OK. Reset the crystal if you are not sure.
9. If everything is OK and still no visible light can be detected after the third pass, try to move the lens L1 to get a higher intensity in the crystal and brighter visible light after the third pass (different divergence might require repositioning of L1. Note: No superfluorescence with the same pump divergence would indicate a decreased pump intensity- longer pulse duration at the focal point, smaller energy or lower

contrast. One has to check the laser before proceeding further). Mark the beam position in front of CL2 before unscrewing L1, and try to maintain the same position when moving. Go through this section once more to check the first-third passes after securing the L1. The goal is to achieve strong and stable SFL after three passes.

10. Check that input pump beam goes through the center of apertures A1 and A2. If needed, move holders of aperture A2 to the right position.

3.5 Realignment: Fourth pass: pre-amplification of the seed.

At this point, the first three passes should be aligned. So, the external beam routing mirror should not be touched anymore, unless it is for very fine optimization later on. Remember that the third pass should already have SFL signal generated only with the power contained in the first three passes. Now, we have to make sure that the seed reflected from the grating collinearly overlaps spatially with the pump in the fourth pass and adjust the time overlap between the pump and seed pulses if needed. Then, with the fourth pass, we will pre-amplify a part of the spectrum of this seed signal in the field of second channel pump. Refer to Part 2 for more general explanations.

 *For convenience set the TOPAS signal wavelength close to 1500 nm (reset motors if any have been touched by hand). So, the SFL signal should be green (to be more exact, SFL is in IR, however it produces some green-yellow-red when mixed with pump in the same nonlinear crystal).*

1. Open the beam path of the pump for 4th pass.
 2. Make sure that the pump beam reflected from BS2 is centered on the aperture A3.
- If needed, perform the beam direction adjustments in vertical (twisting wedged

BS2 adapter) and horizontal (adjusting angular position of BS2 and M3 holders) planes.

3. Check that the pump beam is not clipped along the beam path towards M5. If necessary perform needed alignments by adjusting M3' angular position.
4. Check that the pump beam spot on M5 is in the vertical plane containing the beams after the first and third passes and fits the aperture of mirror. If need perform alignment of M4.
5. Check that pump beam reflected from M5 is in the vertical plane containing the beams of the 1st-3rd passes. You can perform this check by placing the card in front of the Main assembly and scanning its height. Another check point is at aperture A2: The pump beam reflected from M5, M2 and M1 should be shifted from the center of A2 only in the vertical plane. Align M5 if needed.
6. At this point verify that the 4th pass pump itself is not producing SFL and/or supercontinuum signal: closing the pump for first three passes you should see no light except the pump beam patterns. If SFL or/and supercontinuum are present reduce the size of A3. Find the optimum size of A3 when the pump intensity in the NC is just below the threshold of SFL.

Caution! Remember that the threshold of supercontinuum generation and optical damage of the crystal is rather close. Don't work in the condition of supercontinuum generation for a long time.

7. Observe two spots going away from the main assembly towards M10 (side reflection of M2). Since both the pre-amplified seed and non-phaseshifted SH of the pump are passing through M2, the spots should be composed of the SH of the pump

(blue spots at ~400 nm) and some seed green light (when at 1500 nm) (see Fig.

15). Likewise, you could see a stable green beam (from signal & idler sum frequency with the pump) when placing the card behind the TD crystal.

8. Verify that the observed parametric light is a seed amplification in the 4th pass. When closing first three passes the parametric light should disappear. If you have

amplification, go to **Realignment: Fifth pass: final-amplification of the seed**

(Chapter 3.6).

If the alignment of beams and pump intensity in the NC is OK, but you see no amplified superfluorescence the reasons for that could be : i) pump and seed are not overlapped in space, ii) pump and seed are separated in time. Usually these adjustments are performed using the zero order diffraction from the DG. That means that instead of reflecting seed at the second or higher order with a particular angle, the seed is reflected at 0 angle.

9. Block the beam paths of pump for 4th and 5th passes.

10. Mark the grating holder (moving part) position with respect to its sleeve (still part) and set grating to 0 angle

i. (For femtosecond TOPAS model) Just rotate the grating to 0 position by using the "Direct access" menu of TOPAS software (for details refer to the TOPAS CONTROL SOFTWARE/HARDWARE manual).

ii. (For picosecond TOPAS model) Unscrew the screw S1 (using hexagonal key) on the side of the grating (ref. Fig.16 below) and twist manually the grating to approx normal incidence with reference the third pass beam. Fix S1 and perform fine grating angle adjustment using the stepper motor knob "Grating" to

get green light reflected backwards through the M5.

 Notice that by touching the grating screw S1, you will lose the calibration of the grating. Therefore, a calibration will have to be performed after alignment.

(Figure 18)

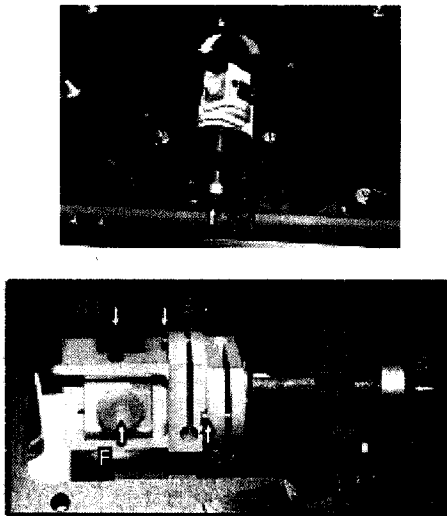


Figure 18. Views of the diffraction grating holder and the position of the adjustment screws Notice that on this picture, the grating angle is NOT at the 0 order position, but the direction of the rotation is shown.

(Figure 19)

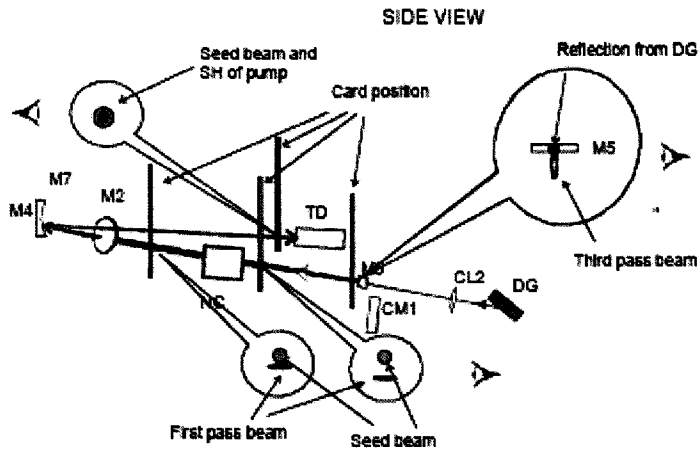


Figure 19. Views of the beam pattern configurations for the fourth pass alignment.

Now you should check the position of the beams at several points verifying that the seed beam reflected from DG is properly aligned. Use the diagram presented in Fig.17 above. Make sure the seed beam reflected from the grating fits the aperture of M5 and is in the same vertical plane as the 1st – 3rd pass beam. For this purpose check the beam pattern position when placing the card behind M5, in front of NC, and in front of the main assembly (looking from the DG side). If needed, adjust seed position in the horizontal plane by means of the screw S2 (ref. Fig.16). **Make sure the seed passes through nonlinear crystal, not above.**

Now you should verify that seed pulse overlaps with fresh pump beam at fourth pass through the NC.

12. Open the beam path of the pump for 4th pass.

13. Verify that the overlapping occurs in front of the NC and in front of the Main assembly. The most accurate check point is in front of time delay crystal TD where the seed and SH of the pump should clearly overlap (ref. Fig. 17). To verify the overlapping, alternatively block (ON/OFF) the pump beam to see the green and then the blue

overlapping the green spot. If needed perform fine pump beam direction adjustments by means of M4 and M5.

Now you should achieve the optimum seed and pump overlap in time.

14. Monitor the seed beam pattern on the card in front of TD and adjust the Delay 1 knob (crystal delay). At proper pulse timing the intensity of the seed green spot sharply increases. Maximize the amplified seed energy by monitoring the green light intensity or/ and by measuring energy of the pre-amplified (in 4th pass) seed at the output of TOPAS.

☞ *Notice that the pump intensity in the fourth pass must be below the threshold of superfluorescence when the seed is blocked. The superfluorescence may be easily detected just after the NL crystal or after reflection from M7 in front of the TD (Photo 7-9,). Superfluorescence will have a much bigger beam diameter of VIS(yellow-green-reddish) light than the amplified beam. Generation of supercontinuum (colored concentric rings) indicates that the pump intensity is much too high(Photo 3). Close A3 to reduce the intensity.*

At this point you have the properly adjusted the 4th pass working with the grating at the 0 angle, i.e. the DG is operated as a simple mirror. The following step is to restore grating operating angles.

15. Rotate the DG to the position corresponding to the TOPAS operation wavelength

i. For femtosecond TOPAS model: Just set a working angle of the grating using the "Direct access" menu of the TOPAS software (for details refer to TOPAS CONTROL SOFTWARE/HARDWARE manual).

ii. For picosecond TOPAS model: Reset the grating motor. Unscrew the screw S1 and tilt the grating face down and match the marks that should have been made

before releasing the screw (point 10 of this chapter). This will ensure that you will catch at least the same diffraction order. Perform fine grating angle adjustments from the "Direct access" menu maximizing the amplified seed intensity.

 Notice that by touching the grating screw S1, you will lose the calibration of the grating. Therefore, a procedure of grating calibration presented in the TOPAS CONTROL SOFTWARE/HARDWARE manual will have to be performed after full TOPAS alignment.

3.6 Realignment: Fifth pass: final-amplification of the seed.

The first four passes are aligned. Now, we have to make sure that the pre-amplified seed pulses overlap in space and time with the fresh pump in the last (fifth) pass.

1. Unblock the 5th pass pump.
2. Check that the fifth pass pump beam is passing in the middle of the optics. Check that the fifth pass pump beam is in (or is parallel to) the vertical plane containing the beams of 1st – 4th pass and that it goes through the center of the crystal (adjust M10 and M11 if needed).

 Notice that M11 is installed in the assembly that also holds M8. When turning the two knobs at the back of the M8-M11 assembly (closer to the TOPAS front panel) you are aligning M8 only. When adjusting the other pair of assembly knobs M8 and M11 are moving together

Be careful when aligning the pump input direction. Any pump beam should fit the aperture of the nonlinear crystal. If the pump hits the crystal holder a deposition of metal particles on the crystal surface eventually will cause

damage to the crystal.

3. Check that the fifth pass pump is collimated: its size it should change negligibly over a distance of several meters after the TOPAS. Adjust the position of the negative lens L6 if needed. You should not see any parametric light generated in the fifth pass, when the first 4 passes are blocked.
4. Overlap the seed beam (fourth pass) with the pump on M11. To do so, block the pump and look on the card before M11 to see the green light spot corresponding to the seed radiation coming after the 4th pass (see Fig. 18 for the position of the card). Then, unblock the pump and check the overlapping of the pump with the seed. Adjust M7 to optimize the overlapping visually.

Figure 20

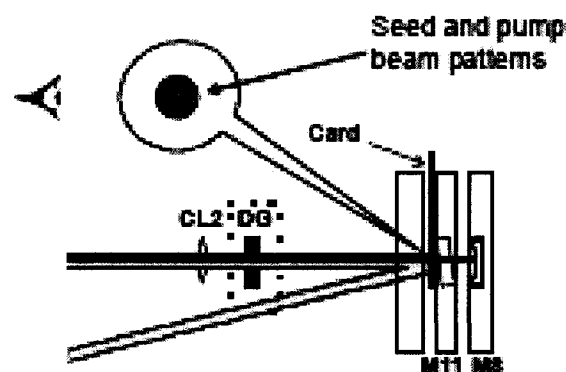


Figure 20. Views of the beam pattern configurations for the fifth pass alignment.

5. Verify that seed and pump overlap, at a 1-10 m distance away from the TOPAS, by alternatively blocking (ON/OFF) the pump beam. Also, check that the spectral components of the parametric light are not separated in space. If needed perform M8 adjustments.

The direction of VIS light generated in the main crystal of TOPAS may not

overlap exactly with the signal beam direction. Points 6-10 below present the description of a more accurate verification of the beam alignment in the 5th pass.

6. Set the TOPAS to 1300 nm*. If in previous steps the grating has been set to the 0 diffraction order and back using the screw S1 (see Fig. 16), its angle may not correspond to the optimum one. So, tune the grating using the “Direct access” menu and maximize the pulse energy of the 4th pass pulse after setting the wavelength.

7. Install mixer 1 with crystal #2 for generation of second harmonic of signal (SHS) and from the “Direct access” menu rotate the crystal of the mixer to the position where the SHS signal (red light) is most intense.

8. Move Delay 2 (use Amplifier slide bar in the “Direct Access” window) to get rid of the amplification in the 5th pass if you have any and observe at the output the pattern of the relatively weak red light (second harmonic of the preamplified seed after 4th pass.).

9. Check the overlap of the pump and the SH of signal in the near field (just after the SH crystal) and in far field (2- 10 m) from the TOPAS. You can use the weak blue light (SH of pump) for monitoring of pump beam position. Overlapping the signal with pump in the far field should be optimized by adjusting mirror M8. In order to improve overlapping in near field adjust M7.

At this point it is convenient to optimize the intensity of the pump for the 4th pass.

10. Monitoring the red beam intensity change the size of A3. The intensity and shape of the spot should change when adjusting A3. When A3 is opened too much you can see the appearance the ring surrounding the central spot. The pump intensity is

optimum when a central spot intensity is maximum, but the ring is still absent.

The last task is to restore the optimum Delay 2 .

11. Using Amplifier slide bar in “Direct Access” window return the Delay 2 position the setting it was before starting the 8th point of the procedure.

12. Scan the delay in a certain range looking for highest TOPAS output energy.

 Notice that usually you can find a few points with weak amplification besides the two strong ones while adjusting Delay 2. Two positions of the Delay 2 (separated by ~ a full turn of the Delay 2 knob) give the highest output power. The first point (smaller pump delay) comes when the pump is overlapped in time with signal pulse and the second point occurs when the idler is overlapped in time with the pump (signal and idler pulses are separated in time in the TD). The first one (signal pulse overlap usually gives a higher output energy and stability).

When optimizing Delay 2 (amplifier delay) verify that spectra positions of the second harmonic of the seed and the fully amplified signal are same. Different center wavelengths of the amplified signal correspond to a misaligned phase matching in the final pass. If this is the case perform fine adjustments to M8 and M11 to adjust the angle in the horizontal plane.

Pulse energy is one of the main parameters for optimization. However, when optimizing Delay 2 you can take into account also the shape of the spectrum and duration of output pulse. Sometimes (when pump intensity is a little too high) a more homogeneous spectrum is generated with slightly misaligned power amplifier delay. One can use pulse duration, shape of spectrum for final optimization of the delay. Often one

has to make a compromise between the highest energy, clean spectrum and pulse profile when optimizing Delay 2. Signal and idler pulse duration is usually shorter than pump pulse duration, if pump is >100 fs and pump pulses are close to bandwidth limited.

3.7 TOPAS recalibration.

Realignment of the TOPAS usually results in slight changes in the beam directions and optics positions. However you can avoid the measurement of a new tuning curve for the TOPAS by performing recalibration procedures for the optical elements whose angular or spatial position is controlled by stepper motors. The aim of the recalibration is to verify and optimize the offsets for the stepper motors regarding to the new optic positions inside the TOPAS.

The detailed descriptions of TOPAS recalibration procedures are presented in **TOPAS CONTROL SOFTWARE/HARDWARE manual, Chapter 4.4 Corrections.**

APPENDIX I: TOPAS LAYOUT

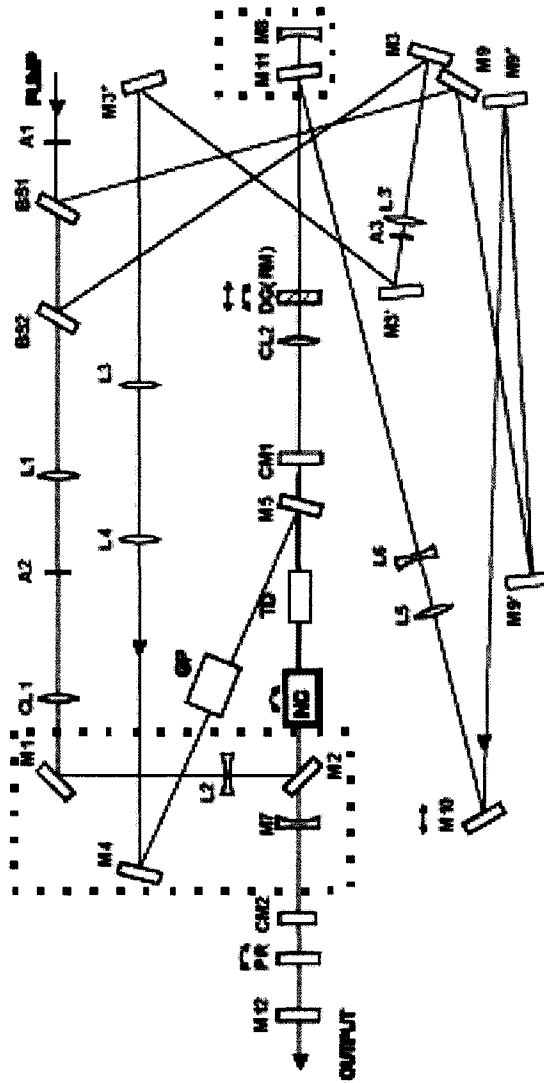


Fig. A1: Top view of the general layout of the TOPAS optical elements. The five passes are represented simultaneously and the abbreviations are given below.

ABBREVIATION SIGNIFICATIONS

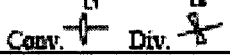
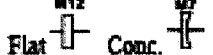
Sample abbreviation	Signification	Sample symbol
A1	Aperture	
BS1	Beam splitter	
L1	Diverging or converging lens	
CL1	Cylindrical lens	
M12	Flat or concave mirror	
CM1	Cylindrical mirror	
PR	Polarization rotator	
NC	Nonlinear crystal	
TD	Time delay	
DG	Diffraction grating	
GP	Fused silica plate	
.....	Main assembly element	

Table.A1: Significations of the abbreviations used on the TOPAS layout.

APPENDIX II: ADDITIONAL PROCEDURES

If the TOPAS pump energy, beam profile or the beam size/divergence were changed significantly you should probably adjust the beam collimation lenses inside the TOPAS in order to reseat the TOPAS for the new pump beam parameters. The following procedures are related to that particular situation.

First three passes focusing adjustment:

The aim is to find the optimum pump focusing condition in order to get the most stable signal of amplified superfluorescence after three passes through the nonlinear crystal.

- The lateral adjustment of L1 (horizontal position on the base slot) will change the size of the beam on the the crystal. We want to get enough intensity to get superfluorescence but yet, not to burn the crystal. Therefore, by precaution, scan SLOWLY increasing the intensity (ref. fig. A2). Make A2 smaller at this point to prevent too high intensity at some elements. Make smallest possible pump beam after three passes. Then open slowly the A2.

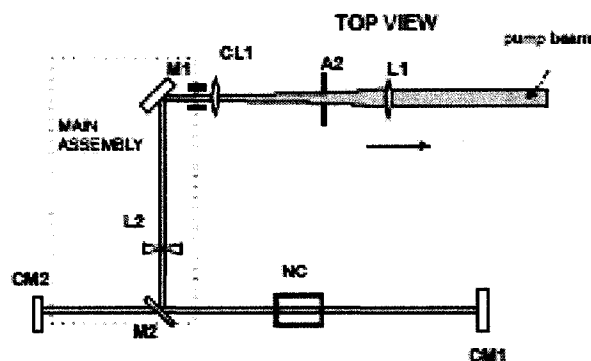


Fig.A2: Top view of adjustment direction of the lens L1 in order to change the intensity of the beam on the crystal.

- Make sure that the vertical alignment of the first and third pass still good while scanning the L1. Also, if the beam is too wide or blurry on the card before CL2 that means that the beam is too intense on the crystal. There are two possible solutions: close A2 a little until the beam looks good, **or** move L1 more carefully and more finely to get the right position that will allow the right intensity on the crystal.

Notice that if the lens is already aligned and the beam is slightly blurry, try using the aperture. However, if a major alignment of the beam is required, try moving the lens to the appropriate position. Change BS1 to higher reflection if pump intensity in the first three passes is too high and one has to reduce pump beam diameter (by A2) significantly.

Fourth pass focusing adjustment

The aim is to adjust the second pump channel zoom telescope for optimum seed preamplification.

- Adjust first L3 laterally on the base slot in order to get highest intensity in the crystal.

Then, if L3 is not enough to focus properly, adjust lens L3' in the same way the.

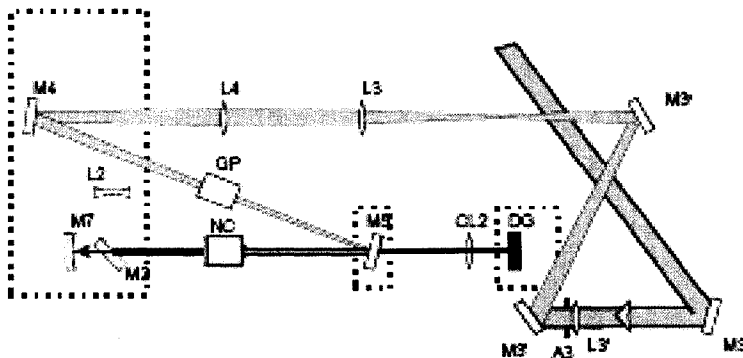


Fig.A2: Top view of the adjustment direction of the lens L1 in order to change the

intensity of the beam on the crystal.

Notice that if the focus is too much, one can decrease the intensity of the beam using A3 to lower the power on the crystal (to avoid burning). Remember that the beam size of the fourth pass has to be small for two reasons: first, to have enough intensity to pre-amplify the seed and second, to select a limited spectrum of the diffracted light from the grating. Spatial filtering is also performed here. A small beam focused at long distance would have clean central part and blurry peripheral area in focal point. This spatial filtering helps to generate a homogeneous seed beam.

Fifth pass collimation adjustment

The aim is to form the highly collimated pump beam for the final amplification stage.

Adjust first L6 laterally on the base slot in order to get the beam collimated (check that the beam size does not change over distance).

Notice that final signal and idler beam size and divergence will depend mainly on the shape and divergence of pump beam. Make a diffractive divergence of the pump beam in order to maximize the energy of the mixer stages (Difference frequency is most sensitive mixer stage. Signal and idler are conjugated pulses and beams. Diverging signal would correspond to converging idler and vice versa.).

APPENDIX III: PICTURES



Photo 1

Photo 1:
The typical shape of the pump beam with super-fluorescence (SFL), viewed after the 1st pass through the nonlinear crystal (NC). SFL acts as a seed emitting broad band super-fluorescence.

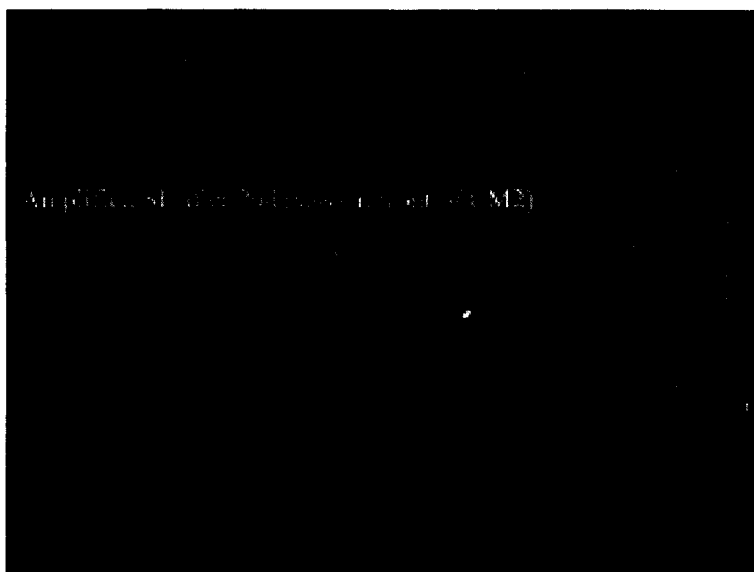


Photo 2

Photo 2:
Amplified SFL after 2nd pass through the NC, viewed in front of CM 2. The second pass is the backwards reflection from CM 1, through the NC to CM 2. The second pass amplifies the collinear parts of the SFL produced in the first pass.

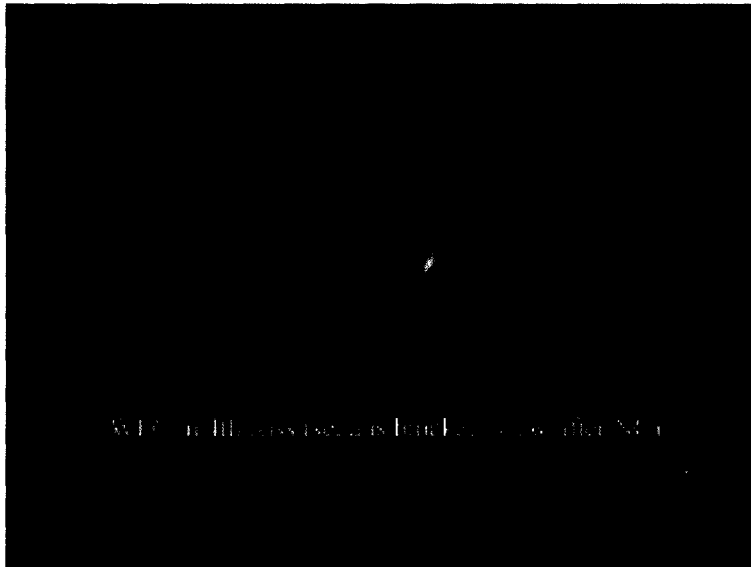


Photo 3

Photo 3:
Light due to
supercontinuum
generation viewed
after NC. Super-
continuum
generation is at the
crystals optical
damage threshold; if
visible decrease the
size of aperture 2.
Don't work in the
condition of
supercontinuum.

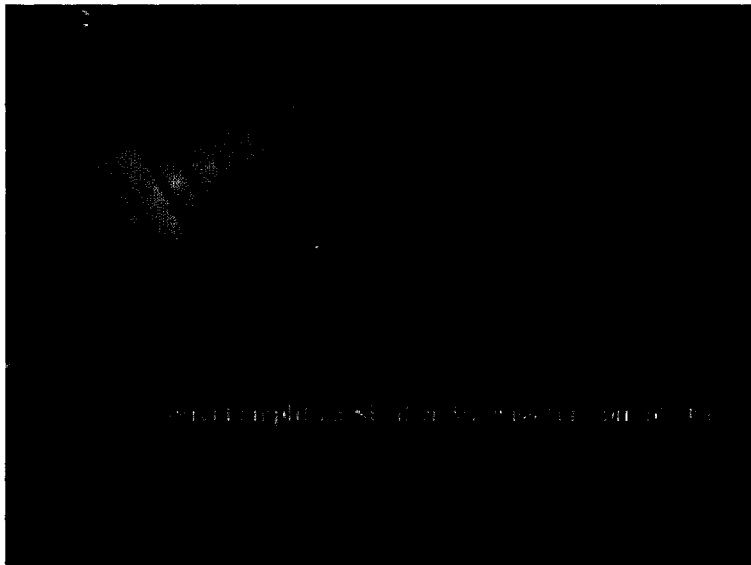


Photo 4

Photo 4:
The third pass is the
reflection from CM
2 through the NC to
the diffraction
grating. The correct
amplified SFL after
the third pass is
observed in front of
the diffraction
grating (DG).

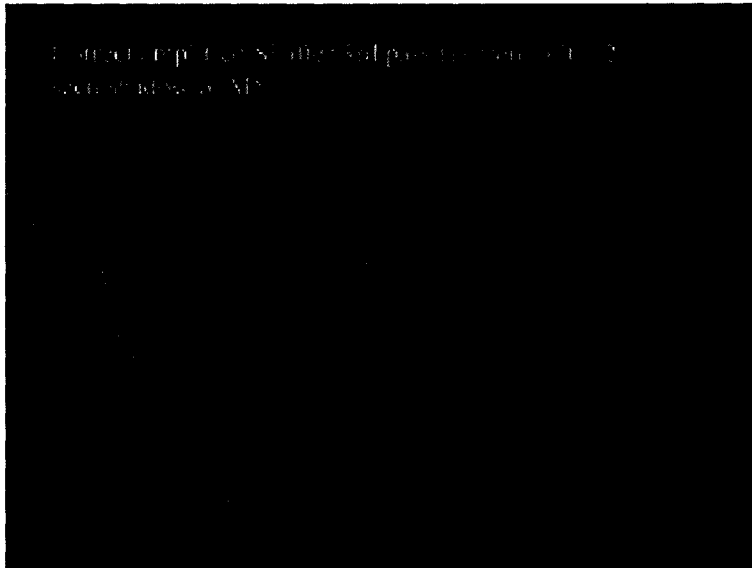


Photo 5

Photo 5:
 Correct amplified 3rd pass, viewed before the diffraction grating (DG) in front of the cylindrical lens (CL2). CL2 collimates the beam and the slit in front of it acts as a cursor for proper alignment so that the collimated portions hit the center of the DG.

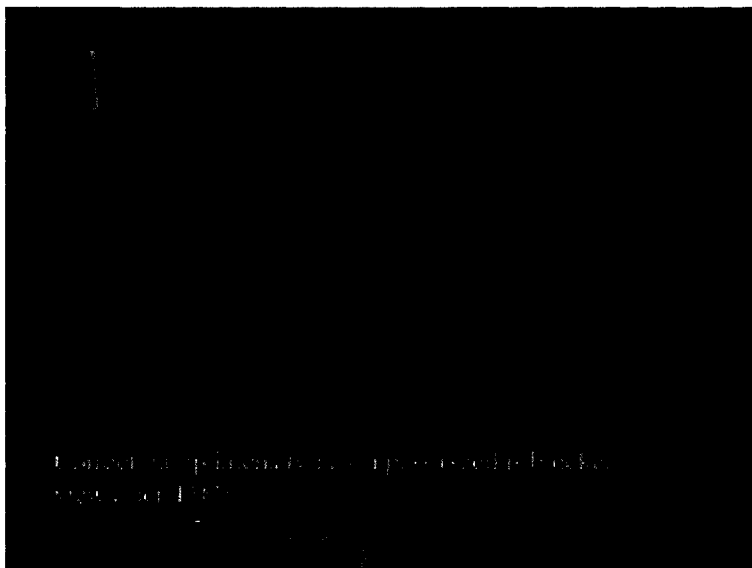


Photo 6

Photo 6:
 The bright visible spot indicated an effective seed pre-amplification in the 4th pass. This beam is viewed after the time delay (TD) crystal and the seed beam is blocked.



Photo 7

Photo 7:
The correct seed
intensity in the 4th
pass, the view is
after the TD crystal.
Note the pump is
blocked.

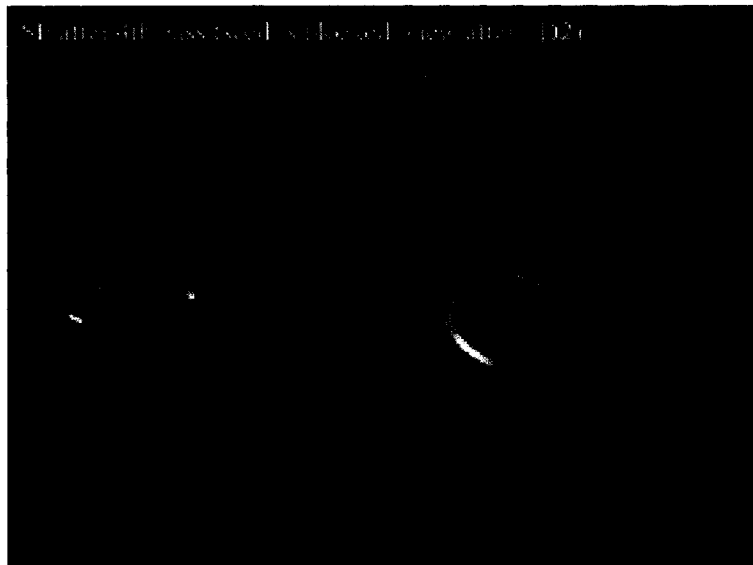


Photo 8

Photo 8:
The correct pump
intensity after the 4th
pass with the seed
blocked. Viewed after
the TD crystal.

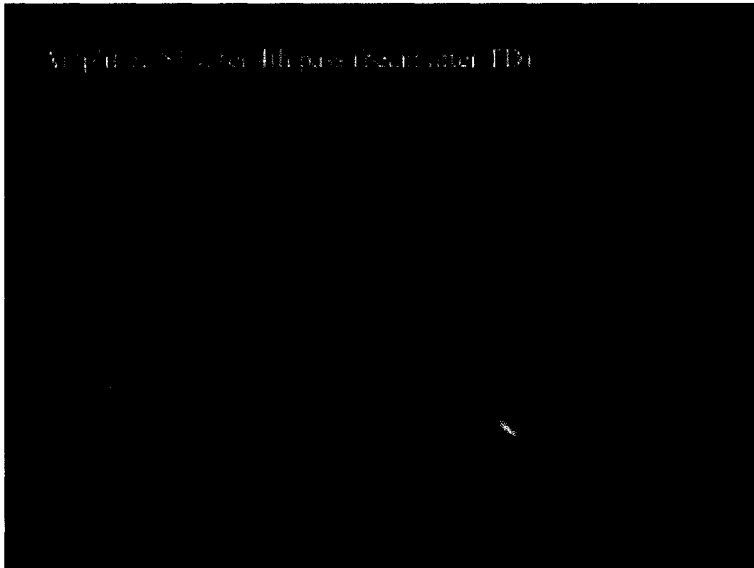
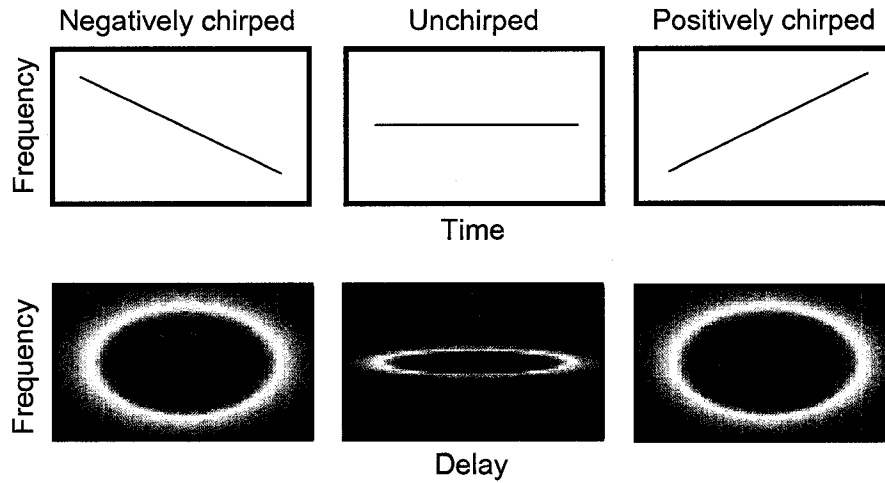


Photo 9:
Properly amplified
SFL after the 4th
pass, viewed after
TD crystal. If
colored concentric
rings are observed
a supercontinuum
is being generated
and the pump
intensity is much
too high (close A_3
to reduce the
intensity).

Photo 9

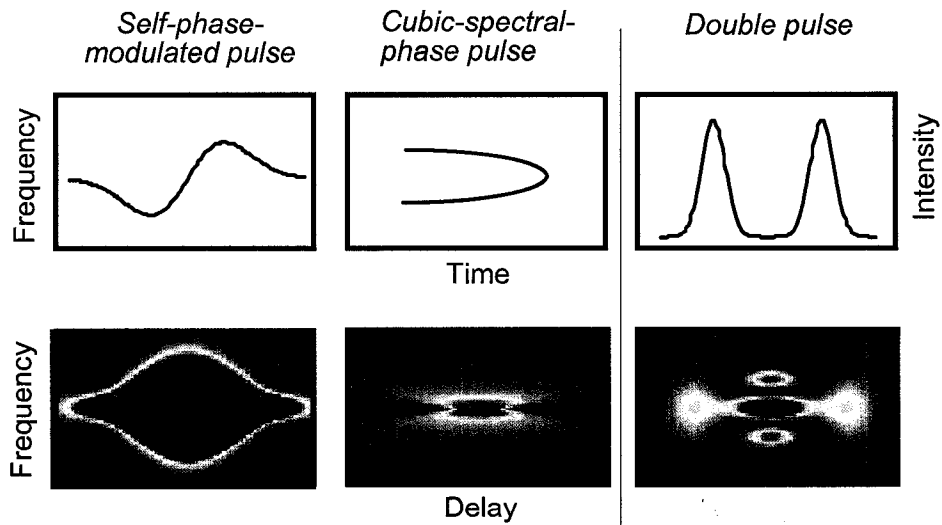
SHG FROG traces



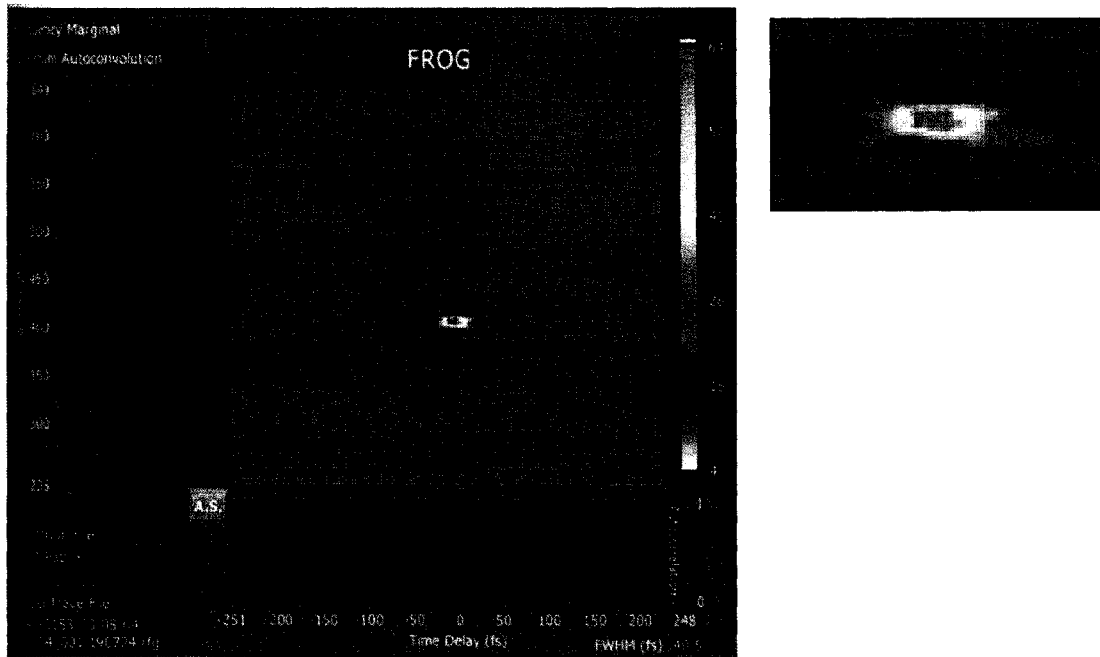
SHG FROG has an ambiguity in the direction of time, the traces are symmetric with respect to delay.

www.physics.gatech.edu/gcuo/ultrafastoptics

Complex SHG FROG traces



www.physics.gatech.edu/gcuo/ultrafastoptics



A SHG FROG image from our amplified system. The picture in the upper right is zoomed in image of the FROG trace on the right. Note the colors are inverted from the two previous FROG examples.

Note: Our SHG FROG trace represents a pretty well aligned system. One should look for a circular trace with the most intense signal at the center. The image shown above has a slight amount of cubic-spectral phase (note cross within spectrum) but overall it is quite concentric. Pictures on the previous page represent poorly aligned systems.

References

- (1) Spence, D. E.; Kean, P. N.; Sibbett, W. *Optical Letters* **1991**, *16*, 42.
- (2) Fork, R. L.; Martinez, O. E.; Gordon, J. P. *Optical Letters* **1984**, *9*, 150.
- (3) Spence, D. E.; Kean, P. N.; Sibbett, W. *Optical Letters* **1991**, *16*, 42-44.
- (4) Negus, D. K.; Spinelli, L.; Goldblatt, N.; Feugnet, G. *Advances in solid state lasers*, 1991.
- (5) Eaton, H. K., University of Colorado, 1999.
- (6) Zhou, J. P.; Huang, C. P.; Shi, C.; Kapteyn, H. C.; Murnane, M. M. *Optical Letters* **1994**, *19*, 126.
- (7) Rudd, J. V.; Korn, G.; Kane, S.; Squier, J.; Mourou, G. *Optical Letters* **1993**, *18*, 2044.
- (8) Martinez, O. E. *IEEE Journal of Quantum Electronics* **1987**, *QE-23*, 1385.
- (9) Martinez, O. E. *IEEE Journal of Quantum Electronics* **1987**, *23*, 59.
- (10) Martinez, O. E. *Journal of the Optical Society of America B* **1986**, *3*, 929.
- (11) Moulton, P. F. *Journal of the Optical Society of America B* **1986**, *3*, 125.
- (12) Backus, S.; Durfee, C. G.; Murnane, M. M.; Kapteyn, H. C. *Review of Scientific Instruments* **1998**, *69*, 1207.
- (13) Akturk, S.; Kimmel, M.; O'Shea, P.; Trebino, R. *Optics Express* **2003**, *11*, 491-501.
- (14) Podenas, D., 2003.

Appendix 3: Sample Preparation

Introduction

MALD (matrix assisted laser desorption) is a technique which places highly unstable, fragile large species into the gas phase as individual intact molecules¹⁻⁶. A novel approach to a well known technique has allowed for the production of single molecule gas phase energetic materials. To produce gas phase molecules from the thermally unstable, non-volatile solid energetic material samples a specific sample drum must be prepared. This sample drum allows for the production of a stable supply of the gas phase molecules for extended periods of time.

To prepare a sample drum a porous yet smooth surface must first be obtained for even sample deposition. This surface is prepared by producing an aluminum oxide thin film coat on an aluminum drum via a plasma electrolytic oxidation technique⁷⁻¹⁰. In this electrolytic oxidation technique a cylindrical Al drum ($l \sim 19.5$ mm, $id \sim 27$ mm, $od \sim 38$ mm) is immersed into an electrolytic solution and plays the role of anode. A DC voltage of 120 V and a current of 1.0 A is applied across the electrolytic solution. Plasma is formed on the surface of the Al drum thereby oxidizing it and forming an $\gamma\text{Al}_2\text{O}_3$ thin porous film. The Al_2O_3 has a grain size of <10 μm and a thickness of 10 μm .

The Al_2O_3 coated drum is the base for our sample preparations. A sample matrix is prepared and evenly sprayed upon the Al_2O_3 coated drum. The sample solution consists of equal molar amounts of the molecule of interest (RDX, HMX, and model systems) dissolved in a volatile solvent, acetone, and the matrix material. The matrix

material used in these experiments is the laser dye Rhodamine 590 (R590) and it is dissolved in methanol. R590 is ideal because it has a large absorption coefficient for the 532 nm light used in the MALD process and it forms a non-crystalline microscopically smooth thin film. A sample solution ($\sim 4 \times 10^{-3}$ mol/l) is sprayed, with an air atomizing spray nozzle (Spraying System Co.), on the Al_2O_3 coated Al drum. The drum is rotated and lightly heated with a light bulb during spraying, allowing for the aerosol to be evenly distributed, dry upon contact, and form a homogeneous thin film of the two species¹¹.

Once the sample drum is prepared it is placed within the laser desorption pulsed nozzle source (see introduction for more detail). The pulsed nozzle produces a carrier gas pulse (of Helium or Argon) which is timed to intercept the effluent from the laser desorbed spot on the sample drum. A 532 nm laser pulse, ~ 1 -2 mJ/ pulse, vaporizes the R590 laser dye in the matrix film but is not absorbed by the nitramine materials, which only absorb below 250 nm. This MALD technique places the material of interest into the vapor phase without decomposition. The gas phase material is then carried by the He/Ar through a supersonic expansion from the pulsed nozzle. The gas phase molecules are cooled ($T_{\text{tran}} \sim 1$ K, $T_{\text{rot}} \sim 10$ K, $T_{\text{vib}} \sim 50$ K) and lead into the spectroscopy region.

Preparation

This section contains a step by step procedure for preparing the sample drum. Figure 1, at the end of the document, illustrates the sample spraying setup.

It should be noted that porous filter paper can also be used as a base for the sample preparation. The filter paper is simply attached to the outside of the Al drum using double sided tape.

Plasma electrolytic oxidation

Electrolytic solution

NaF 0.6 M

Na₂B₄O₇ 0.1 M

(NH₄)₂HPO₄ 0.1 M

NaH₂PO₄ 0.5 M

Procedures:

Coating the drum:

1. In the electrolytic solution completely submerge anode (Al drum) and cathode (wire mesh). The reaction is very exothermic. Keep the electrolytic solution as cool as possible by immersing the beaker of electrolytic solution in a bucket of ice water. If coating more than one drum wait until the solution has cooled to room temperature before proceeding.
 - a. The Al drum should be connected to the power supply via a high purity Al wire. The wire should be tightly wrapped around the drum one time.
 - b. The wire mesh (screen) should be connected to the power supply.
2. Apply about 1-1.2 V and 1 Amp.
 - a. Turn up the voltage and slowly turn up the current.
 - b. Electrolytic discharge will begin on the Al wire and “jump” to the Al drum. During this process one must ensure the current and voltage remain somewhat constant. If contact between the Al wire and drum is not very good the wire might break resulting in loss of current.

- c. The coating process will look like an avalanche of sparks. Allow the process to proceed for 10-15 min or until the avalanche like sparks occur more sporadically.
3. Turn off power supply and remove coated drum and wire mesh from the solution.
Rinse with distilled water.

Recoating the Al drum

1. Removal of old Al oxide and R6G/ RDX matrix
 - a. Use methanol to remove the R6G/ RDX matrix.
 - b. Wash the old Al oxide drum with distilled water.
 - c. Place old drum in a solution of distilled water and sodium hydroxide (The concentration is not critical. About 5-10 pellets in 50ml of distilled water. Make sure to place inside the hood, it released hydrogen gas)
 - d. Allow the Al drum to sit for a couple of minuets, until most of the coat has fallen off.
 - e. Remove the Al drum from the solution with a glass rod (solution is very basic).
 - f. Rinse with distilled water and ensure that all of the Al coat is removed. If some still remains repeat the sodium hydroxide solution process.
 - g. After all of the Al coat is removed, let the drum sit in distilled water for about 20 min.
 - h. Rinse again with distilled water and finally clean with methanol.

Spraying the drum

1. First prepare the sample matrix solution

- a. Equal molar quantities of RDX or HMX and R6G laser dye must be measured out (4×10^{-3} mol/l).
 - b. Dissolve RDX or HMX in acetone and R6G in methanol.
 - c. Prepare matrix solution (4 ml of RDX and 8 ml of R6G)
2. While rotating the Al drum via a clock motor (to ensure homogenous coating) spray the matrix solution onto the drum using an air atomizing spray nozzle (Spraying System Co.).
 3. Heat drum, via a heat lamp, during spraying to help dry solvent (Figure 1).

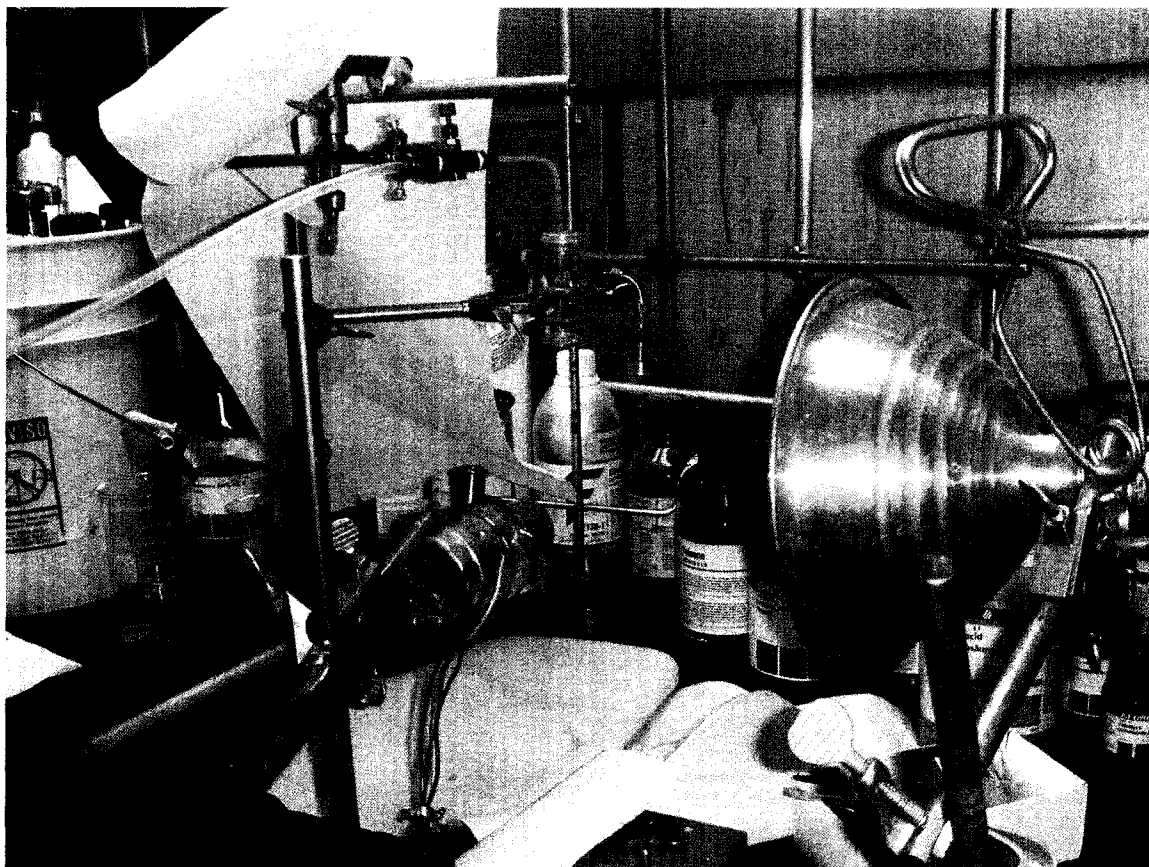


Figure 1. Sample preparation, spraying the Al_2O_3 coated drum.

References

- (1) Plows, F. L.; Jones, A. C. *Journal of Molecular Spectroscopy* **1999**, *194*, 163.
- (2) Jones, A. C.; Dale, M. J.; Keenan, G. A.; Langridge-Smith, P. R. R. *Chemical Physics Letters* **1994**, *219*, 174.
- (3) Dale, M. J.; Jones, A. C.; Langridge-Smith, P. R. R. *Analytical Chemistry* **1993**, *65*, 174.
- (4) Meijer, G.; Vries, M. S. d.; Hunziker, H. E.; Wendt, H. R. *Journal of Chemical Physics* **1990**, *92*, 7625.
- (5) Cable, J. R.; Turbergen, M. J.; Levy, D. H. *J. Am. Chem. Soc* **1989**, *111*, 9032.
- (6) Li, L.; Lubman, D. M. *Applied Spectroscopy* **1988**, *42*, 418.
- (7) Wirtz, G. P.; Brown, S.; Kriven, W. M. *Mater. Manuf. Processes* **1991**, *6*, 87.
- (8) Kurze, P.; Krysmann, W.; Schreckenbach, J.; Schwarz, T.; Rabending, K. *Cryst. Res. Technol.* **1987**, *22*, 53.
- (9) Krysmann, W.; Kurze, P.; Dittrich, K.-H.; Schneider, H. G.; *ibid* **19**, *19*, 973.
- (10) Dittrich, K.-H.; Krysmann, W.; Kurze, P.; Schneider, H. G.; *ibid* **1984**, *19*, 1984.
- (11) Im, H. S.; Bernstein, E. R. *Journal of Chemical Physics* **2000**, *113*, 7911-7918.

Appendix 4: RRKM theory

Due to the size of the energetic materials used in our decomposition studies we can assume that the dissociation kinetics will follow a simple exponential behavior. The high density of states contained in the molecules allows us to assume the intramolecular vibrational energy redistribution (IVR) is faster than the time scale of the reaction. This ergodicity assumption validates the use of Rice-Ramsperger-Kassel-Marcus (RRKM) transition state theory in our experiments. The following pages will discuss RRKM theory and how it is used to calculate an upper limit to the reaction coefficient $k(E)$.

RRKM theory is the most commonly used method of calculating microscopic rate coefficients for unimolecular reactions of polyatomic molecules. Research in unimolecular and recombination reactions has formed a major part of gas phase kinetics over the last 80+ years. A gas phase unimolecular reaction is a simple process in which an isolated molecule undergoes a chemical change. Possible unimolecular reactions include isomerizations, eliminations, and dissociation (Figure 1). The differences between these reactions can be illustrated in their potential energy surfaces. If a molecule undergoes a reaction it must have an internal energy high enough to exceed the barrier between reactant and product. Reaching an internal energy sufficient for reaction requires excitation which could occur by collision with a bath gas, $[M]$, at thermal equilibrium or laser excitation.

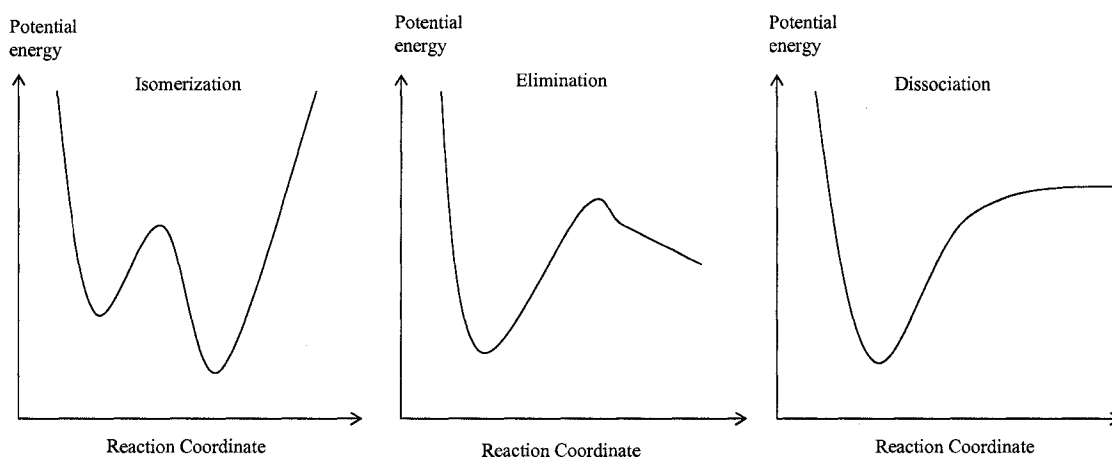


Figure 1. Potential energy along the reaction coordinate for isomerizations, eliminations, and dissociations.



An essential quality of a unimolecular reaction in the gas phase is that the time scale of the reaction (eq. 2) is much longer than that of the excitation (eq. 1). The separability of reaction and activation steps within a unimolecular reaction was first suggested by Lindemann in 1922. In a bath gas at high pressures, collisional activation and deactivation are so fast that eq. 1 processes are not rate determining. The overall rate coefficient of the reaction is dependent only on the intramolecular process (eq. 2), therefore the rate coefficient is independent of bath gas pressure. Conversely, at low bath gas pressures excitation processes are the rate determining step.

Excitation (eq. 1) and reaction (eq. 2) processes have a reaction rate in which reactant A^* is dependent upon its internal energy (E); yielding the following modified equation for reaction (eq. 3)



This notation was developed by Rice, Ramsperger, and Kassel in the late 1920's. In the 1950's Marcus demonstrated how one could compute $k(E)$ from the knowledge of the dynamics of the potential surface of the reaction. $K(E)$ can be computed exactly from classical trajectories (solving classical equations of motion on the potential energy surface describing the system) but, the solution to these classical equations of motion requires considerable computational time. Because of this, an approximate description of the dynamics of the reaction (eq. 3) was developed by Rice, Ramsperger, Kassel and Marcus and is called RRKM theory.

In RRKM theory transition state theory is applied to a microcanonical ensemble of the excited reactant molecules. Key concepts in this theory are that of the reaction coordinate and the realization that the transition state expression gives an upper bound to the rate coefficient that could be computed by a complete classical trajectory simulation. The reaction coordinate, s , is a curvilinear coordinate which links the reactant region of the potential energy surface to the product region. In transition state theory there exists some critical configuration between reactants and products (e.g. critical bond length) which once passed through by the reactant atoms, will not be re-crossed. An additional important approximation in RRKM theory is that of ergodicity: the rapid randomization of energy throughout all degrees of freedom of the reactant. The ergodicity and non-recrossing assumptions of transition state theory have been tested and found to be accurate for most systems. The reason why RRKM theory is most generally employed and widely accepted is because it is not only accurate but it is also readily applied computationally for typical systems (direct-count computer algorithms).

The fundamental idea of RRKM theory is as follows. If we are interested in the breaking of a particular bond in a molecule, a collision (with a bath molecule or photon) prepares the reactant with an internal energy (E) distributed over the various degrees of freedom. The energy will be transferred among the degrees of freedom where at times it will accumulate in and then dissipate from individual modes until sufficient energy accumulates in one particular bond that breaks for the reaction to occur. $K(E)$ is the inverse of the average time required for the bond to stretch to the length necessary for the bond to break.

$K(E)$ is calculated, using RRKM theory, through consideration of a microcanonical ensemble of all possible reactant states; all possible configurations and momenta that are consistent with a given energy E . First, a reaction coordinate is identified which defines the progress of the reaction from reactant to product regions of configuration space; this coordinate also serves to identify reactant and product regions in phase space. Next, one considers a surface in phase space that is orthogonal to the reaction coordinate and completely divides reactant from product regions, and evaluates the total flux of trajectories crossing from the reactant side to the product side. The rate coefficient is evaluated as the ratio of the flux of trajectories crossing the surface to the population of the reactant ensemble at energy E , see eq. 4 below.

The two fundamental assumptions in RRKM theory, ergodicity and the transition state, will be elaborated on below. The ergodicity assumption requires that vibrational energy is randomized rapidly on the time scale of reaction throughout all vibrational degrees of freedom (IVR is fast). This is the reason why all trajectories crossing the surface and all members of the reactant ensemble carry equal weighting in the expression

for the microscopic rate coefficient. In essence all parts of phase space are accessible on the time scale of the reaction and are subject only to the constraints of conservation of energy. If $E > E_0$ where E_0 is the critical energy from reaction then eventually that energy will end up in the breakable bond, no matter how the excited molecule was initially prepared. This randomization implies that all initial distributions of internal modes with energy E rapidly become “equivalent”. Postulation of a transition state rests on the assumption that all trajectories crossing a surface dividing reactant from products will have started in the reactant region and will go directly on to products without recrossing the dividing surface.

These two assumptions yield the final RRKM result:

$$k(E) = \frac{\int_0^{E-E_0} \rho^+(E_+) dE_+}{h\rho(E)} \quad (4)$$

In eq. 4, E is the energy in the active modes, $\rho^+(E_+)$ is the density of states on the transition state surface, and $\rho(E)$ is the density of states of the molecular reactant¹. The transition state surface is usually defined by a fixed value of the reaction coordinate, s , and hence when evaluating $\rho^+(E_+)$ one includes all active degrees of freedom except s .

In calculating $\rho(E)$ and $\rho^+(E_+)$, only the active modes of the molecule and transition state are included. All of the degrees of freedom of the molecule which participate in the randomization of the energy of excitation are the “active modes”. The modes usually include the vibrational degrees of freedom of the molecule and any internal rotational degrees of freedom.

Determining the density of states of a molecule requires solving the Schrödinger equation for all active modes; but in principle one can evaluate the density of states by replacing the exact Hamiltonian with an approximate one which separates the normal mode vibrations and internal rotations. Separating the Hamiltonian neglects coupling terms in the potential that are higher than quadratic but it doesn't significantly affect the overall density of states of the polyatomic. In order to determine $\rho(E)$ and $\rho^+(E_+)$ one needs to know the harmonic vibrational frequencies and the rotational constants for the reactant molecule and transition state. Rapid algorithms have been developed for the convolution of the density of states for vibrational and rotational degrees of freedom so that a typical RRKM calculation takes just a few second of computer time.

In calculating the density of states one must start with an approximate functional form for the separable rovibronic Hamiltonian,

$$H = \sum_{i=1}^N H_i . \quad (6)$$

In eq. 6 H_i is the Hamiltonian for the i^{th} normal mode vibration or rotation and N is the number of degrees of freedom. This separability enables the overall density of states to be expressed as a convolution of the density of states of the individual modes. Thus for two independent degrees of freedom,

$$\rho_{1,2}(E) = \int_0^E \rho_1(E_+) \rho_2(E - E_+) dE_+ , \quad (7)$$

in which, ρ_1 and ρ_2 are the densities of states for each term in the Hamiltonian. Eq. 7 can be iterated through all degrees of freedom to obtain the overall density of states. One can convolve $\rho_{1,2}(E)$ with $\rho_3(E)$ to obtain $\rho_{1,2,3}(E)$ and so on until all active modes have been included into the density of states. For determining the density of states of the rotational

and vibrational degrees of freedom a two part procedure is required. First one must determine the convoluted density of states for the active rotational degrees of freedom of the molecule, $\rho_{\text{rot}}(E)$. Using a classical approximation to the rotational density of states, $\rho_{\text{rot}}(E)$ may be obtained as an analytical function of the energy E . Second, the convolution of $\rho_{\text{rot}}(E)$ with the density of states of each normal-mode vibration must occur. This is accomplished by using the Beyer-Swinehart algorithm², which is based on the quantum energy levels of a harmonic oscillator.

Convolution of the rotational density of states, $\rho_{\text{rot}}(E)$, is accomplished by first evaluating the rotational partition function, which is proportional to the molecules rotational constant and then its inverse Laplace transform is taken to determine the rotational density of states. This method yields an analytical expression for the rotational density of states. Evaluation of a one-dimensional free rotor will be shown below. The Hamiltonian for a 1-D rotation is,

$$H = \frac{\rho_{\theta}^2}{2I} \quad (8)$$

in which, ρ_{θ} is the angular momentum, I is the moment of inertia of the rotor, and the potential V is constant for all angles and is zero. The rotational partition function, Q , and density of states $\rho(E)$ are defined as:

$$Q = \int_0^{\infty} \rho(E) e^{-E/k_{\text{B}}T} dE \quad (9)$$

$$\rho(E) = \frac{1}{h} \int d\Gamma \Gamma \delta(-E). \quad (10)$$

Giving

$$Q = \frac{1}{\sigma h} \int_0^{\infty} dE e^{-E/k_B T} \int d\Gamma \delta(-E) = \frac{1}{\sigma h} \int d\Gamma e^{-H/k_B T} \quad (11)$$

in which, σ is the symmetry number which reduces multiple counting of classically equivalent states in the rotational partition function and Γ represents the multidimensional phase space which corresponds to all positions, q , and momenta, p , of the system. Integration gives a simple form for the partition function,

$$Q = \frac{\pi^{1/2}}{\sigma} \left(\frac{k_B T}{B} \right)^{1/2}. \quad (12)$$

A similar method can be used to determine the partition functions for various dimensional types of rotors.

The Beyer-Swinehart algorithm³ directly counts the vibrational states of the system. This method rapidly evaluates the exact value of the density of states by using a few lines of computer code and a mere second of computer time. The algorithm determines the vibrational state pattern of a collection of quantized harmonic oscillators by counting all possible combinations of the vibrational quantum numbers that are consistent with a specific total energy. The simplicity of the Beyer-Swinehart algorithm rests in the fact that the algorithm successively runs up the energy scale for each oscillator and modifies the vibrational density of states iteratively. Slight modifications to the Beyer-Swinehart code allows for convolution of the density of states of rotation with that of vibration, yielding, after evaluation, the convoluted rovibrational sum of states necessary to calculate the reaction coefficient $k(E)$. More detailed information on these algorithms can be found in Gilbert and Smith's book "Theory of unimolecular and recombination reactions"³, chapter 4.

References

- (1) Robinson, P. J.; Holbrook, K. A. *Unimolecular Reactions*; Wiley-Interscience: London, 1971.
- (2) Holbrook, K. A.; Piling, M. J.; Robertson, S. H. *Unimolecular Reactions*; second ed.; John Wiley and Sons: Chichester, 1996.
- (3) Gilbert, R. G.; Smith, S. C. *Theory of Unimolecular and Recombination Reactions*; Blackwell Scientific Publications: Oxford, 1990.

Appendix 5: Source of materials

Contact information for the individuals who provided the energetic materials and model systems is provided below.

Michael Hiskey
Los Alamos National Laboratory (LANL)
DX-2 MS C920
Los Alamos, NM 87544
505-667-4592
Materials: DAAF, TAGAT, BTATz, DAATO

Laura Smilowitz
LANL C-PCS MS J585
Los Alamos, NM 87544
505-667-5207
Material: HMX

Jeffrey Bottaro
SRI International
333 Ravenswood Ave.
Menlo Park CA 94025
650-859-2000
Materials: nitropyrrolidine, nitropiperidine, C1 20

Lisa Lauderbach
Lawrence Livermore National Laboratory (LLNL)
7000 East Ave.
Livermore CA 94550
925-422-9889
Materials: TNT, RDX

Randy Simpson
LLNL
7000 East Ave.
Livermore CA 94550
925-423-0379
Materials: TNT, RDX

Sigma-Aldrich
1-800-325-3010
Material: dinitropiperazine